DIRECT PHOTON ANISOTROPY AND THE TIME EVOLUTION OF THE QUARK-GLUON PLASMA

A Dissertation

Submitted to the Faculty

of

Purdue University

by

Tyler A. Browning

In Partial Fulfillment of the

Requirements for the Degree

of

Doctor of Philosophy

August 2016

Purdue University

West Lafayette, Indiana

ACKNOWLEDGMENTS

This thesis would not have been possible if not for Professor Rolf Scharenberg and Professor Andrew Hirsch. Their efforts gave me the freedom to pursue my own path, make my own mistakes, and come to my own conclusions. From them, I learned freedom of thought, which is the essence of science. I would like to thank Professor Brijesh Srivastava for daily discussions which not only enlightened my research, but also gave me the encouragement to never give up and never look backward. I would like to thank Dr. Dmitri Peresunko of the Moscow Engineering Physics Institute for his patience and assistance. I would like to thank the ALICE collaboration for the data and experience that was crucial for this work. I would like to thank my thesis committee: Dr. Finley, Dr. Kruczenski, and Dr. Xie for their guidance and instruction. I would like to thank Dr. David Garand for treading this path before me and showing me the way. I would like the thank Dr. Cyrus Vandrevala for countless long conversations and broadening my horizons to approaches I had never considered before. I would like to thank Dr. Na Yu, whose faith in me helped push me through to the end. And finally, I would like to thank my family for encouraging me to pursue my dreams no matter where they led me.

TABLE OF CONTENTS

Page

Page

Page

LIST OF FIGURES

Figure Page

Figure Page

Figure Page

ABSTRACT

Browning, Tyler A. Ph.D., Purdue University, August 2016. Direct Photon Anisotropy and the Time Evolution of the Quark-Gluon Plasma. Major Professor: Andrew S. Hirsch.

Historically, the thermal photon inverse slope parameter has been interpreted as the thermalization temperature of the QGP. Observation of the thermal photon spectrum in nucleus-nucleus collisions at the ALICE and PHENIX experiments obtain the inverse slope parameter, but the obtained values are inconsistent with the thermalization temperature predicted by the hydrodynamic model. It has therefore been argued that the inverse slope parameter is not representative of the true QGP thermalization temperature because not all thermal photons are emitted at thermalization. This research will probe this assertion using an investigation of flow and nuclear suppression of thermal photons from ALICE Pb-Pb collisions at $\sqrt{s_{NN}} = 2.76$ TeV and comparison to p-p data at $\sqrt{s_{NN}} = 2.76$ TeV.

1. INTRODUCTION

1.1 Heavy Ion Collisions

1.1.1 Quarks, Gluons, and the Standard Model

In 1968, the Stanford Linear Accelerator Center (SLAC) probed atomic nuclei by bombarding them with electrons in a process now known as deep inelastic scattering [1]. They found that hadrons, which had previously been considered individual "hard" particles, in fact possess a sophisticated internal structure. The Standard Model is used to explain the internal structure of hadrons, as well as to characterize the interaction mechanism between those structures and every other kind of matter.

In the standard model, hadrons consist of fundamental constituents called quarks which exist in a quantum bound state. There are six quarks (in order of increasing mass): up, down, strange, charm, bottom, and top in addition to their respective anti-quarks. In addition to mass, each quark is uniquely identified with their quantum numbers (see 1.1) which determine how they bind to each other. Groups of two ($q\bar{q}$) and three (qqq) bound quarks are known to exist, and are called mesons and baryons, respectively. Larger bound states, such as a pentaquark ($qqqq\bar{q}$) have been hypothesized, but have never been observed [2]. The defining characteristic of these bound states is the need to balance a quantum number independent of quark flavor called color charge into a "colorless" bound state. The standard model predicts that the bound quarks will interact by sharing color through intermediate virtual gauge bosons called gluons. These are Yukawa particles immediately analogous to photons from quantum electrodynamics. Assuming a separable solution to the Schroedinger equation, this modifies the wave function of the state by a color dependent prefactor. It can be seen as a modification to the Lagrangian to include a new term that is responsible for color interactions; this "color term" represents the strong nuclear force.

Table 1.1.
Table enumerating the invariant mass and fundamental quantum numbers of the six quarks. The invariant mass is measured in the typical units of $\frac{MeV}{c^2}$, and include uncertainties. After the mass, the quantum numbers are (in order): total angular momentum, baryon number, electric charge, isotopic spin, strangeness, charmness, bottomness, and topness. These numbers determine the form of the color term in the bound state wave function. [2]

Name	Symbol	Mass ($\frac{MeV}{c^2}$)	J	B	Q	I_3	s	c	b	t
Up	u	$2.3^{+0.7}_{-0.5}$	$\frac{1}{2}$	$+\frac{1}{3}$	$+\frac{2}{3}$	$+\frac{1}{2}$	0	0	0	0
Down	d	$4.8^{+0.5}_{-0.3}$	$\frac{1}{2}$	$+\frac{1}{3}$	$-\frac{1}{3}$	$-\frac{1}{2}$	0	0	0	0
Strange	s	95^{+5}_{-5}	$\frac{1}{2}$	$+\frac{1}{3}$	$-\frac{1}{3}$	0	+1	0	0	0
Charm	c	1275^{+25}_{-25}	$\frac{1}{2}$	$+\frac{1}{3}$	$+\frac{2}{3}$	0	0	-1	0	0
Bottom	b	4180^{+30}_{-30}	$\frac{1}{2}$	$+\frac{1}{3}$	$-\frac{1}{3}$	0	0	0	-1	0
Top	t	160000^{+5000}_{-4000}	$\frac{1}{2}$	$+\frac{1}{3}$	$+\frac{2}{3}$	0	0	0	0	+1

Of particular interest to this thesis is a peculiar behavior of quarks called confinement, which is an immediate result of the strong nuclear force. To illustrate this, one often considers the limiting case of a bound quark- anti quark pair (a meson); its interaction potential is given by the Yukawa attractive potential as one might expect, but with an additional attractive linear term that arises from the one dimensional color flux between the quarks in a way analogous to an electromagnetic dipole in quantum electrodynamics (QED). Unlike QED, however, the color field vanishes outside the color flux tube, giving the linear term that is responsible for confinement. Explicitly, the one dimensional two body approximation of the color field is given by [3]:

$$V(r) = -\frac{4}{3}\frac{\alpha(\mathrm{r})}{r} + Kr \tag{1.1}$$

Indeed, when the string tension is taken to be $K \cong 1$ GeV/fm, this describes the heavy quarkonia emission spectrum quite well [4]. From this, it can be observed that in the limit of large r, the attractive term vanishes and the linear term diverges to arbitrarily large energies. However, in practice when the potential energy reaches the rest mass of a new quark – antiquark pair, the virtual quark-antiquark pair produced in the vacuum become real and a new meson is created. As such, no free quarks have been observed in isolation [5]. It is therefore said that quarks are only observed inside of hadrons and are thus confined.

However, that is not the end of the story. At sufficiently high density and temperature, other nearby quarks begin to interfere with the local form of the color field and, when taken together, have the effect of screening the color field that bind hadrons [5]. With the color field suppressed, quarks gain the ability to decouple and reassociate conductively throughout the medium in a phenomenon called deconfinement. This asymptotic freedom is the sign of a new state of matter that will be the focus of the remainder of this thesis.

1.1.2 The Quark-Gluon Plasma

The Quark-Gluon Plasma (QGP) is a quantum chromodynamic (QCD) phase characterized by deconfinement of quarks and gluons as well as temperature and baryon density well beyond that of ordinary cold nuclear matter. Particularly, theoretical description of QCD matter show novel properties comparable to the QGP at energy densities in excess of 1 $\frac{GeV}{fm^3}$ [6], but an exact parameterization of the phase boundary has only been investigated in certain energy subspaces to date. Fig. 1.1 illustrates the phase transition boundary.

Lattice QCD theoretical models which compute the high temperature limit of the equation of state predict a sharp change in the Stephan-Boltzmann energy density around a value of $T \cong 170$ MeV as well as asymptotic freedom and chiral symmetry restoration; all of which are distinct signatures of the QGP. Experimental observations of thermal photons at the Relativistic Heavy Ion Collider (RHIC) have confirmed and refined these models to provide even more strict limitations on the temperature [8]. The phase transition predicted therefore appears consistent with a first order phase transition; in addition, SU(3) gauge theory also predicts this type, but the presence of more flavors confounds that prediction. As such, the exact phase transition type is unclear [9].

The extremes of the temperature and density energy constraints make this state of matter quite rare in nature. It is thought to have existed in the earliest moments of the universe, as well as in the present day in certain exotic celestial objects such as quark stars where the gravitational collapse of stellar matter yields pressures comparable to what is required for the QGP to form [10]. On Earth, however, we are limited in our laboratory study of the QGP to particle accelerators which collide heavy ions at speeds close to the speed of light, such as the Super Proton Synchrotron (SPS) at the European Center for Nuclear Research (CERN) in Geneva, Switzerland. An illustration of such a collision is available in Fig. 1.2. On February 10, 2000, the SPS experiment announced the creation and observation of a new state of matter

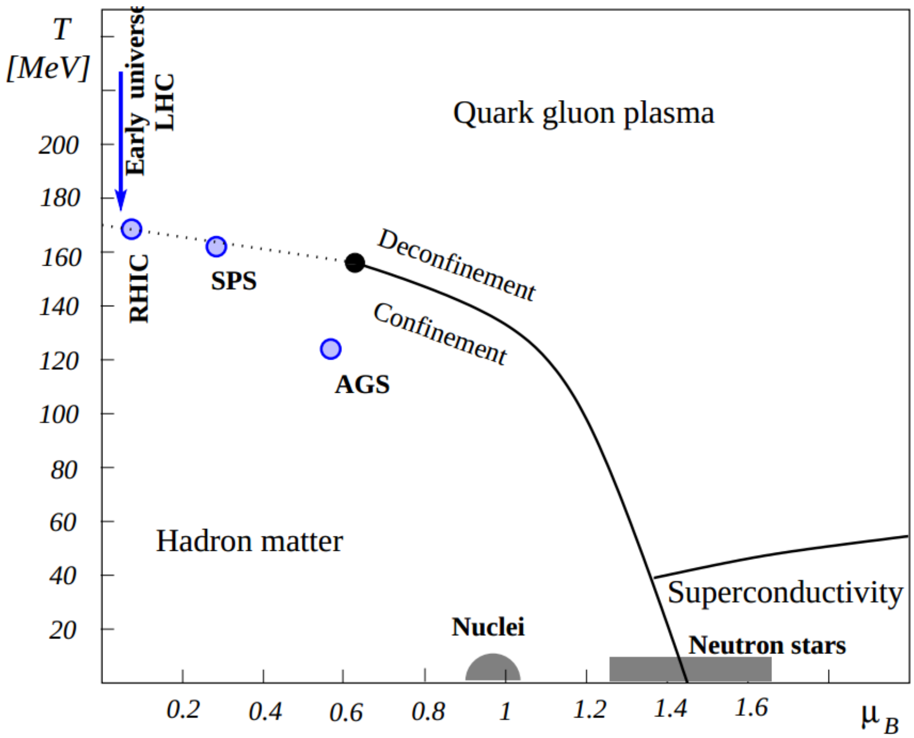

Figure 1.1. The nuclear matter phase diagram. Here, the horizontal axis is the average baryon density and the vertical axis is the temperature in MeV as measured from the exponential of the strong nuclear coupling constant, $\alpha(r)$. An exact parameterization of the phase transition for all points in space is not known, and is thus represented as a dotted line here. Experiments like SPS, RHIC, and the LHC are capable of passing this line during heavy ion collisions. [7]

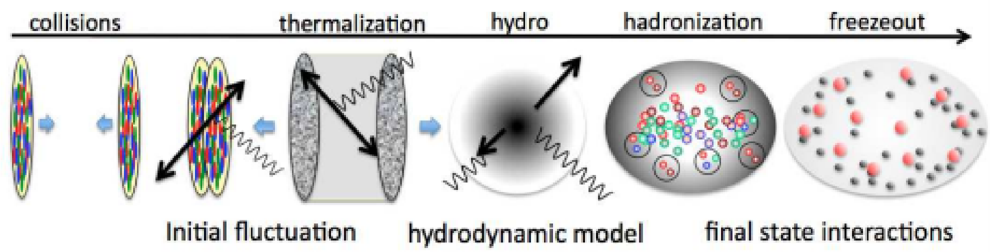

Figure 1.2. Step by step evolution of a heavy ion collision. See section 1.3 for a summery of the timeline. [12]

consistent with the QGP [11]. This observation has since been recreated and verified by the Relativistic Heavy Ion Collider (RHIC) [6].

Because of the very high particle multiplicity and femtoscopic characteristic length scale of relativistic heavy ion collisions in these experiments, a system of theoretical techniques and numerical simulations are used to compute essential observables such as the impact parameter or participating nucleons in a single collision event that would otherwise be difficult, if not impossible, to directly measure. Collectively, these techniques are the Glauber Model [13]. The Glauber model itself makes use of the parton distribution functions, skin depth, nucleon-nucleon cross section, and other experimental observables to put together a comprehensive relativistically corrected quantum picture of the collision. However, it is often enough to consider only the optical limit of the Glauber model to formulate a pseudo-classical view of a heavy ion collision, such in Fig. 1.3.

1.1.3 Time Evolution of a Heavy Ion Collision

It is instructive to examine in specific detail the known features of a heavy ion collision's evolution in time and define a few useful terms that will be used later in this thesis to characterize the experiment.

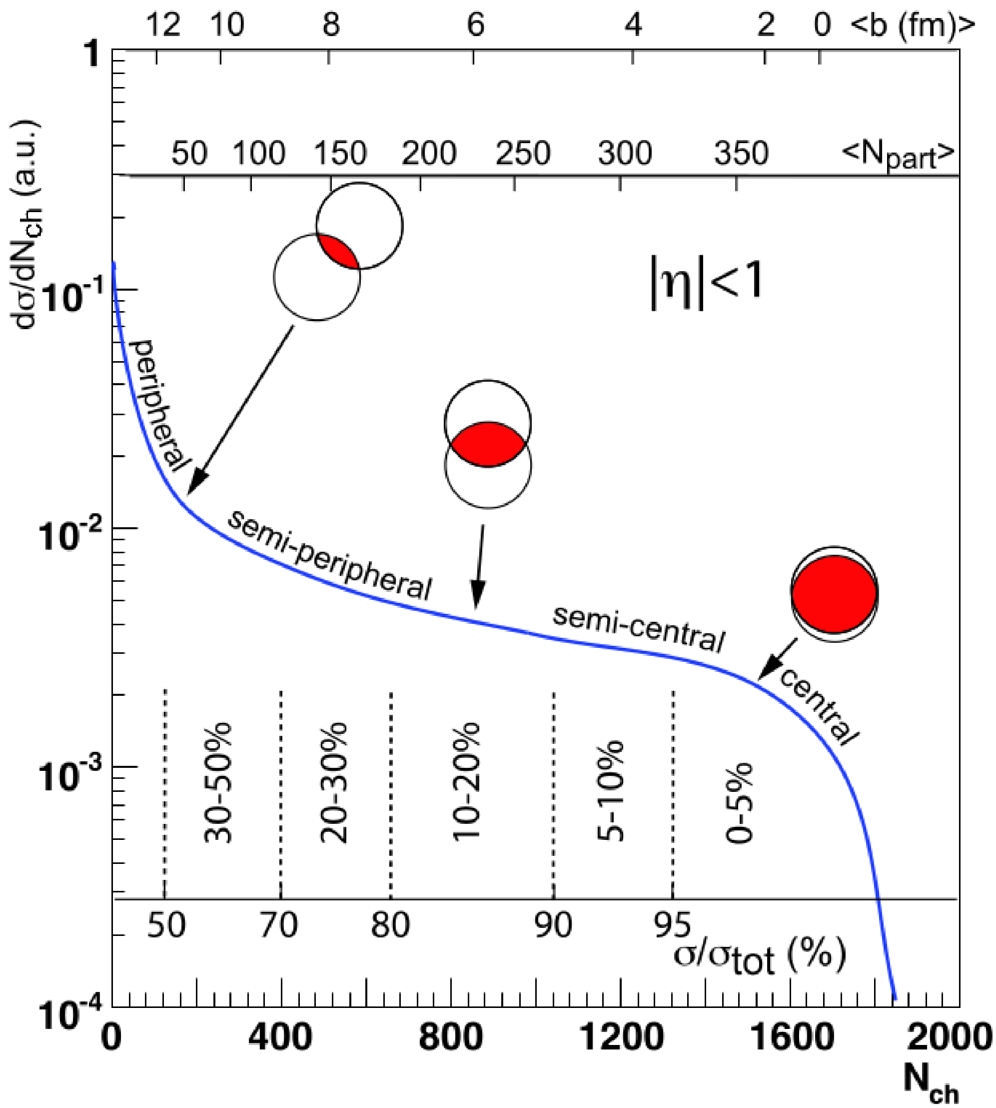

Figure 1.3. Illustration of heavy ion interaction cross section versus impact parameter according to the Glauber Model. Observe that according to the Glauber Model, impact parameter, centrality, and produced particle multiplicity will show a direct dependence. Also note that the values shown are for illustrative purposes only, and not an actual measurement. [13]

As the constituents of a heavy ion collision are moving relativistically, it's useful to consider the particle bunch crossings as events in Minkowski space; like a light cone (see Fig. 1.4). According to the Glauber model in the optical limit, the participating nuclei will be Lorentz contracted into disks in the lab frame that travel along the direction of the beam line. In the two dimensional space spanned by the azimuth, the disks will overlap as they travel toward each other. At the time of the collision, the partons within the overlap area will be participating partons, while those outside are spectators; the latter will quickly disperse in a spray of radiation along the beam line [15]. It's worth noting that the orientation of the overlap area (that is, the event plane) are important experimental observables for studies of coordinate phase space distributions of hadrons; as will be discussed in more detail in section 5.2.

Although the exact temporal dynamics of a heavy ion collision are unknown (see section 1.4.1), some theoretical models have been proposed which try to describe the collision. One such model based on a hydrodynamic interpretation of the QGP; what follows is a brief description of the approximate time evolution in the hydrodynamic model. After the initial collision, there is a short equilibrium phase during which hard partons from their respective ions will interact and multiply. At times less than 0.3 fm/c, gluon-gluon interaction will dominate, and they will locally thermalize into small clusters. The clusters then expand and merge into a hot nuclear medium, with hard quarks intermixed. Then, as the hard quarks interact with the thermalized gluons, they will themselves thermalize on a scale roughly 2-3 times longer than the quarks due a smaller interaction cross section from their color coefficients [16]. When the system thermalizes, the chemical composition (that is, the flavor ratios) of the products have been fixed. At this point it is argued that a new state of matter has been created that is consistent with the QGP [6]. This hot and dense nuclear material then expands and cools for another $\sim 4-6$ fm/c before hard partons begin to separate from the medium and again undergo hadronization [17]. Each particle species will hadronize at different times depending on their mass; with the harder partons leaving the medium first and subsequently hadronizing into heavier products

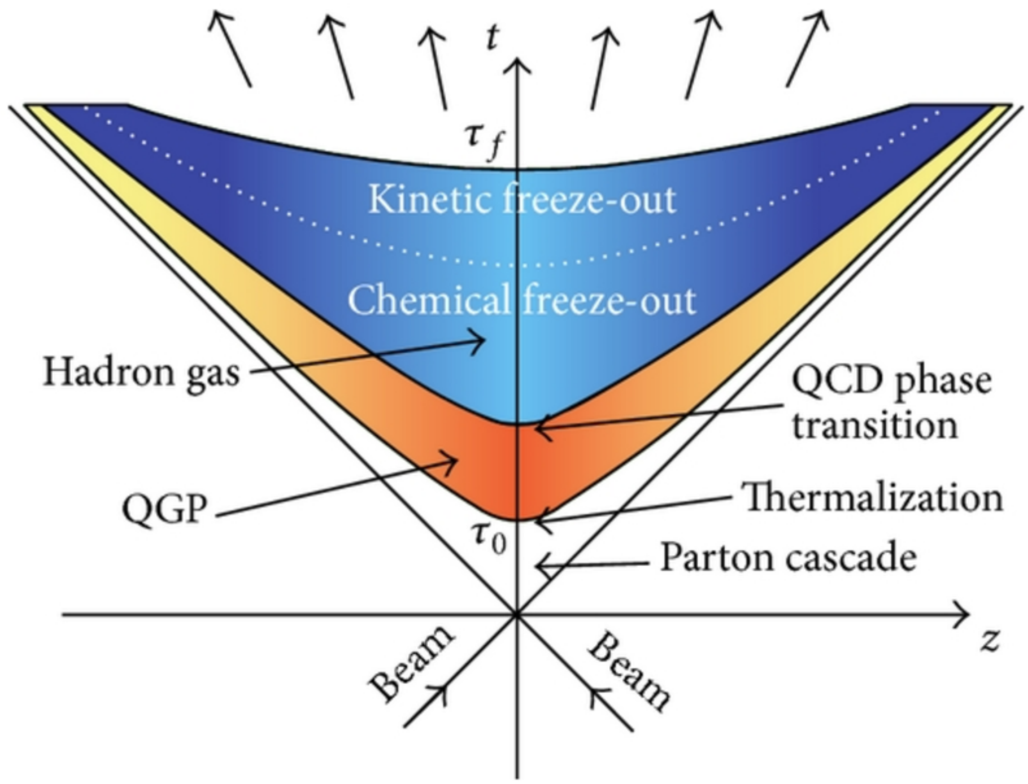

Figure 1.4. This figure illustrates a heavy ion collision in coordinate phase space with the azimuth and radial distance suppressed. Here, let the diagonal lines represent the position of spectator ions traveling along the beam line. The hyperbolas are meant to denote major epochs in the evolution of the nuclear material. [14]

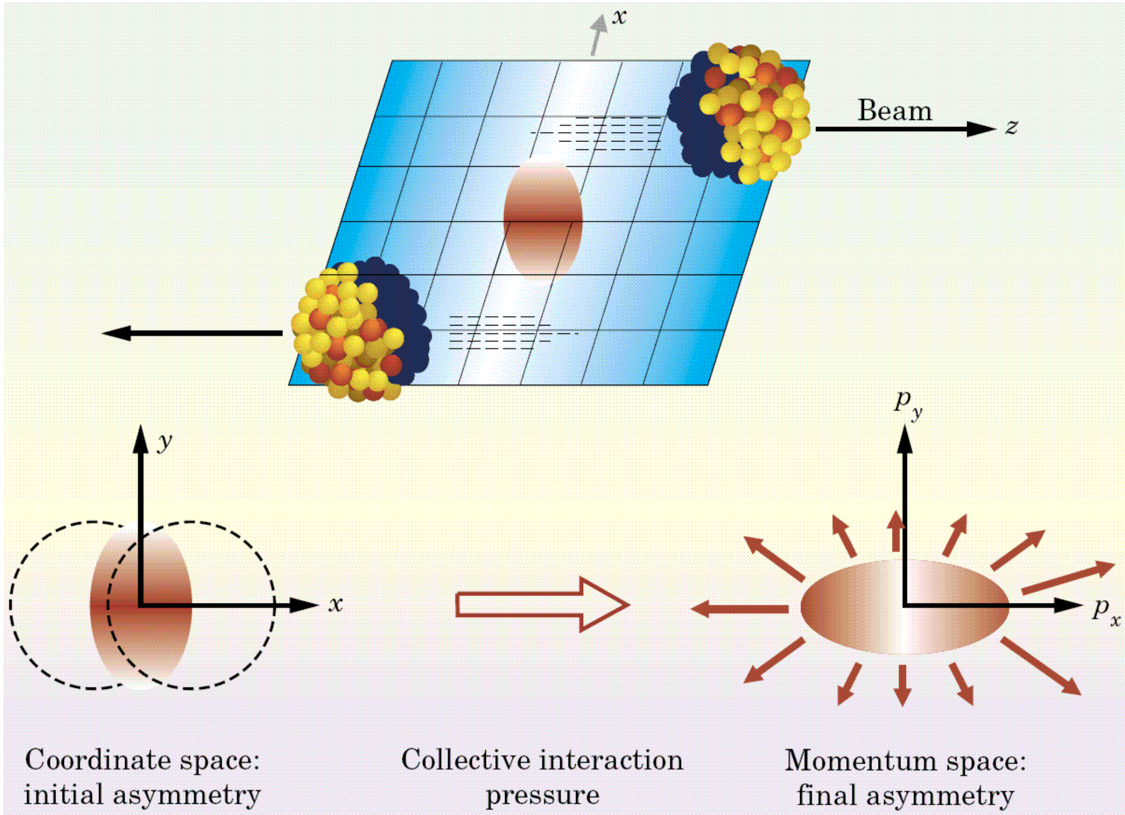

Figure 1.5. Illustration of collision and participant medium in coordinate and momentum phase space. Note the orientation of the plane of interaction. [19]

to conserve four momentum. When the last parton has hadronized, that is referred to as chemical freeze out.

An even longer time may pass, however, before the baryon density drops far enough for the hadrons themselves to stop interacting with each other, called kinetic freeze out. After kinetic freeze out, it can be said that the heavy ion collision has reached its final state [1] and meaningful observations of the products can be performed.

In light of the many successful theoretical models and experimental observations of the QGP, a casual reader might think that it is well understood, but there are

[1]Of course, the final products themselves might subsequently decay prior to being observed, but there exist experimental methods to reconstruct the final state with good accuracy. We'll discuss this in more depth in later sections.

still many unanswered questions about the QGP that must be addressed. In order to tackle these questions, specialized facilities have been constructed around the world in order to observe heavy ion collisions in unprecedented accuracy.

1.2 The ALICE Experiment

1.2.1 The LHC

The Large Hadron Collider (LHC) on the border of Switzerland and France near the city of Geneva successfully navigated its first ion beam around the full 27 kilometers of its circumference on September 10, 2008. See an illustration in Fig. 1.6. This makes it the largest existing circular particle collider in radius and maximum collision energy. It is managed by the Center of European Nuclear Research (CERN), and has seven ongoing experiments at access points periodically spaced around the ring. The mission of the LHC is to test various existing theoretical descriptions in particle and nuclear physics in a new high energy regime.

After its first three years of run time, the LHC delivered nearly 30 fb^{-1} of total integrated proton-proton luminosity to the ATLAS and CMS experiments in the search for the Higgs Boson [20]. In addition, it achieved its maximum pre-upgrade collision energy of $\sqrt{s_{NN}} = 7$ TeV in proton-proton collisions and $\sqrt{s_{NN}} = 2.76$ TeV in lead-lead collisions. This is still only a fraction of its maximum design energy of $\sqrt{s_{NN}} = 14$ TeV in proton-proton and $\sqrt{s_{NN}} = 5.74$ TeV in lead-lead collisions. More than one 1,200 members have contributed to the project from over 130 institutes around the world, making the accelerator truly global in scope [21].

1.2.2 The ALICE Experiment

The A Large Ion Collider Experiment (ALICE) is one the of experiments at the LHC. ALICE was optimized to study heavy ion collisions at $\sqrt{s_{NN}} = 2.76$ and $\sqrt{s_{NN}} = 5.74$ TeV and thus makes use of a larger number of detectors with more

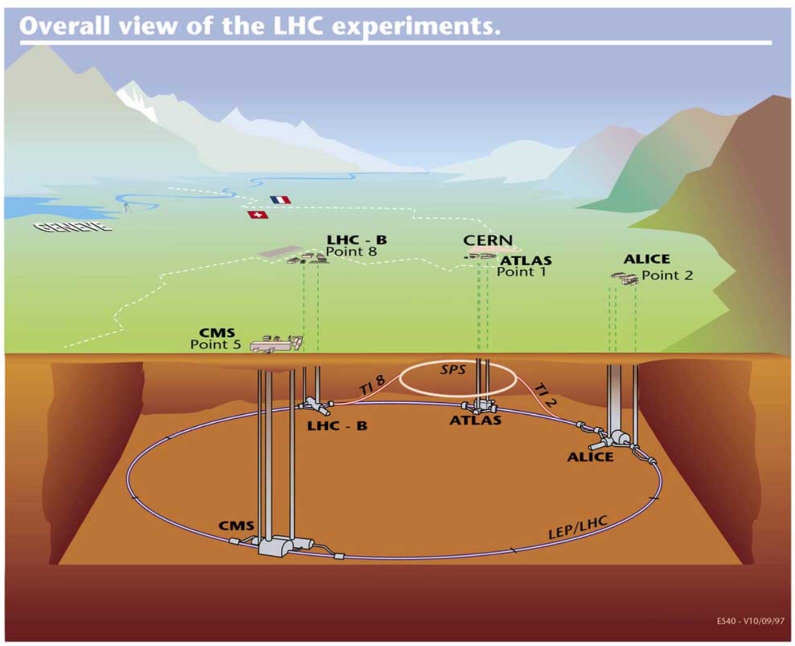

Figure 1.6. Pictorial Schematic of the LHC under Geneva. The main ring is 27 km in diameter and is capable of pp collisions with center of mass energy of up to 14 TeV. [18]

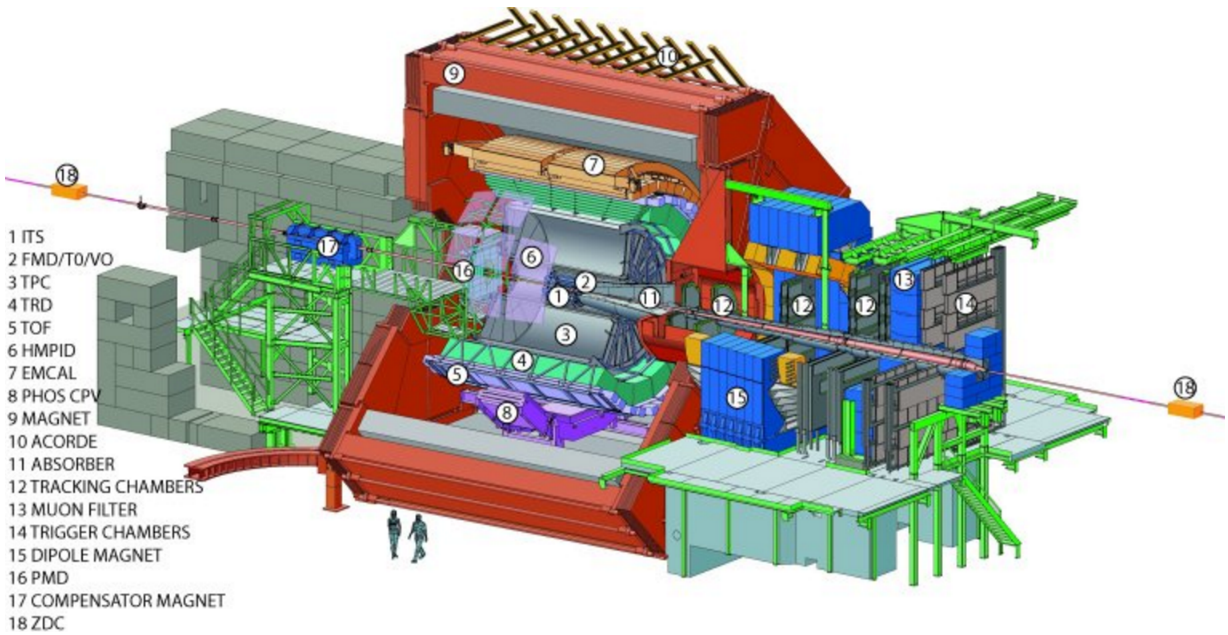

Figure 1.7. Pictorial schematic of the ALICE experiment at Point 2 of the LHC. The PHOS detector can be seen as the purple arm at the bottom of the detector. The TPC is the gray and teal barrel in the center. [21]

limited acceptance than some other LHC experiments in order to provide access to a wider scope of observables. An illustration of ALICE cut away allows one to see the experimental setup (Fig. 1.7).

Since a single heavy ion collision can result in a very high product particle multiplicity and bunch crossings at the LHC occur on the scale of nanoseconds, the rate at which data is produced is quite high; around 2.5 GB/s, or 1 PB per year [22]. To cope with this, ALICE makes use of the worldwide computing network called the GRID.

1.2.3 Relevant Detectors

The Photon Spectrometer (PHOS) is an ALICE detector that was designed explicitly to study gamma radiation produced in the heavy ion collisions. It consists of three modules of 3584 rectangular prism lead tungstate ($PbWO_4$) crystals with dimensions 22x22x180 mm^3 arranged in a 56x64 grid. The detector is 4600 mm radial distance from the interaction point and has an acceptance of $|\eta| \leq 0.12$ in pseudo-rapidity and $\Delta\phi = 60^o = 1.05$ radians in azimuthal angle. The lead tungstate crystal was chosen because of its ability to almost immediately (usually within a few millimeters) induce an electromagnetic shower when exposed to ionizing radiation. After induction, the shower will lose energy at a rate proportional to $E_{shower} \propto e^{\frac{-x}{X_0}}$ on average, where X_0 is the radiation length. The crystal's radial length covers adequate shower length (10 X_o) to differentiate neutral pion identification using an invariant mass analysis. Energy deposited in a cell by a shower is extracted via fiber optic wave guides to a series of photomultiplier tubes where the light is converted to an electric analog signal and measured. The detector uses three criterion to discriminate photons from charged hadrons with a high efficiency: a shower shape analysis (each crystal cell covers only half a radiation length), a time of flight cut (resolution 1 ns at 1-2 GeV), and charged particle track matching in the TPC [23,24]. A more detailed description of the use of this detector will be covered in later sections.

Complimenting PHOS is the Time Projection Chamber (TPC). The TPC barrel covers $|\eta| \leq 0.9$ in pseudorapidity, but as high as $|\eta| \leq 1.5$ with reduced track length and the full azimuth. It has radial dimensions of $0.845 < \mathrm{r} < 2.466$ m (active volume), making it the biggest TPC in the world to date. It uses a mix of Ne/CO_2 gas (90/10%) is used, which correspond to roughly 3.5% X_0 in radial track length. A drift field of 400 V/cm is applied creating a drift velocity of 2.84 $cm/\mu s$ (maximum drift time of 88 microseconds). It can detect particles with up to 100 GeV/c in transverse momentum with good resolution and position resolution on the order of millimeters. The TPC is used in the High Level Trigger (HLT) of ALICE in addition to its track finding role [22–24].

Although the PHOS and TPC will provide the majority of data considered in this thesis, the V0 detector will provide an essential measurement of centrality and the event plane measurement. The V0 detector is segmented into V0A and V0C (on

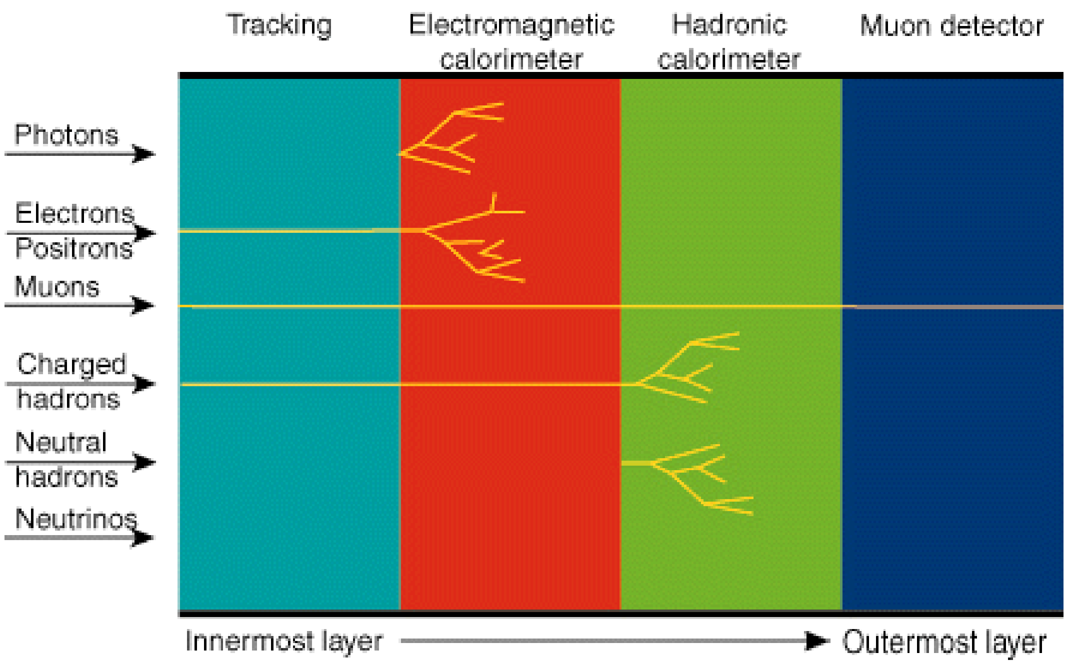

Figure 1.8. Illustration of path as various particle species travel radially outwards from the center of ALICE.

the south and north sides of ALICE, respectively). They are both located 340 cm from the interaction vertex and are inside the L3 magnet. They are located along the beam line and are divided into eight sections of $\frac{\pi}{4}$ in azimuth and four sections in psuedorapidity. Each section consists of scintillator plastic with embedded wavelength shifting fibers. [15]

In Fig. 1.8, an illustration of the paths of various particle species traversing the ALICE experiment radially outward is shown.

1.3 Direct Photons

1.3.1 Direct Photon Properties

The experiment and detectors described previously allow one to analytically isolate direct photons. Direct photons are defined as any photons created in a heavy ion collision after thermalization of the system but before kinetic freeze out. In other words, they are photons not created by hadronic particle decays. Since photons are largely non interacting after hadronization, the information carried by them is unperturbed by other decay products or intervening materials and fields prior to reaching a scintillating detector such as PHOS. As such, direct photons have long been considered an ideal probe of the QGP [34].

When studying direct photons, the primary source of background is neutral meson decay. At the ALICE experiment, neutral pions make up a nontrivial ratio of the produced particle species, and typically decay to the 2γ channel with $\Gamma_{\pi^0\to\gamma\gamma}/\Gamma_{\pi^0} = 0.98798$ [27] on a characteristic length scale of ~ 22 cm. As such, π_0 decay dominates the photonic background in heavy ion collisions. Another neutral meson that non trivially contributes is the η with $\Gamma_{\eta\to\gamma\gamma}/\Gamma_\eta = 0.3941$ [27]. Roughly 88% of the decay mesons are from neutral pions, while 10% are from etas [73]. Much less commonly, other diphoton meson decays can contribute as well, such as the $f_0(600)$, but these are considered to be negligible. With these sources in mind, it is possible to isolate direct photons with a high purity by using the double ratio method.

1.3.2 Categories of Direct Photons

The actual emission source of photon is independent of its classification as direct, but intrinsically direct photons can be subdivided according to their source. The most common [26] sources of direct photons include prompt photons, jet-medium interactions, and thermal photons.

Prompt photons are created in hard QCD processes, and can we well characterized by next to leading order (NLO) pQCD. They are by far the most common subtype of direct photons in pp collisions, but their signal does scale with participating nucleon number in AA collisions.

There are also Jet-Medium photons, created by hard parton interaction with thermalized partons to create in medium bremsstrahlung. This subcategory is often accompanied by a jet, as the name suggests.

Finally, scattering of thermalized partons with other thermalized partons may create thermal photons via $q\bar{q} \rightarrow g\gamma$ or $qg \rightarrow q\gamma + NLO$. This last subcategory is characterized by its low p_t when compared to the hard QCD processes, and is interesting as an indicator of bulk QGP properties. Although this thesis will attempt to use the most explicit language possible, we will concern ourselves primarily with this last category when we speak of direct photons.

1.3.3 Direct Photon Isolation Methods

Direct photons can be observed using the so called "double ratio" method. This method exploits the primary source of background, the neutral pion decay channel, and uses it as a benchmark to cancel a large number of systematic uncertainties in the spectrum measurement. Mathematically, it is straightforward:

$$\gamma_{dir} \equiv \gamma_{inclusive} - \gamma_{decay} = \gamma_{incl}(1 - \frac{\gamma_{decay}}{\gamma_{incl}}) = \gamma_{incl}(1 - \frac{1}{R}) \tag{1.2}$$

Where

$$R \equiv \frac{\gamma_{incl}}{\gamma_{decay}} = \frac{\frac{\gamma_{incl}}{\pi^0_{data}}}{\left[\frac{\gamma_{decay}}{\pi^0}\right]_{MC}} \tag{1.3}$$

γ and π represent the photon and pion spectra, respectively, and the subscripts denote the source subcategory. The assumption is made that the pion spectrum is well described by Monte Carlo such that the substitution in the denominator is valid. Previous studies of the π_0 spectrum in Monte Carlo provide confidence that this assumption is justified [28, 29]. Therefore, all that is needed to compute R is the measurement of the inclusive photon spectrum and a measurement of the pion spectrum for a given data set. It can be seen that when R $>$ 1, we have detected a number of direct photons. The direct photon invariant yield, then, is given by:

$$\frac{dN_{dir}}{p_t dp_t d\eta d\phi} = \frac{dN^{\gamma incl}}{p_t dp_t d\gamma d\phi} \frac{R-1}{R} \tag{1.4}$$

with the inclusive photon spectrum computed via the normal:

$$\frac{dN^{\gamma incl}}{p_t dp_t d\gamma d\phi} = \frac{1}{2\pi}\frac{1}{p_t}\frac{\mathcal{P}}{\mathcal{E}_{eff}}\frac{dN^{raw}}{dp_t} \tag{1.5}$$

where $\mathcal{P}$ and $\mathcal{E}_{eff}$ is the purity and effective efficiency of the photon selection algorithm, respectively, and $\frac{dN^{raw}}{dp_t}$ is just the raw photon spectrum.

At ALICE, there are two methods to identify the needed raw photon spectrum in the low p_t (thermal photon) regime. Since the PHOS detector was explicitly designed with photon studies in mind, it is ideal for this analysis and thus it is used extensively. In the PHOS method, photons are isolated from charged particles and hadrons using a series of cuts. As previously mentioned, these cuts include charged particle track matching in the TPC as well as a shower shape cuts based on the deposited energy dispersion matrix. More details are provided in section 4. In addition to the PHOS method, the photon conversion method (PCM) searches for photon decay to $e^+ + e^-$ pair in the TPC. In practice, each method is used as a cross check of one another, and by looking at the two methods it is possible to estimate systematic uncertainties in the spectrum. Finally, whichever method is used to measure the inclusive photon spectrum, the experimental π_0 yield (in the numerator of Equation 1.4) can be observed directly using the usual diphoton invariant mass. The denominator can be found using a HIJING simulation of π_0 production in the ALICE detector geometry.

1.3.4 Direct Photon Observations at PHENIX

Direct photons have long been considered a ideal probe of the QGP [34] precisely because they only interact electromagnetically and are thus considered to traverse the strongly quantum chromodynamically interacting medium with a large mean free path. This line of reasoning culminated in a famous measurement by the PHENIX experiment in 2008 [34] whose primary results can be seen in Fig. 1.11.

It can be seen that, indeed, direct photons seem to not be suppressed in the medium; the "photonic" suppression factor is consistent with unity, indicating no

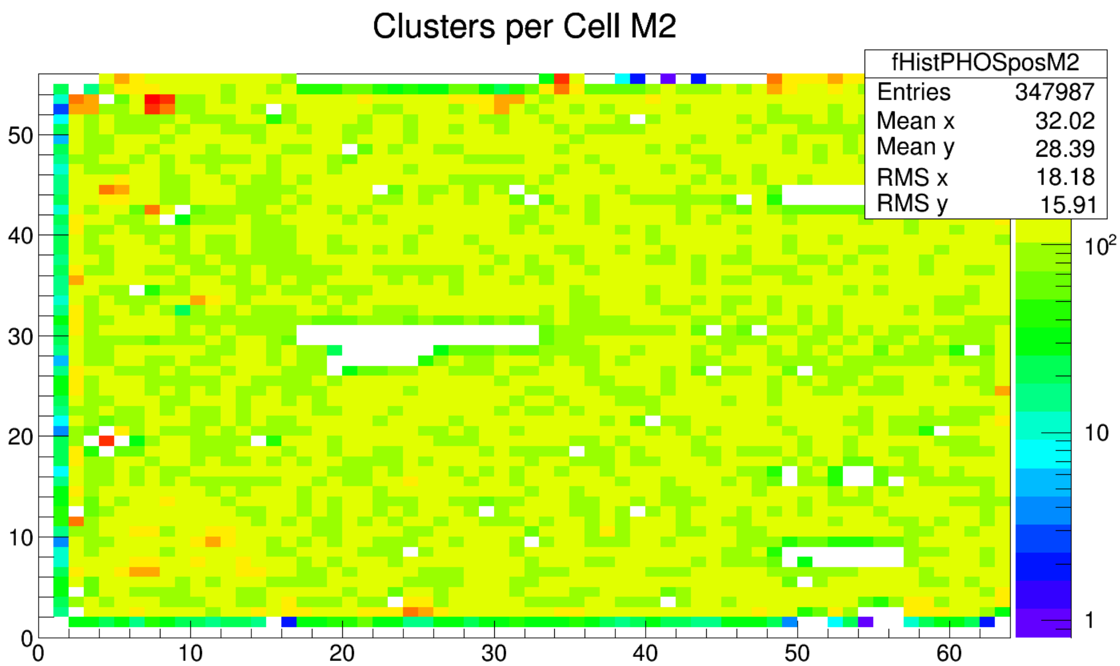

Figure 1.9. PHOS raw cluster energy plot in module 2. Each pixel is the raw average energy deposited in a cluster centered on the cell. It is easy to see cell by cell fluctuations because of differences in individual calibration and other causes. Much of the PHOS analysis focuses on normalizing or cutting away these effects.

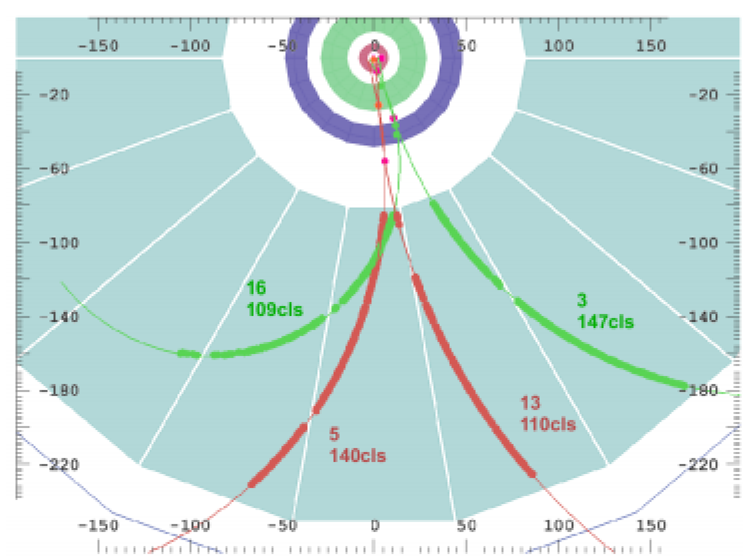

Figure 1.10. TPC display of a real event, highlighting a few detected electrons. It can be observed that extrapolating the trajectory of the matched electrons back to their overlap suggests the presence of a secondary vertex such as the decay of a neutral pion. The PCM method attempts to identify which electrons come from these secondary vertices and by extension identify direct photons. [25]

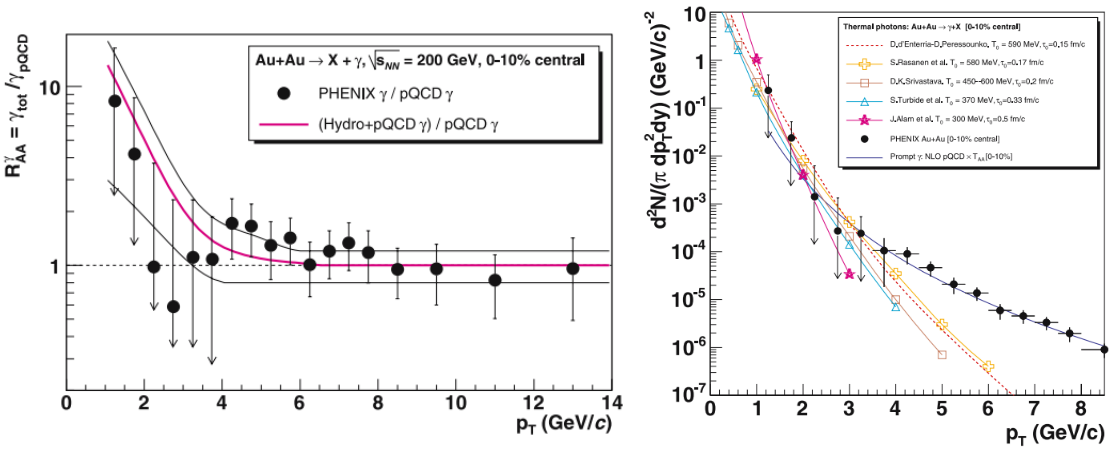

Figure 1.11. PHENIX study of direct photon suppression. [34]

suppression. Since the direct photon yield is consistent with expected results from pQCD, the assumption of pQDC - that there exists a large mean free path of products - is assumed to be true of direct photons. However, this result only holds above roughly $p_t > 4 - 5$ GeV/c, meaning that its result only applies to prompt and jet-medium photons, and explicitly excludes the thermal photon regime. It is possible that thermalized photons *do* have a low mean free path in the QGP, just like partons. Nevertheless, the PHENIX study has shed significant light on photon interaction in the QGP and raised many of the question posed in section 1.4.

1.3.5 Direct Photon Elliptical and Triangular Flow Measurements at ALICE

Previous direct photon studies at ALICE has been successful in computing the direct photon spectrum [29] and both v_2 and v_3 flow [38] (see 5.2.1 for a brief description of flow). These analysis studied lead-lead collisions at center of mass energy 2.76 TeV (the benchmark for lead-lead experiments at ALICE prior to 2015). Their results can be seen in Figs. 1.12, 1.13, and 1.14 respectively.

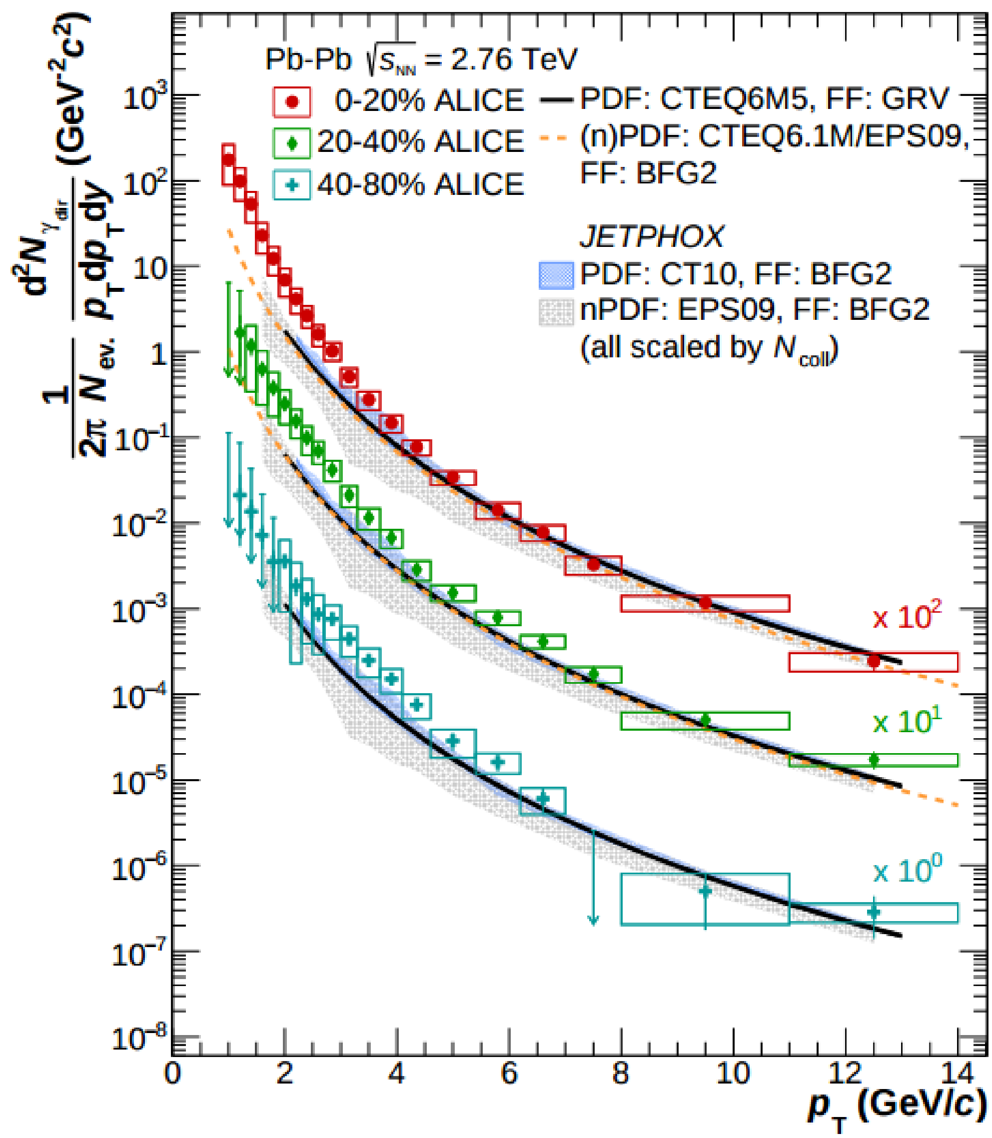

Figure 1.12. Direct photon spectrum in PbPb at 2.76 TeV collision energy observed by ALICE. [29]

These flow harmonics studies did not go to higher than third order in v_N and were not compared to proton-proton results as PHENIX did. Nevertheless, they serve as an effective methodological foundation for further study. The specific methodological details used in this thesis and how they differ from these studies will be discussed primarily in section 2.1.

1.4 Open questions

1.4.1 Meaning of the Temperature

In section 1.1.3, a rough timeline of the QGP was presented which was based on a hydrodynamic model. However, this is certainly not the only model which is available [39]. Indeed, because of the femtosecond timescale involved, the time evolution of the QGP is effectively impossible to quantitatively measure directly and even indirect observations of the QGP temporal dynamics are nontrivially difficult to interpret. Regardless, the hydrodynamic model provides a general timeline [16] from which to perform a useful analysis. For this reason alone the hydrodynamic timeline will be the primary one discussed in this study.

Of particular interest is the meaning of the thermal photon spectrum's inverse slope parameter measured in thermal photons studies at both the LHC and RHIC [26, 40]. The spectrum's inverse slope parameter is, as the name implies, simply the inverse slope parameter in a simple exponential fit of the low p_t direct photon spectrum, $\frac{\delta N}{\delta p_t} = Ae^{\frac{-p_t}{T}}$. Thermodynamically, this is understood to be the temperature of the observed media [41, 42]. However, some hydrodynamic models suggest that the correlation between the measured inverse slope parameter and the temperature of the system at thermalization is not necessarily a linear function [43]. Furthermore, one insists that throughout the evolution of QGP it is continuously expanding and cooling [5]; therefore, providing any one temperature as "the temperature of the QGP" is a fundamentally flawed idea. This ambiguity comes from the fact that it's unclear exactly when in the evolution of the activated nuclear matter the majority of thermal

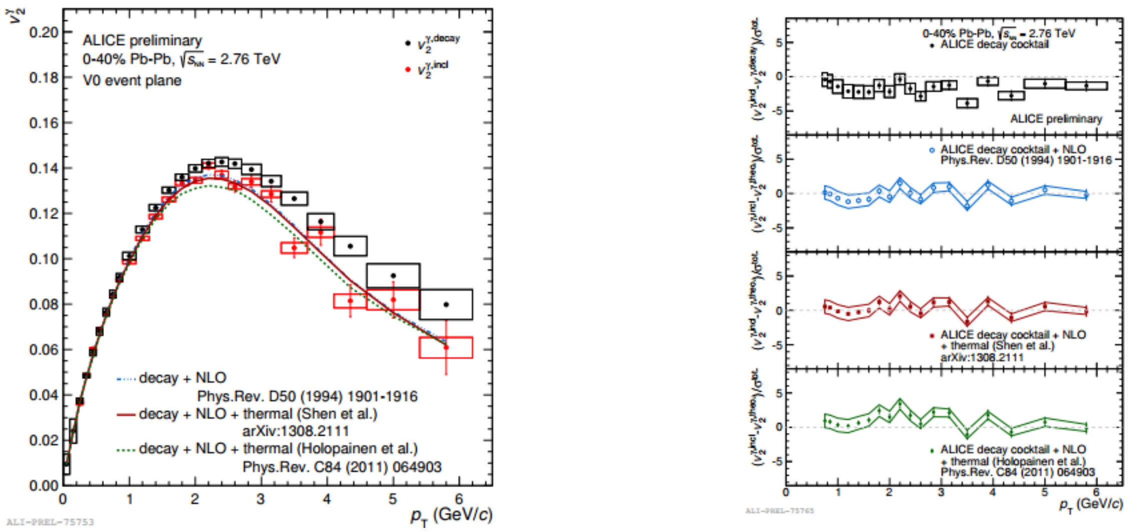

Figure 1.13. Direct photon v_2 in PbPb at 2.76 TeV collision energy observed by the ALICE Collaboration. [38]

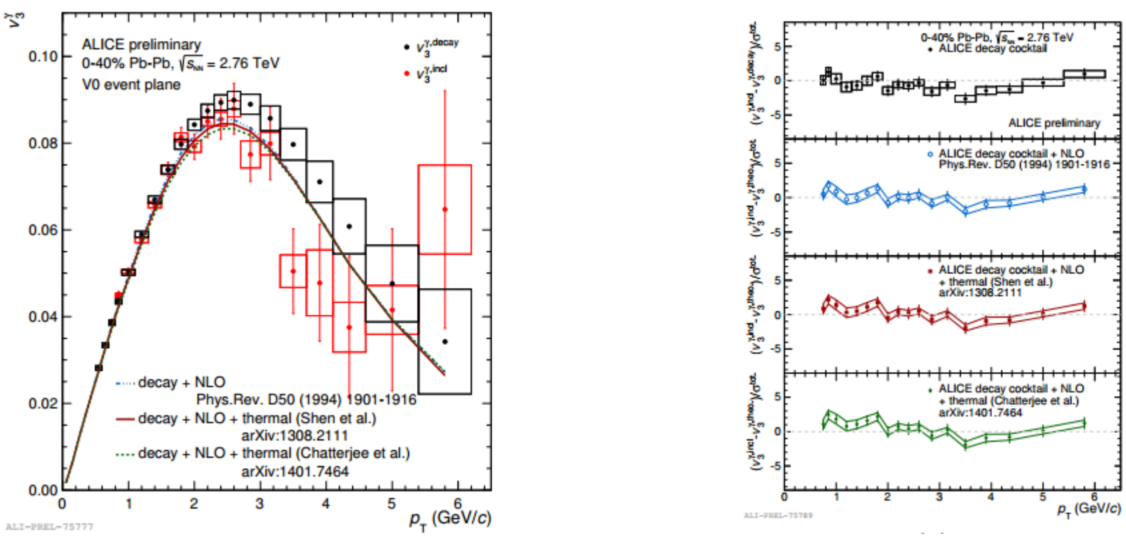

Figure 1.14. Direct photon v_3 in PbPb at 2.76 TeV collision energy observed by the ALICE Collaboration. [38]

photons are emitted. If it's early in the collision (immediately after thermalization, for example), then the measured inverse slope parameter is most likely higher (indeed - significantly higher) than the phase transition temperature as is suggested by the hydrodynamic model [44]. If, by contrast, emission happens mostly very late in the collision such as immediately prior to chemical freeze out then perhaps it is a very good indicator of the transition temperature.

It is suggested to the reader that the ambiguity of the meaning of the temperature measurement is fundamentally tied to the ambiguity of the time evolution of the QGP. If it were somehow possible to determine roughly when in the collision thermal photons were emitted (the thermal photon yield as a function of time), then the thermodynamic temperature derived from those photons would have specific physical meaning. Presently, however, no experimental analysis has been done to shed light on this question. This thesis will attempt to probe the activated nuclear system's temporal dynamics by examining the properties of thermal photons.

1.4.2 Photonic Suppression

First, it will be necessary to confirm that thermal photons are indeed non interacting in the nuclear plasma. While the PHENIX experiment did indeed verify that most direct photons are unperturbed by the plasma, these results crucially did not extend to thermal photons (see 1.3.4 for much more details). Therefore the first task will be to reproduce the PHENIX results at low transverse momentum.

To do this, one will use an important observable in heavy ion collisions for any product particle species: the nuclear suppression factor, R_{AA}. Perturbative quantum chromodynamics very accurately predicts the relative yields of different particle species in high energy interactions [5]. However, pQCD (represented by Feynman diagrams) assumes a large mean free path between interaction vertices, and thus ignore transient effects in the wave functions of intermediary particles in the plasma [45,57]. In strongly interacting quantum plasmas like the QGP, there is a short mean free path between interacting partons which nontrivially reduces the yield of many charged product particles [45]. This yield reduction is called the "nuclear suppression factor", R_{AA}, and is mathematically enumerated as simply the ratio of the observed charged particle yield to the expected yield from pQCD scaled by the number of participating nucleons as predicted by Glauber:

$$R_{AA}(p_t) = \frac{dN_{AA}^{total}/dp_t}{\langle T_{AA}\rangle \, d\sigma_{pp}^{pQCD}/dp_t} \tag{1.6}$$

This has been well studied for light hadrons and electrons, and a nontrivial hadronic nuclear suppression is detected [46]. These results might well be expected: partons are known to be strongly interacting in the medium and correspondingly have short interaction distances.

If thermal photons are observed to be suppressed in the medium similarly to partons, then this short interaction distance must be considered when interpreting the temperature measurements that use those same thermal photons. Namely - that they have been perturbed while traversing the medium and are thus no longer indicative of interactions early in the collision. By contrast, if - like the high p_t direct photons observed by PHENIX - they are not suppressed, then one can be confident that the thermal photons that we detect are more or less the same as when they were generated after thermalization. Either way - the information will be useful to our examination of the heavy ion collision timeline. Certainly, our analysis of the properties of thermal photons must include a measurement of the thermal photon nuclear suppression.

1.4.3 Flow of Direct Photons

In addition to the hadronic nuclear suppression, many believe observation of hadronic azimuthal anisotropy (more often called simply "the flow") to be of particular interest when probing the QGP's behavior [58]. Flow measurements use high order Fourier transforms of the azimuthal coordinate phase space product hadron distribution to search for patterns in the interaction of various partons in the QGP.

In particular, some are curious about when partons with zero isotopic spin are formed in the QGP and seek to observe the dynamics of such partons using flow measurements [59].

If these hadronic flow measurements bare similarities to thermal photon flow measurements, one might argue that the life of a thermal photon in the QGP is comparable with the life of that heavy flavor. Thus, previous heavy flavor flow measurements could be used as an uncalibrated benchmark in discussions about thermal photon temporal evolution. Note that while direct photon flow has been studied thoroughly in the past (see a complete discussion of those results in section 1.3.5), it is worthwhile to verify and compare these results with hadronic flow studies as a second source of information regarding the thermal photon timeline [29].

Since many of the same tools used to study direct photon suppression can also be used to study direct photon flow, it seems natural to include these measurements in this analysis as well.

1.4.4 Proposal and Purpose

With these three open questions about the Quark Gluon Plasma in mind, I suggest the following: I will measure the thermal photon spectrum, suppression, and flow using the ALICE photon spectrometer. Then I will use the measured data and comparison to known hadron results to estimate when in the QGP evolution narrative provided by hydrodynamics most thermal photons stop interacting with the medium. If thermal photons stop interacting with the plasma early, as is historically suspected, one expects a low nuclear suppression factor and a flow mirroring heavy flavor flow measurements. By contrast, if thermal photons continue to interact long after thermalization such as soft partons, then one expects to see high thermal photon suppression and flow more closely resembling light flavor hadrons. It is unlikely that all thermal photons in a given event cease interaction at a single specific moment of time, but it is possible to estimate the average group behavior using this method.

Knowing when the "average" thermal photon stops interacting in the plasma will shed light on the information carried by the collective; specifically, it will provide context to the thermal photon inverse slope parameter which has been previously used in many experiments to estimate the QGP temperature, and will tell us approximately *when* the temperature is taken in the evolution of the plasma.

2. INCLUSIVE PHOTON RECONSTRUCTION

2.1 Quality Assurance

2.1.1 Data Sets

Our analysis objective has two parts: Obtain the direct photon nuclear suppression factor below $p_t = 4$ GeV/c and obtain the direct photon flow parameters. Note that while I covered a very high level overview of ALICE, LHC, and detector function in section 1.2, intimate machine specific details as well as a basic understanding of accelerator physics is assumed from this point onwards. Further machine specifics can be found in the physics performance reports published by the ALICE experiment [23, 24].

The first step for both of these objectives depends on direct photon isolation - which depends on the double ratio (see section 1.3.3).

$$R \equiv \frac{\gamma_{incl}}{\gamma_{decay}} = \frac{\frac{\gamma_{incl}}{\pi^0}_{data}}{\left[\frac{\gamma_{decay}}{\pi^0}\right]_{MC}} \tag{2.1}$$

It is immediately apparent that a highly accurate inclusive photon spectrum, γ_{incl}, is needed to proceed. That will be our first step.

The ALICE experiment (section 1.2) provides the tools needed to do this. At the time that this analysis was performed, the LHC had only collected substantial PbPb data at $\sqrt{s_{NN}} = 2.76$ TeV, so we must use that center of mass energy for our analysis. With this in mind, we require that data used in this experiment satisfy the following requirements:

1. LHC PbPb Data at $\sqrt{s_{NN}} = 2.76$ TeV.
2. ALICE global quality flag is “Good run”.
3. PHOS, TPC, and V0 detector flagged “On”.

4. PHOS and TPC reconstruction completed and marked “Good”.

5. V0 flagged “Nominal”.

It was found that data sets LHC 10h and LHC 11h data satisfied these conditions. LHC 11h data was selected because it had higher statistics, although LHC 10h data was frequently used as a cross check throughout this analysis. The data sets were found to be consistent within statistical error. On the recommendation of the ALICE Gamma working group, reconstruction pass 2 was selected.

Run numbers are available in appendix B.

2.1.2 Physics Selection

The ALICE experiment uses a sophisticated, multi-layer triggering called the High Level Trigger (HLT) to select relevant information to save to disc [47]. Each time the HLT is activated, information is read from the detectors to the disc and an “event” is recorded. Basic physics selection is required to differentiate different types of events in order to isolate events of interest (“physics” events) from uninteresting events (beam-gas interactions, beam-pipe interactions, cosmic rays, and so on).

Luckily, the ALICE collaboration provides its own computational framework that is built on top of the ROOT data analysis framework which has been the standby of particle physics for several years. This ALICE specialized framework is called AliROOT. Within AliROOT, a physics selection task is provided (perhaps uncreatively named: AliPhysicsSelectionTask.cxx) which was used in this analysis. Minimum bias triggers were used in both data and Monte Carlo in PbPb and pp events. For an exact characterization of the minimum bias triggers and their function, one may consult the literature [47].

2.1.3 Reconstruction

After physics selection and data storage, event level information is then reprocessed and re-characterized to make it easier to analyze. This "reconstruction" task is performed on a run by run basis by ALICE and will often consist of several passes - attempts to accurately reconstruct the data within some error tolerance. Computationally, this will consist of several steps such as tracing clusters in the TPC pads to form tracklets which are then merged into coherent TPC tracks, tracing those tracks to determine the event vertex, determining centrality using particle multiplicity and the Glauber Model, or finding the event plane using Fourier transforms on the data gather from V0A and V0C. It is beyond the scope of this work to discuss all of the observables computed during reconstruction, but more information can be found in a detailed review of ALICE reconstruction [60].

Of particular interest for our purposes is PHOS's clusterizer, which will be discussed briefly to provide context to the meaning of the word "cluster" which we will using extensively in later sections. As an electromagnetically interacting particle traverses the lead tungstate crystals of PHOS (also called cells), it pair produces (if a photon) and subsequently bremsstrahlungs in an electromagnetic cascade, depositing its energy in the cell as it disintegrates [61]. Since each cell is only half a shower length in width, several adjacent cells will be activated by the photon; with the center cells carrying significantly more of the total energy share than the outlying cells. This set of nearby activated cells is a cluster. By summing the energy of each cell in the cluster, the total energy of the incident original electromagnetically interacting particle can be computed. In addition, after weighting the energy recorded in each cluster, a geometric cluster center can be calculated which corresponds roughly to the impact point in the plane of PHOS. Knowing the impact point in relation to the heavy ion collision vertex allows one to compute the electromagnetic particle's four momentum unit vector and knowing its energy allows one to know its magnitude. By the simple relation: $\mathbf{p}_\gamma = E_r * \hat{\mathbf{p}}$ (where $E_r = \sqrt{m^2 + p^2}$ is the usual relativistic energy), we know the four momentum vector for the initial electromagnetic particle and can easily project it to obtain the particle's transverse momentum, p_t, which is more commonly used. All of this is performed during reconstruction [60].

It's worth mentioning that clusterizing is not always correct. For example, in a heavy ion collision the product particle multiplicity is sufficiently high that up to 40% of the PHOS electronics might be activated simultaneously by electromagnetic particles in the PHOS crystals [62]. In this case, it's entirely possible (and even likely) that multiple electromagnetic particles will happen to strike PHOS nearby enough that their electromagnetic cascades mix and the energy deposition distribution has multiple local maxima in the place of PHOS. In this case, it's necessary to "unfold" the merged clusters. Significant study has been devoted to unfolding techniques [63, 64] and these techniques are again performed by during reconstruction.

After reconstruction, the ALICE centrality task (AliCentralitySelectionTask.cxx) and PHOS tender (AliPHOSTenderTask.cxx) load the results of reconstruction and use them in the subsequent task. After physics selection, both of these tasks are applied to further refine the minimum bias data sample. Additional cuts will be applied to the minimum bias sample at the cluster level to mitigate possible errors in reconstruction (namely merged and exotic clusters - see section 2.3).

2.1.4 Additional Event Cuts

In addition to basic physics selection and reconstruction cuts, additional cuts were applied at the event level to ensure data quality. They are as follows:

1. Inclusive (0-100%) centrality
2. z-vertex < 10 cm
3. N Clusters > 2
4. $\left|\cos(\psi^{RP}_{V0A} - \psi^{RP}_{V0C})\right| > 0.7$

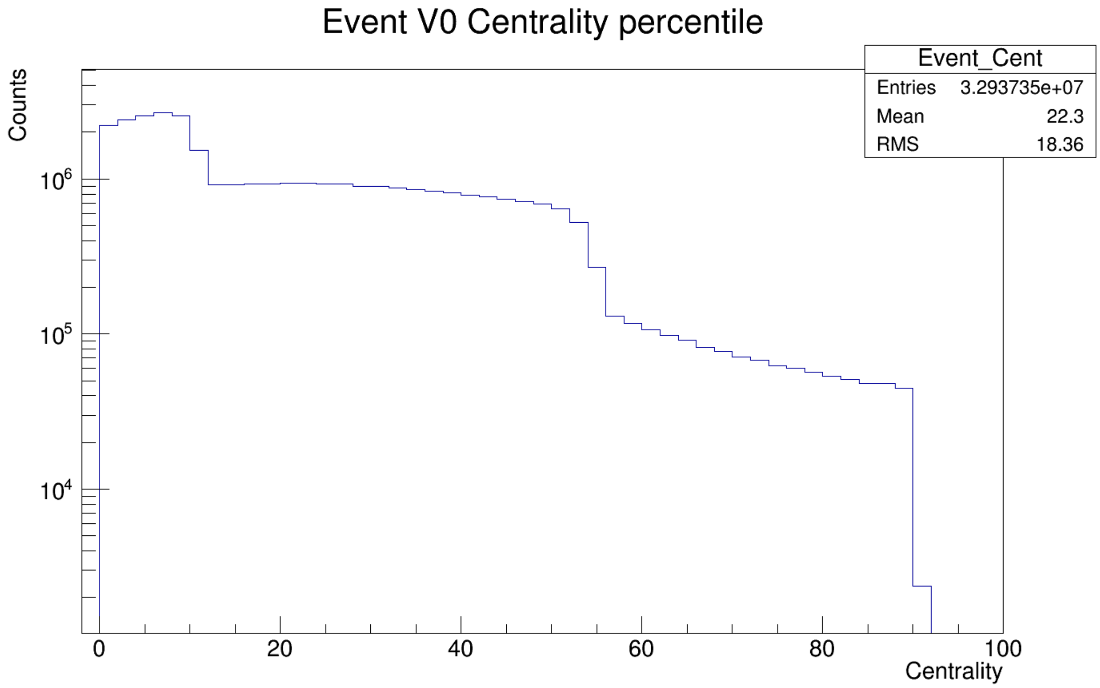

Figure 2.1. Centrality distribution of events after event cuts.

The low multiplicity of thermal photons with respect to background demands very high statistics to ensure a statistically significant signal. Unfortunately, the amount of reliably reconstructed Pb-Pb data generated by the LHC at 2.76 TeV is somewhat limited. Thermal photon flow especially is a concern, since at high order and at high p_t might only have a handful of statistically significant thermal photons needed to make a measurement. All appropriate available Pb-Pb data will be used, which amounts to approximately 32.9 million events after event cuts (see section 2.1.1), but even with the maximum amount of statistics, efficiency must be as high as possible in part to mitigate limited statistics in pp at 2.76 TeV which will be especially important in the computation of the thermal photon suppression. To guarantee this, no centrality binning at the event level was introduced; the centrality of all future plots will be minimum bias unless explicitly stated otherwise. See Fig. 2.1.

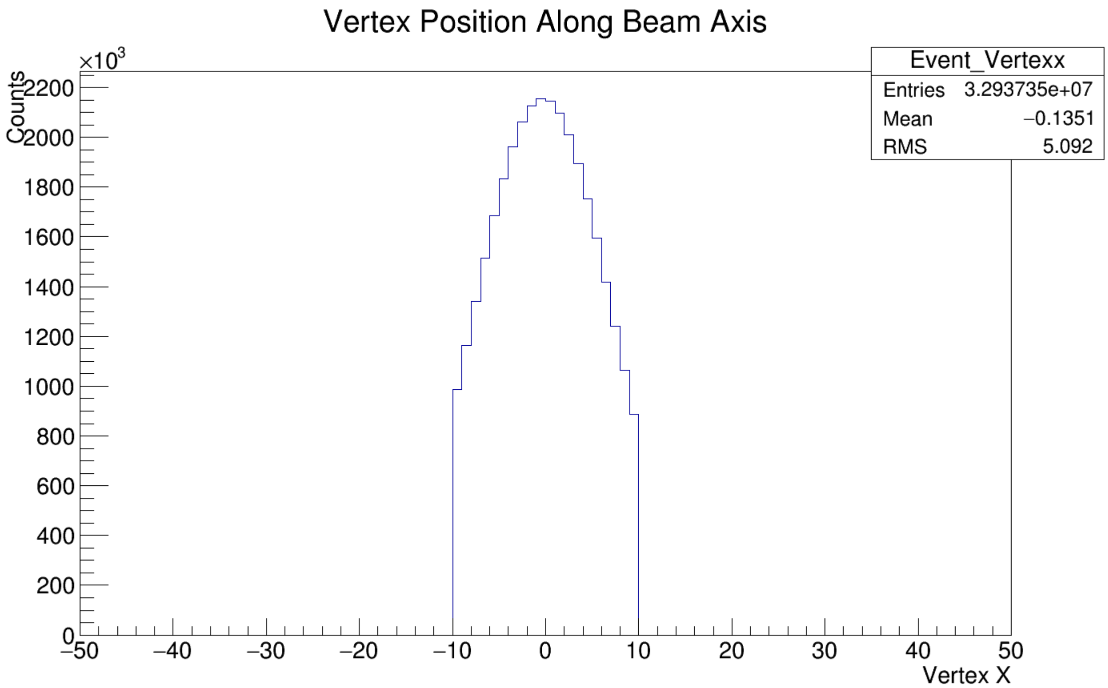

Figure 2.2. Z-coordinate displacement of event event vertex with respect to the origin in the ALICE coordinate system.

A cut on the vertex z-coordinate (the coordinate along the beam line in ALICE's global coordinate system) of ± 10 cm was also introduced. In cases of very large z-vertex, particle showers in the photon spectrometer might not be normal to the PHOS plane, which could cause an increased number of exotic clusters in the clusterizer (see section 2.3.1). The z-vertex cut is loose, but will help to prevent this. See Fig. 2.2.

Although they should be removed by physics selection, ultra peripheral PbPb events and pp events might only yield a handful of calorimeter clusters. In these cases, there is not enough statistics to adequately reconstruct the event plane. Therefore, at least 2 clusters are required in the calorimeter. See Fig. 2.3.

In order to ensure consistency in the V0A and V0C derived event planes (See section 5.1.2), the scalar product of the planes (or, more specifically $\left|\cos(\theta^A_{EP} - \theta^C_{EP})\right|$) was also computed and can be seen in Fig. 2.4. This provides a good check to see how the A and C side event planes agree (if at all). A global cut on events

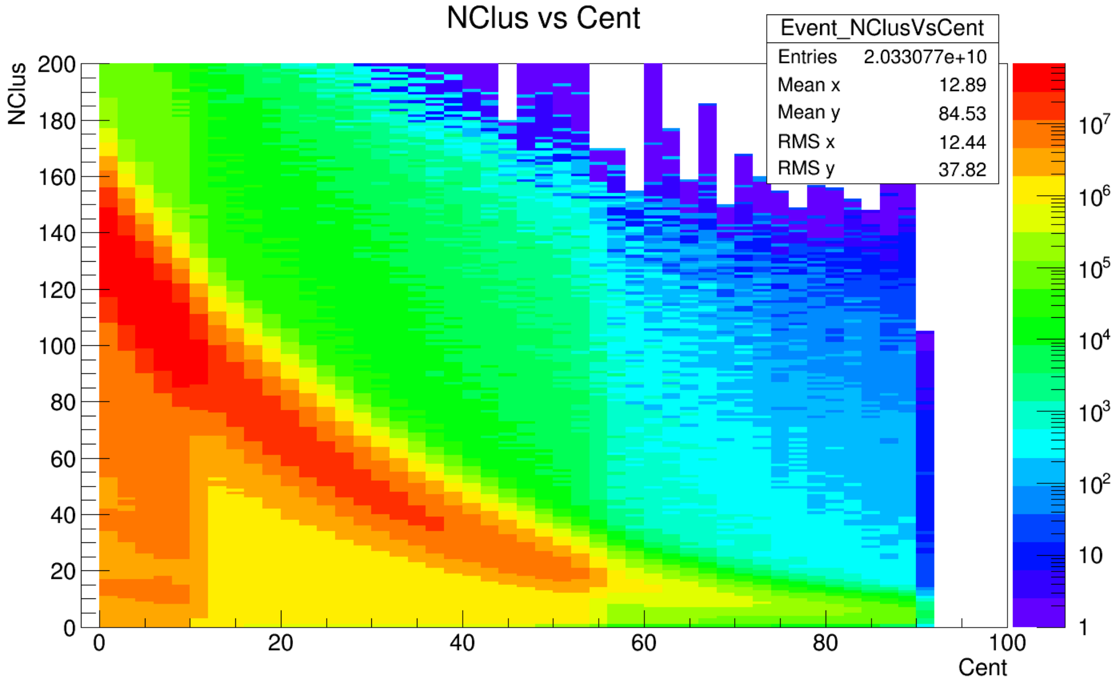

Figure 2.3. Number of clusters per event with respect to centrality.

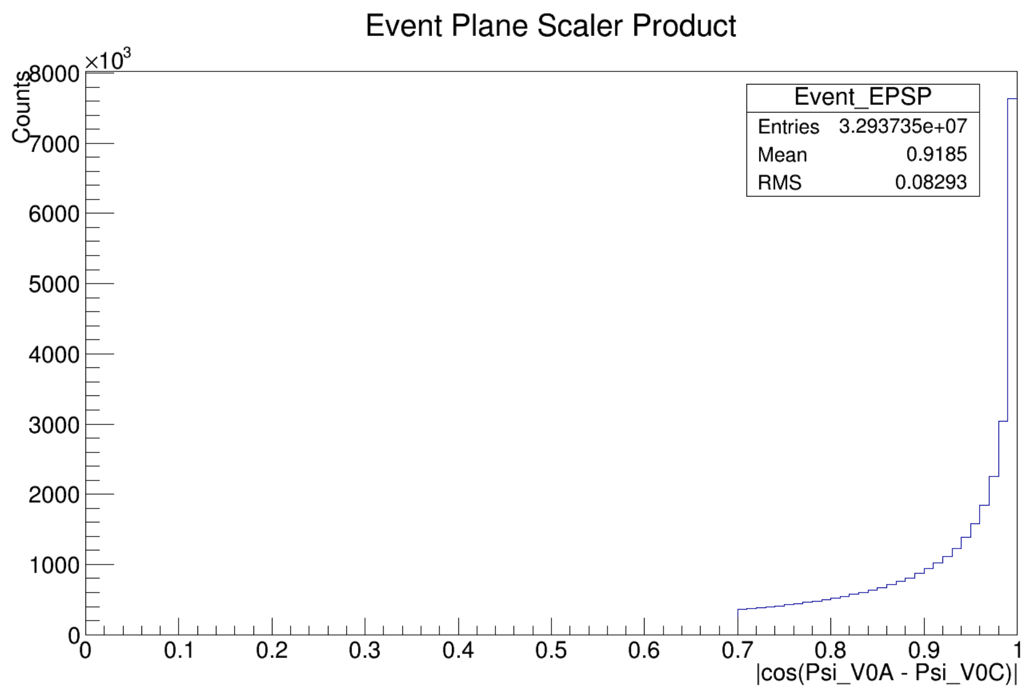

Figure 2.4. Event plane scalar product ($\left|\cos(\psi^{RP}_{V0A} - \psi^{RP}_{V0C})\right|$) to compare V0A and V0C side agreement.

with $\left|\cos(\theta^{A}_{EP} - \theta^{C}_{EP})\right| < 0.7$ was applied to eliminate possible bias from inconsistent reporting of the event plane.

An estimate of the efficiency of each cut is available in Fig. 2.15.

2.1.5 Elementary Cluster Cuts

At the cluster level, there are the following quality assurance cuts:

- cluster->Is PHOS cluster

1. N Cells > 3
2. Cluster Energy > 0.3 GeV
3. $-200 \leq TOF \leq 200$ ns

4. $d_{NearestBadChannel} \geq 2.2$ cm

All clusters considered were those in the Photon Spectrometer (PHOS) only. A closely related detector, the Electromagnetic Calorimeter (EMCAL), also produces electromagnetic cascades which could be used to study electromagnetically interacting particles (including photons!) [65]. However, the EMCAL has only recently been optimized to study photons, and the techniques are still being tuned for that detector [66]. As such, it was decided to exclude EMCAL clusters from this study.

The first cut on PHOS clusters requires at least three activated lead tungstate cells in the cluster. This is by far the lowest efficiency cut (See Fig. 2.15). Its primary purpose is to eliminate contribution from so called "hot cells"; that is, PHOS crystal cells which are miscalibrated and greatly over report energy deposition magnitude and frequency. While the "Bad Map" in the tender (section 2.1.3) should effectively record and remove hot cells, the PHOS electronics are continuously exposed to high levels of synchrotron radiation as well as radiation from the collisions themselves [67]. It is inevitable that radiation damage will continuously change the properties of the electronics for each cell. Therefore, for any given, it's possible for the bias voltage to be improperly reported in tender and for a cell to become hot. The cell number and energy cuts will provide a redundant layer of protection from this class of cluster contamination.

We therefore require that at least three cells must be present in the identified cluster to qualify for this study. Since the radiation length of each cell transverse to the normal vector is $0.5X_0$ (see section 1.2.3), this cut is extremely unlikely to eliminate actual photon showers. See Fig. 2.5 for the distribution of activated cells per cluster.

It is also required that the total energy of the cluster exceed 0.3 GeV. Similar to the above activated cell number cut, this cut is also intended to remove hot or dead cells. See Fig. 2.5 for the distribution of energy in each cell.

The time of flight (TOF) for the cluster is the time difference between the High Level Trigger activation and the activation of the cluster as measured by the LHC

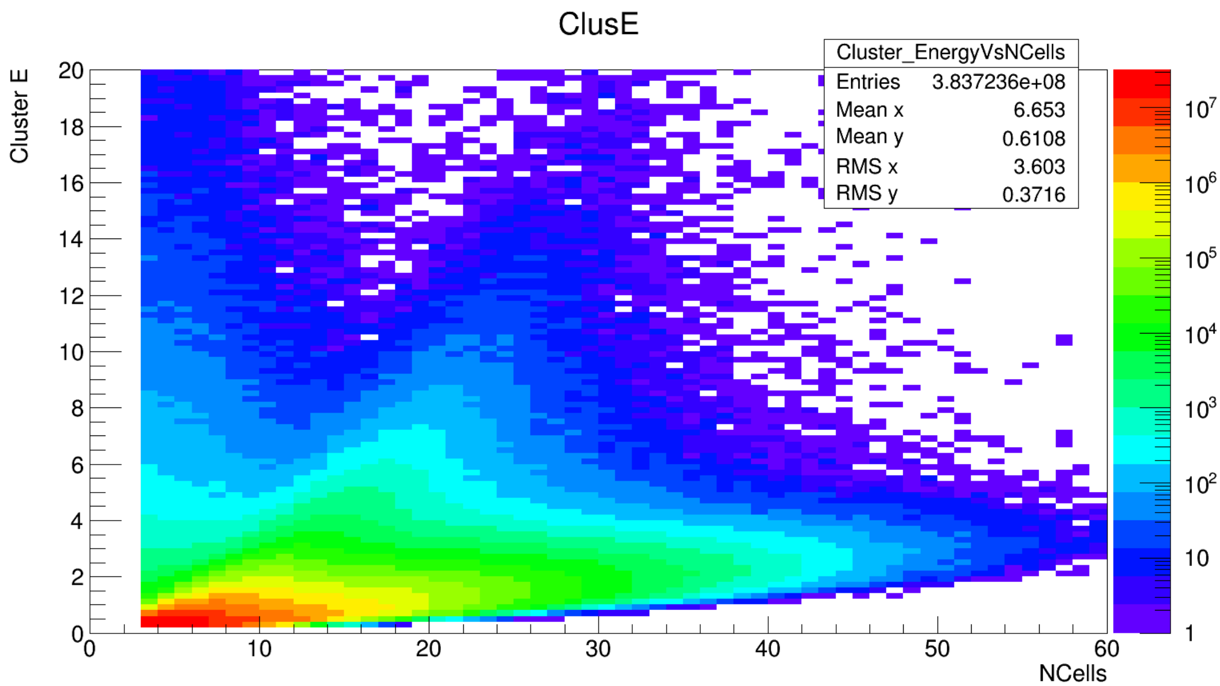

Figure 2.5. Energy of each cluster versus the number of cells in that cluster.

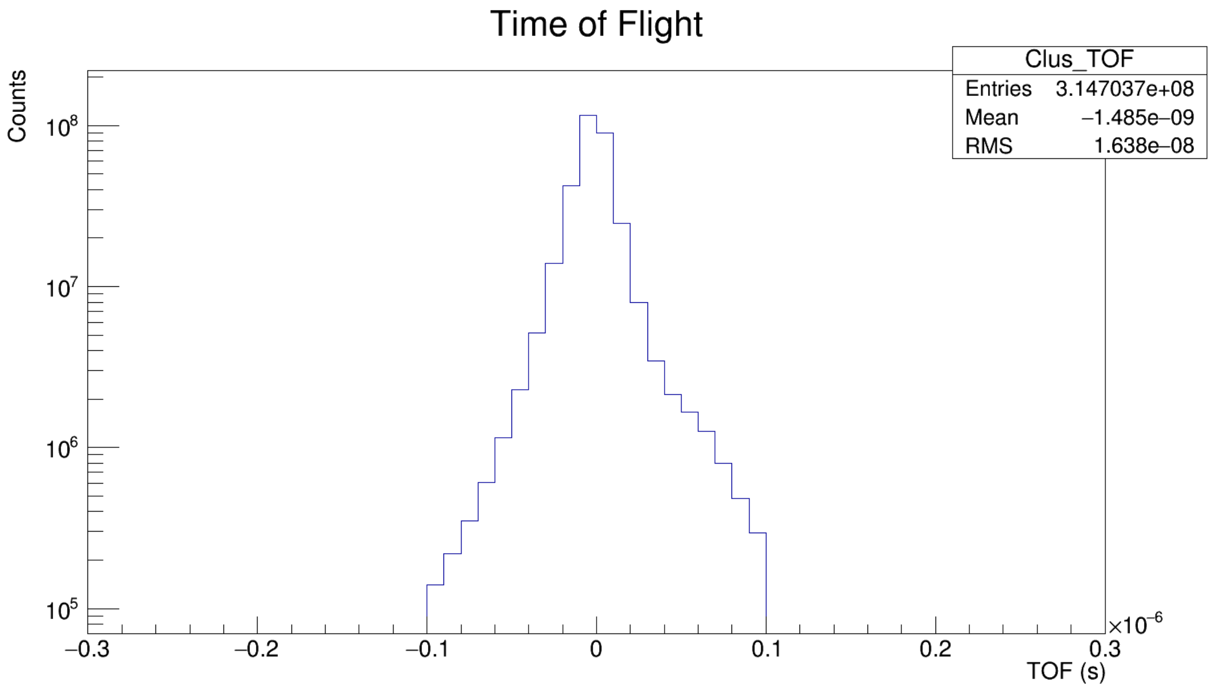

Figure 2.6. Time of Flight of each cluster.

clock [68]. It is required that the time of flight not exceed 200 ns before or after the collision. The distribution of TOFs is shown in Fig. 2.6. Note that the actual time of flight of a product particle in the lab frame is one the order of $\frac{4.6m}{\sim c} = 15ns$. Since this is much less than the measured TOF, the distribution can be thought of as representing the uncertainty in the LHC clock, which is locked to the bunch crossing rate [68]. The cut is applied to reduce the chance of possible pileup; that is, triggering miscalibration such that residual shower energy from one event contributed a false cluster to the next collision event. Great effort is made in CERN to ensure accuracy of the LHC clock [69], and in practice pileup is quite rare [60]. Nonetheless, the time interval between bunch crossings (and thus possible events) is roughly $\Delta T \sim \frac{1}{2c}$ in the lab frame; with a time interval this small, it is worthwhile to provide a redundant layer of protection.

A cut was also applied to remove clusters on the edges of the detector or on the edge of cells marked as bad in Tender. Clusters which contain cells on the edge of the detector can misrepresent the energy or momentum of the particle which caused them. If the lead particle of a shower is within the acceptance, but a part of its shower falls outside of PHOS or in a region which for whatever reason is excluded from analysis, then the energy lost in the missing part of the shower is not taken into account when computing cluster energy. This will introduce a bias to artificially lower the observed energy of clusters. To combat this, it is required that the cluster's center (see section 2.1.3 for a formal definition of cluster center) be more than 2.2 cm (the diagonal length across one cell) from an excluded region. That is to say that while cells whose center is within 2.2 cm of an excluded region are included in the analysis, no accepted cluster may have a center in such a cell. As a result, any energy leaked must be at least one cell from the cluster center. Fig. 2.7 shows the distance of each cluster center of mass to the edge of the detector or nearest bad cell. Fig. 2.8 shows the net distribution of cluster centers in each module both before and after cuts. Note that this is the effective acceptance. Besides cut 1, this is the least efficient cut, as can be seen in Fig. 2.15. However, the reduction in systematic bias was judged to be worth the cost.

2.2 Charged Particle Veto

2.2.1 Track Matching

Since electromagnetic cascades in PHOS can be triggered by any electromagnetically coupling particles - and not just gammas [60] - any photonic analysis with PHOS will require rejection of clusters originating from charged particles. This rejection is the charged particle veto (CPV). However, while it's true that a calorimeter cluster originating from a gamma is not able to be differentiated from a cluster due to a charged particle using PHOS alone, a comprehensive CPV can be used to reject these charged particles using a variety of methods.

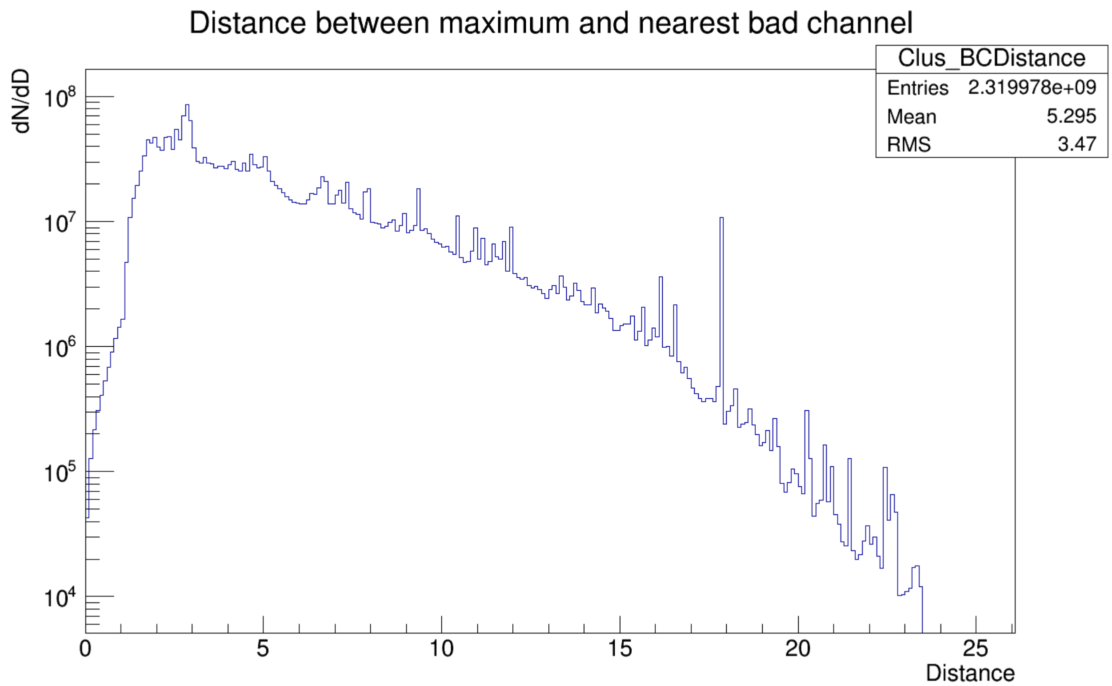

Figure 2.7. Distance to nearest bad channel.

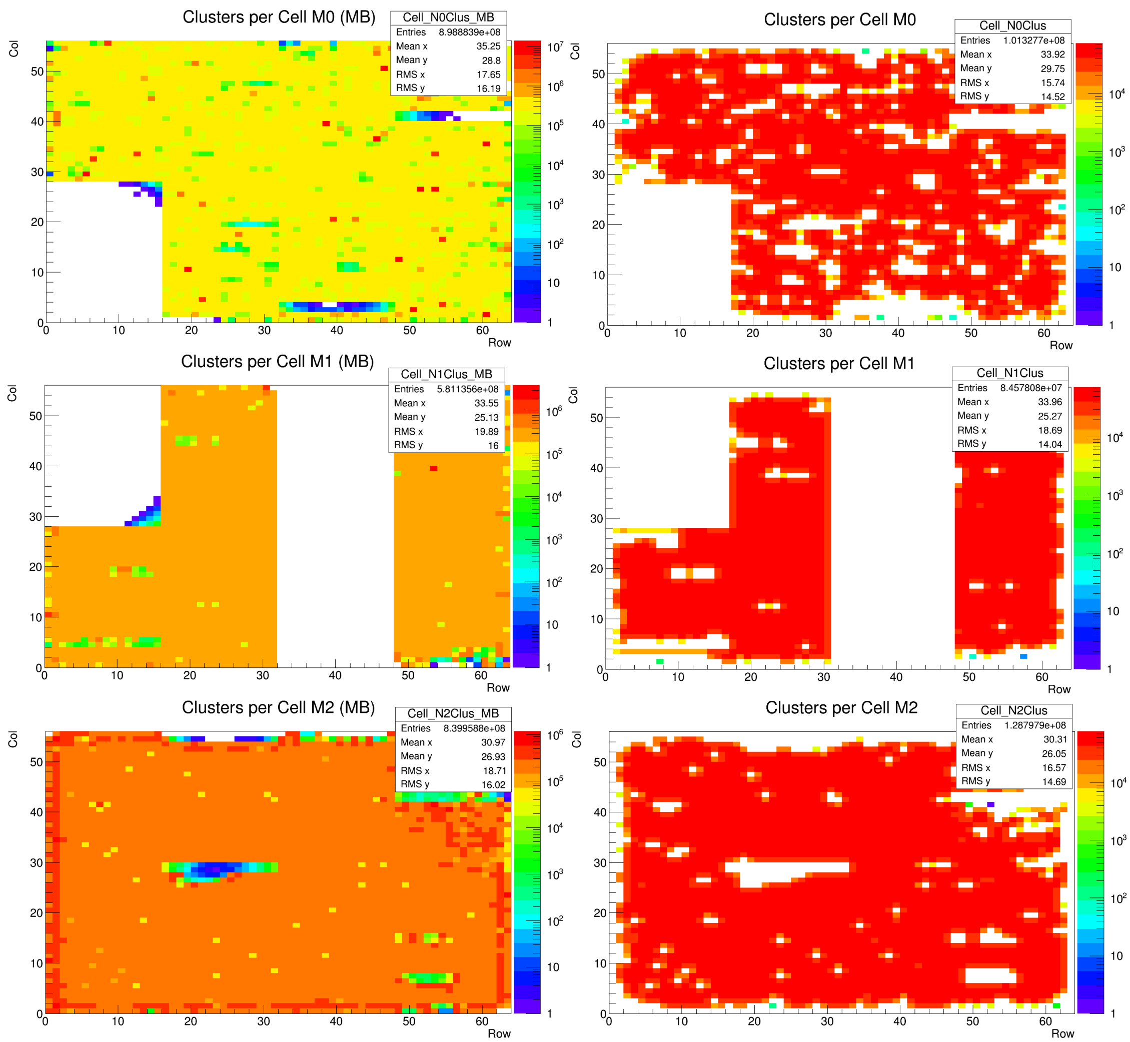

Figure 2.8. Cluster centers in module 0 (top), 1 (middle), and 2 (bottom) before and after cluster cuts.

For example, it is sometimes possible to compare qualitative aspects of a cluster such as shower shape and energy distribution in order to make a (sometimes quite reliable) source particle identification (particle ID, or PID) [70]. This is largely due to PHOS being inside ALICE's central magnet, meaning a lead charged particle which cascades as it traverses the lead tungstate crystal will follow a bending path as it deposits energy. After reconstruction, this bended path projects in two dimensions as an elliptical shape. For more information on this phenomenon, see Section 2.3. In general, however, better efficiency can be achieved by using additional information obtained using other detectors present in ALICE which specialize in the identification of charged particles.

ALICE's TPC is best suited this role because of its well understood particle ID [71, 72], and location both close to the beam line. It also covers the same azimuthal acceptance as PHOS. The TPC particle ID is well studied and systematic uncertainty due to TPC misidentification can be estimated and is considered sufficiently small [71]. In addition, during reconstruction tracks in the TPC are propagated onto the plane of PHOS [60] (see section 2.1.3 for a discussion of reconstruction), allowing many tracks to be selected as possible matched track candidates. The challenge when creating this analysis is to select which likely matched track (if any) could be used as justification for a CPV of that cluster. Several methods were explored to do exactly this and are explained briefly in each subsection.

2.2.2 Charged Particle Trajectory Extrapolation (Analytic)

Initially, an analytic method was pursued to compute the distance of closest approach (DCA) between the extrapolated matched track trajectory and an arbitrary point in space. If a cluster's center could be compared to the expected trajectory of a nearby track using this DCA, then it could be possible to cut on it to remove charged particles. For this problem, a psuedo-classical approximation of the charged particle trajectory was assumed. Since the ESD files record the final state momentum, position, charge, and mass of a track in the TPC using in the class AliExternalTrack-Param: public AliVTrack, it is in principal possible to compute a parameterization of particle trajectory, $\overrightarrow{x}(t)$. The distance of closest approach to an arbitrary point in space is therefore when

$$\frac{\delta}{\delta t}\left\|\overrightarrow{x}(t)-\overrightarrow{x_0}\right\|=0;\frac{\delta^2}{\delta t^2}\left\|\overrightarrow{x}(t)-\overrightarrow{x_0}\right\|>0 \tag{2.2}$$

If the arbitrary point in space is taken to be the deposited energy center-of-mass of the cluster and the point $\overrightarrow{x}(t=0)$ is taken to be the track's outer parameters (via AliESDtrack::GetOuterParam), then all the information needed to compute the trajectory is known. Finding the form of the equation of motion directly from the Classical Hamiltonian and the Lorentz force turns out to be tricky, but, by the uniqueness theorem, we can take the form of the equation of motion to be that of a generalized helix. Knowing this and $\overrightarrow{x}(t=0)$ gives

$$\overrightarrow{x}(t)=R[[\cos(\omega t)-cos(\theta_0)-x_{i0}/R]\hat{i}+[\sin(\omega t)-cos(\theta_0)-x_{j0}/R]\hat{j}+[\frac{p_{z0}t}{mR}-x_{k0}/R]\hat{k}] \tag{2.3}$$

where R is the radius of the helix, omega is the Larmer frequency, and $\theta_0 = \arctan(\frac{p_{y0}}{p_{x0}})$. We can then compute the minimum,

$$\frac{\delta}{\delta t}|\overrightarrow{x}(t)-\overrightarrow{x_c}|^2=0=\left(\frac{\overrightarrow{p}}{qB}\right)^2\left[\left(\frac{2p_z qB}{m|\overrightarrow{p}|^2}\right)\left(x_z-x_{cz}+\frac{p_z}{m}t\right)-\left(\cos(\arctan(\frac{p_y}{p_x}))-\frac{x_x-x_{cx}}{|\overrightarrow{p}|^2}qB\right)\left(\frac{qB}{m}\right)\left(\sin(\frac{qB}{2m}t)\right)+\left(\sin(\arctan(\frac{p_y}{p_x})-\frac{x_y-x_{cy}}{|\overrightarrow{p}|^2}qB\right)\left(\frac{qB}{m}\right)\left(\cos(\frac{qB}{2m}t)\right)\right] \tag{2.4}$$

The resulting transcendental equation can be solved only through numerical methods. Therefore, it was decided to pursue an entirely numerical approach from the beginning.

2.2.3 The Statistical Method (Numerical)

Although extrapolating charged particle trajectories to matched tracks is analytically difficult, previous analysis [29] have used a statistical method to perform CPV. In this method, after the charged particle leaves the TPC, its trajectory disperses in a two dimensional factor density distribution centered on the end of the track. This

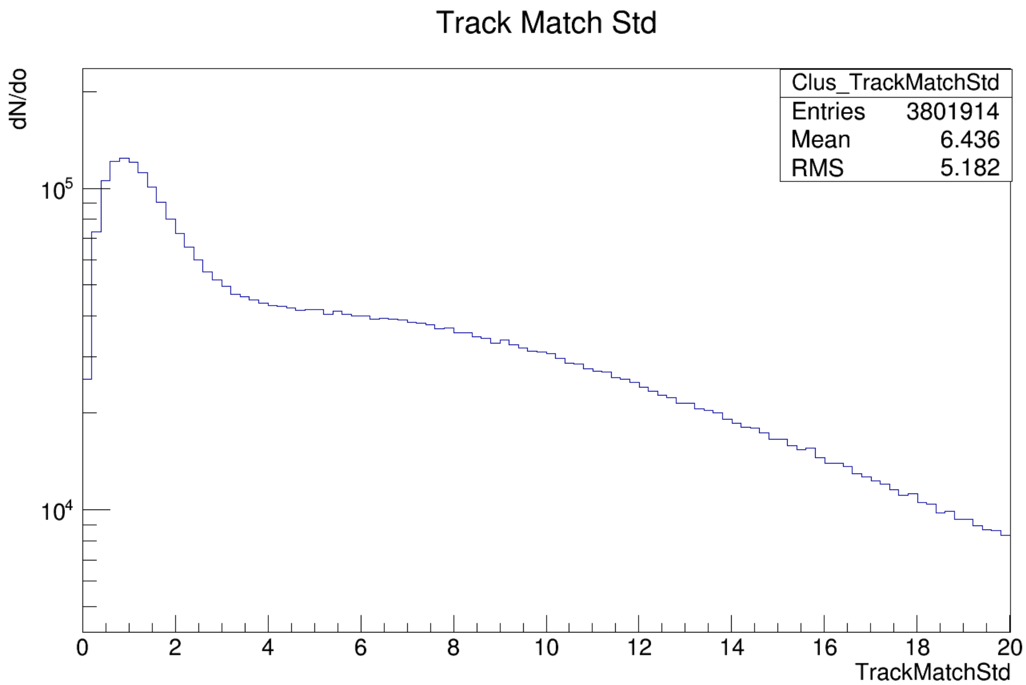

Figure 2.9. Statistical Method track match standard deviations compared to cluster count.

factor density distribution has been tuned using simulation and detector performance data to maximize a factor, r, when the track and cluster in fact belong to the same source particle . This factor function and its results can be seen in Fig. 2.9.

The results are bimodal; the results in the first mound corresponding to unrelated tracks and cluster and the second mound to matched tracks and clusters. There is some overlap. Because of this, any cut which is used will have both Type I and Type II error. Type I error is a false positive and will reduce sample purity, while Type II error will is a false negative and will reduce sample efficiency unnecessarily. A cut of 3.5σ was used. See section 2.4 for the influence on this cut in both sample purity and efficiency.

2.3 Cluster Shape Analysis

2.3.1 Exotic Clusters

After basic QA, some non photonic clusters may continue to persist. So called "exotic clusters" are a catch-all term for relatively rare cell energy deposition patterns that qualify as clusters and pass QA and CPV cuts, but are not caused by photons or neutrons. Possibility sources of these rare cluster include, but are not limited to: cosmic rays, reemission from detector structural elements, improperly identified merged clusters, or other complex or unknown phenomenological sources. Whatever the cause, these sources can be differentiated from photonic clusters due to their irregular shape. A very brief discussion of each element in this (incomplete) list of possible exotic sources and their properties follows.

Consider the case of cosmic rays, which have been well studied [75]. ALICE physics selection and QA cuts (see section 2.1) remove most cosmic ray contamination. For that which remains, incident cosmic radiation will almost certainly not come from the interaction vertex. As such, the geometry of the photon spectrometer is not optimized to observe them and the result will be a very abnormal distribution of energy within the cluster (see Fig. 2.10 for illustration). By contrast, an actual photon source from the interaction vertex will have a very predictable energy deposition pattern (that is, just a Gaussian). Therefore a core energy analysis (see section 2.3.4 and 2.3.3) should be very capable to detecting this abnormality.

Reemission from structural elements is also studied [23, 24]. Like cosmic rays, these exotic clusters will almost certainly not originate in the interaction vertex. As such, a core energy analysis should once again be used.

Although the clusterizer (discussed in section 2.1.3) attempts to "unfold" merged clusters. Some misidentified clusters can remain. These merged clusters are expected to have multiple energy deposition maxima (See Fig. 2.11). They too can be removed with a simple core analysis cut.

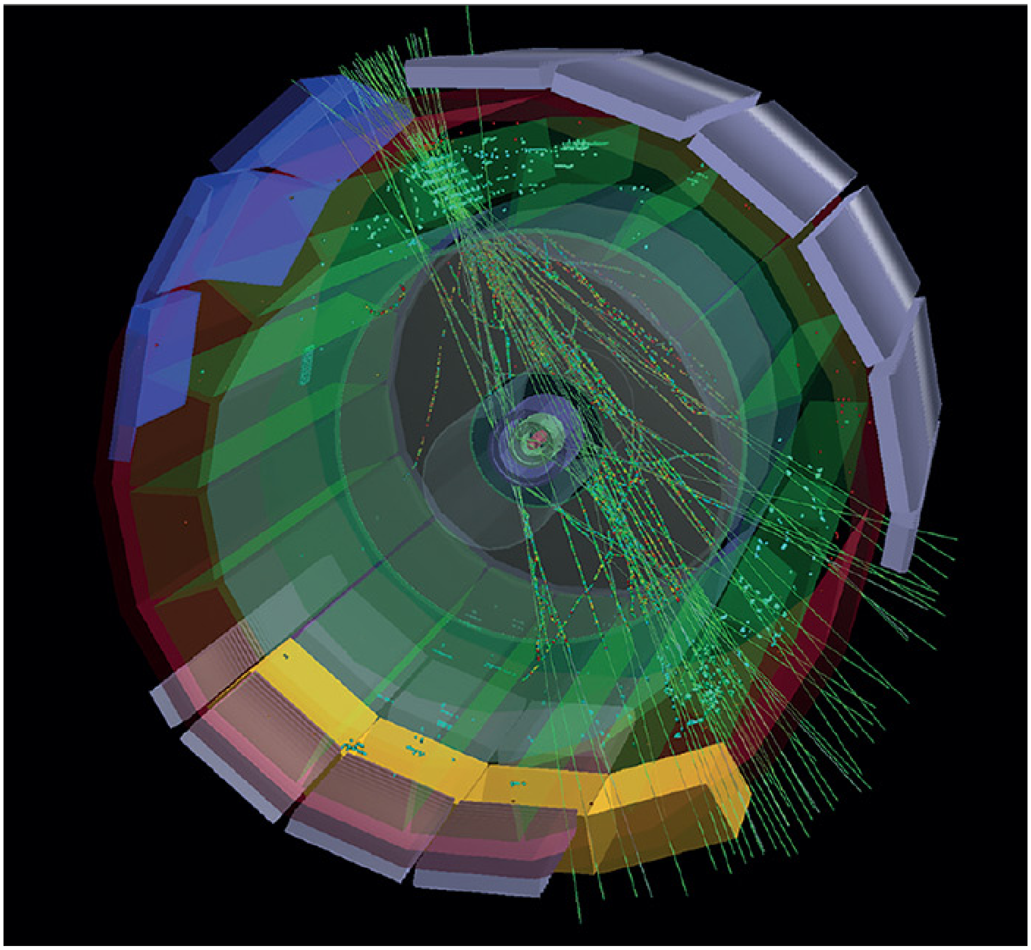

Figure 2.10. Cosmic Ray illustration. In this case, the diagram shows a high energy cosmic muon developing a particle show within the TRD and TPC volumes. [56]

2.3.2 Baryonic Contamination

Besides exotic clusters, it's also possible for neutral hadrons to create "legitimate" electromagnetic cascades in the photon spectrometer. Although it may be counter intuitive, neutrons in particular create electromagnetic cascades which may be mistaken for photons [76]. The reason is that free neutrons liberated from the original nuclear matter or from subsequent fragmentation before chemical freeze out are moving fast enough in the lab frame that - with a boost due to time dilation - their characteristic decay timescale is just long enough to make it to the surface of the photon spectrometer. Although the neutrons themselves are non interacting in PHOS, if they decay via their primary decay channel (simply beta decay, $\frac{\Gamma^{n \to p + e^- + \nu^e}}{\Gamma^{tot}} = 99.7\%$ [77]) while traversing the crystal, then the electron-proton pair certainly *will* create a shower. Since the shower will not match any track found in the TPC and is a real cluster (thus passing most QA cuts), it will be flagged as a photon candidate by the analysis. Therefore, further cuts are required to remove this possible source of baryonic contamination.

Luckily the cluster created by the neutron decay product shower is qualitatively different from one crated by an actual photon. This difference shows itself in two primary ways. Firstly, the shower will be significantly wider and more diffuse. This is because the decay products will have a larger opening angle from their decay vertex in addition to the fact that rest mass of the neutron will contribute nontrivially to the shower energy. The second qualitative difference is that the shape of the deposited energy in the cluster will be somewhat elliptical because the neutron shower is effectively a hadron shower overlapping with and electron shower. Since the photon spectrometer is inside the primary magnet in ALICE, the lead particles will bend in opposite directions as they traverse the calorimeter. As the lead particles migrate away from each other and deposit energy as they go, the two overlapping showers will tend to create something like an ellipse in the two dimensional energy deposition matrix. The eccentricity of this ellipse is determined by the transverse momentum of

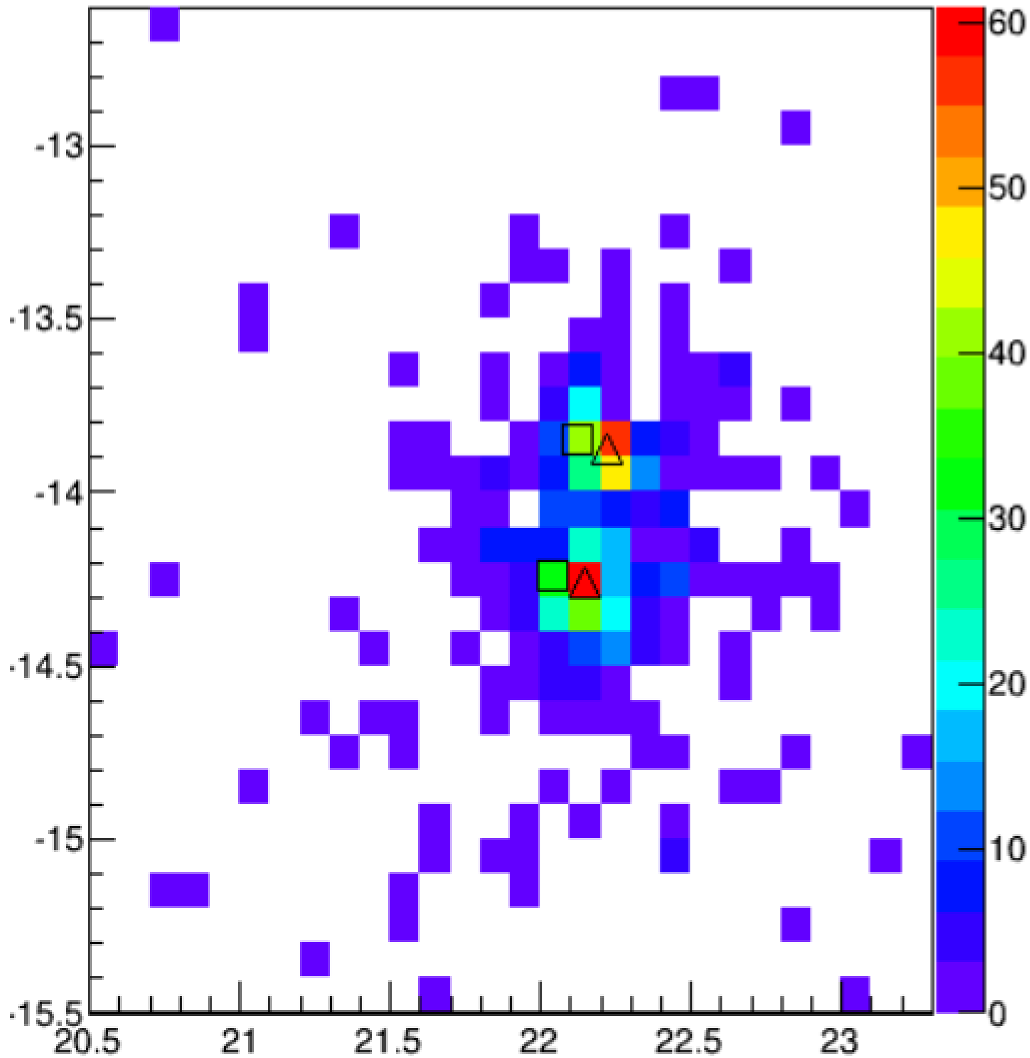

Figure 2.11. Merged clusters illustration.

the decaying neutron as well as when within the spectrometer the neutron decides to decay. A very late decay, for example, might be very faint and circular.

While studying this phenomenon is not our focus in this analysis, knowledge of its existence allows us to create cuts to eliminate this possible source of bias. To eliminate these free neutrons from our data set, an analysis of the cluster dispersion matrix is performed.

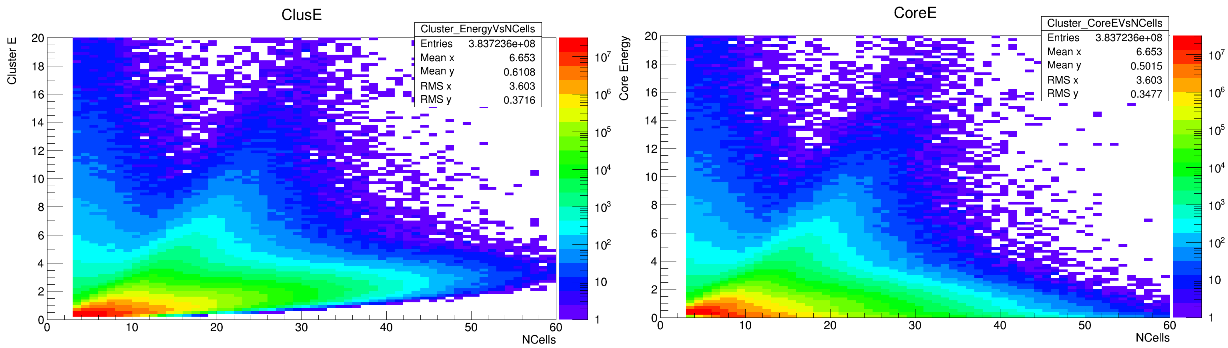

Figure 2.12. Total cluster energy vs cell number (right) and core cluster energy vs cell number (left).

2.3.3 The Core Energy Ratio Method

The first method shower shape analysis designed to eliminate contribution from so called "exotic clusters" uses the cell amplitude - the energy deposited by a cluster in a cell - to look for a clear global maximum. The global maximum then has a circle of radius R_{core} defined around it. Since the detector consists of individual rectangular cells with a side length of 2 cm and no further fine structure, the cell location is defined to be the location of the center of the cell in the detector coordinate system. This results in a discrete distribution of unique R_{core}. The integrated energy inside the circle is computed to be the E_{core}. One may then cut on the ratio $\frac{E_{core}}{E_{cluster}}$. If there are multiple large local energy maxima as one might expect in the case of multiple overlapping clusters, this ratio will be small and the overlapping clusters may be separated using a so called unfolding algorithm or simply removed entirely. Note that in the special case for $2 < R_{core} < 2\sqrt{2}$, the circle is exactly the cell with the amplitude maximum and its immediate neighbors in a cross formation. This is exactly the "cross cut" suggested and used by the CMS collaboration for similar cluster dispersion analysis [73].

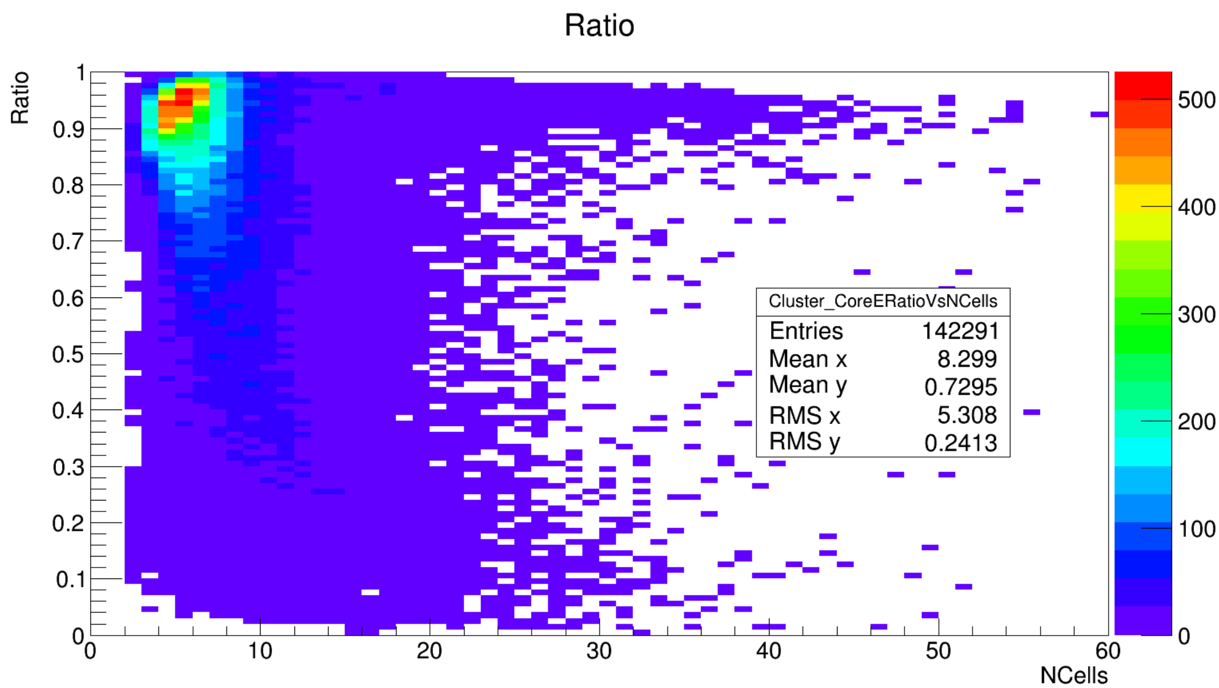

Figure 2.13. $E_{core}/E_{cluster}$. The ratio may be shifted up or down depending on the choice of R_{core}. A clear relation can be seen between the number of activated cells versus the ratio. Clusters with many activated cells, but a low core energy ratio are likely overlapping showers.

2.3.4 The Dispersion Matrix Method

A second shower shape analysis designed primarily to remove contamination from neutral mesons weights each activated cell in a cluster by a logarithmic weighting function of the cells energy to the minimum threshold energy of the cell,

$$w_i = max[0, p + log(e_i/E)] \tag{2.5}$$

This weight is then used to compute a dispersion matrix using the formula,

$$s_{x_i x_k} = \left\langle (x_i - \bar{x_i})(x_k - \bar{x_k}) \right\rangle = \frac{\sum w_i x_i x_k}{\sum w_i} - \frac{\sum w_i x_i * \sum w_k w_i}{(\sum w_i)^2} \tag{2.6}$$

where x and z are the coordinates of position in the plane of the detector and the sums are over all activated cells in the cluster [76]. The matrix is diagonalized and rotated to its major axis and the eigenvalues λ_0 and λ_1 are found. Since isolated photon clusters should be mostly circular, it follows that the dispersion matrix eigenvalues should be degenerate. This method is substantially more complicated and indeed, the exact weighting constants used will vary on a run by run basis - whenever the minimum threshold energy for a cell is recalibrated. However, it also has several advantages. For example, not only will the dispersion matrix shape cut overlapping cells, it also serves as a redundant charged particle veto since leptons and hadron showers will bend in the magnetic field as they traverse the detector, creating an elliptical shower shape.

2.4 Efficiency, Purity, and Inclusive Photon Invariant Yield

2.4.1 Efficiency

If one sums up all the cuts mentioned in the previous sections, eight cluster level cuts were applied to obtain the inclusive photon spectrum:

0. Is PHOS = True

1. $N_{cells} \geq 3$

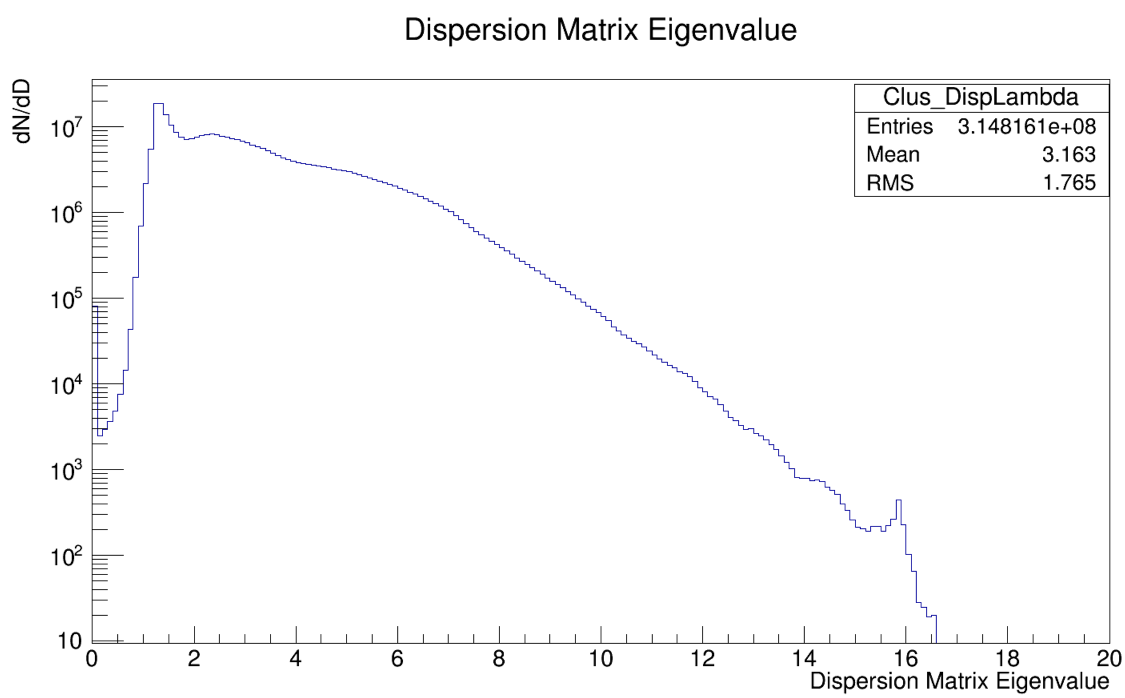

Figure 2.14. Dispersion matrix eigenvalue of each cluster.

2. $E_{cluster} \geq 0.3$ GeV

3. $-100 \leq TOF \leq 100$ ns

4. $d_{NearestBadChannel} \geq 2.2$ cm

5. CPV (see 2.2)

6. Cluster Shape (see 2.3)

Where any clusters that survive cut 0 are minimum bias clusters, any clusters that survive cuts 0, 1, and 2 are weakly cut clusters, and any clusters that survive all cuts are photon candidates, n_{incl}. We will simply call these "inclusive photons" for brevity; although it's important to note that these clusters may be caused by the occasional charged particle or hadron or exotic cluster which somehow slipped through the cracks. To see an analysis of this possibility, see section 2.4.2. Although each cut has already been explained in previous sections, one can see the relative strengths of each cut by viewing Fig. 2.15.

One can immediately see that the (relatively) strongest cuts are on weak cut clusters. This is expected: a small number of hot cells are expected to contribute a consistently large amount of false signals with very high energy, but small cell number. The charged particle veto again has low efficiency primarily because there is significant overlap in the charged and neutral particle Gaussians seen in Fig. 2.9. A hard cut was thus chosen in order to ensure the highest possible purity with the statistical method.

The overall analysis efficiency (often just "efficiency") in each p_t bin was obtained by the ratio: $\epsilon = [\frac{n_{incl}}{n_{MB}}]_{MC}$ and is shown in Fig. 2.16.

2.4.2 Purity

If the analysis efficiency discussed in the previous section is understood as the fraction of the minimum bias clusters which survive all cuts, $\epsilon = \frac{n_{incl}}{n_{MB}}$, then the

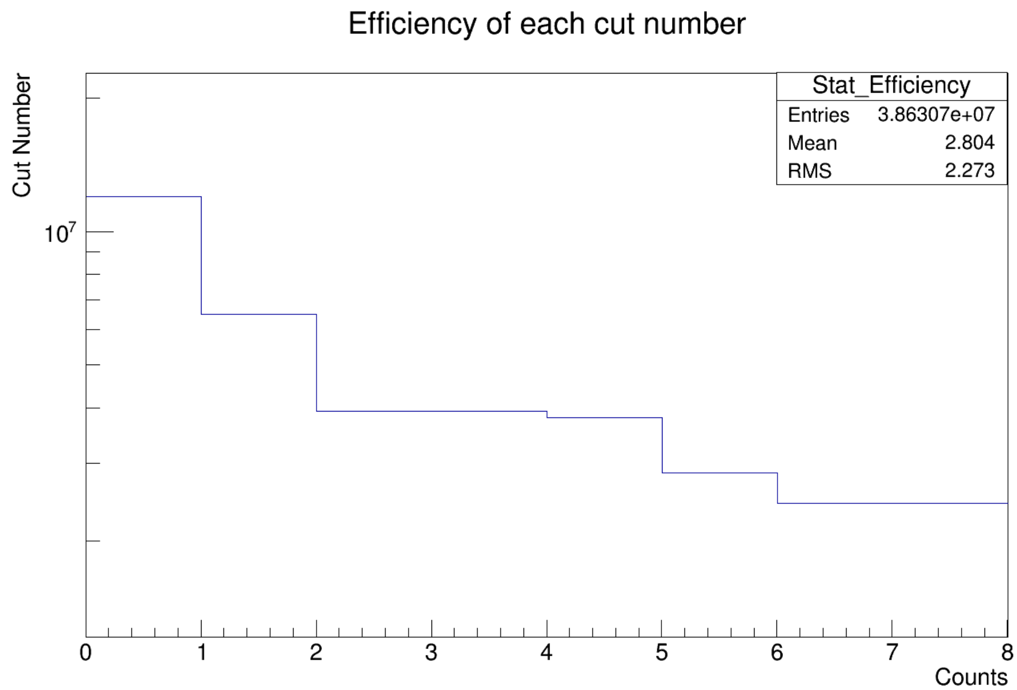

Figure 2.15. Surviving clusters as a function of cut number. Each cut is progressive; for example, the number of clusters in column 4 have survived cut 0, 1, 2, 3, and 4.

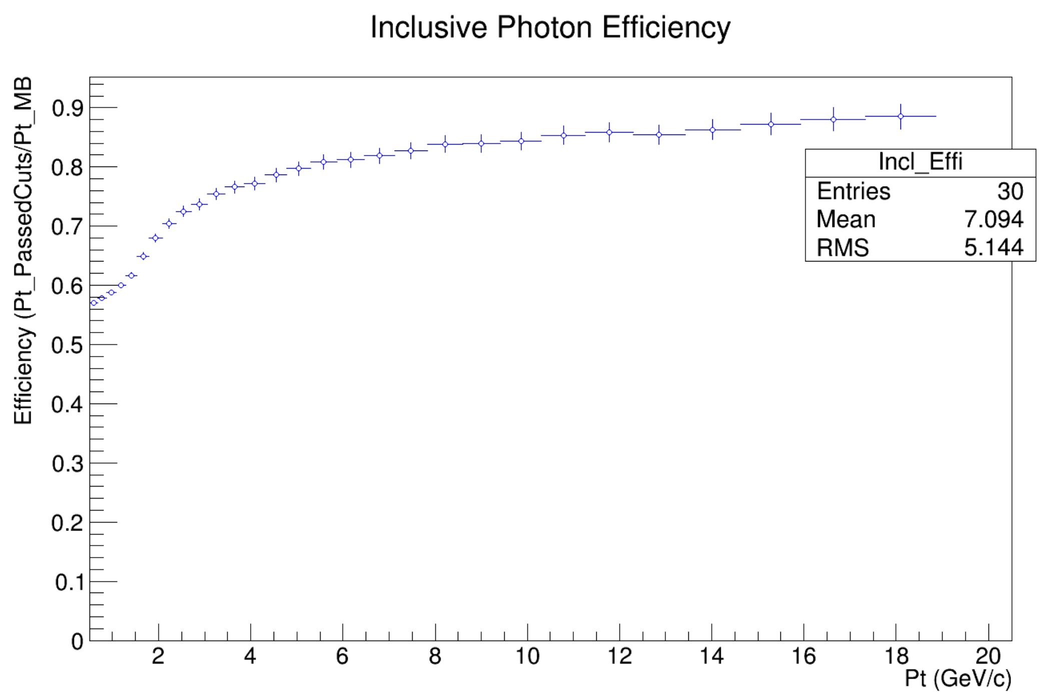

Figure 2.16. Inclusive photon cut efficiency in each p_t bin. Efficiency is computed by $\epsilon_{MC} = [\frac{n_{incl}}{n_{MB}}]_{MC}$, which may differ from the result in real data, $\epsilon_{Data} = [\frac{n_{incl}}{n_{MB}}]_{Data}$ due to the contribution of hot cells. (Monte Carlo does not simulate hot cells.)

identification purity is the fraction of those surviving clusters which are in fact caused by a photon, $\mathcal{P} = \frac{|n_{real} \cap n_{incl}|_{MC}}{|n_{incl}|_{MC}}$. Where n_{incl} is the surviving clusters, and n_{real} is actual number of photons incident on the detector. It is generally not possible to directly measure the purity, because n_{real} is unknowable in a real detector (forgoing an impractically well controlled experiment). The purpose of n_{incl} is to approximate n_{real}; so if n_{real} was known and useful then we would simply use that directly. Note that the purity is directly related to the particle identification efficiency. We will avoid discussing different types of efficiency, however, to avoid confusion with the overall analysis efficiency.

Although purity may not be measured directly from data, it is possible in Monte Carlo simulation. Our Monte Carlo will be discussed extensively in section 4.1, but for now it is sufficient to know that a Monte Carlo which simulated the collision, the PHOS geometry, and the analysis itself was performed. In Monte Carlo, it is possible to know the identity of the source particle which generates each cluster observed in the PHOS geometry. The source particle of every cluster which passes the inclusive photon cuts is checked and, if a photon, will contribute to the numerator of the purity fraction. Ideally, $\mathcal{P} = 1$. Note that for some analysis, the purity may also be called the particle identification efficiency.

Using the above method, the purity was calculated in each p_t bin and can be observed in Fig. 2.17

2.4.3 Inclusive Photon Invariant Yield

The culmination of all of these cuts is the inclusive photon invariant yield, an experiment invariant quantity which describes the inclusive photon flux expected per collision in each transverse momentum bin.

$$\gamma_{incl}(p_t) = \frac{1}{N} \frac{\mathcal{P}}{\epsilon A} \frac{dn_{incl}}{dp_t} \tag{2.7}$$

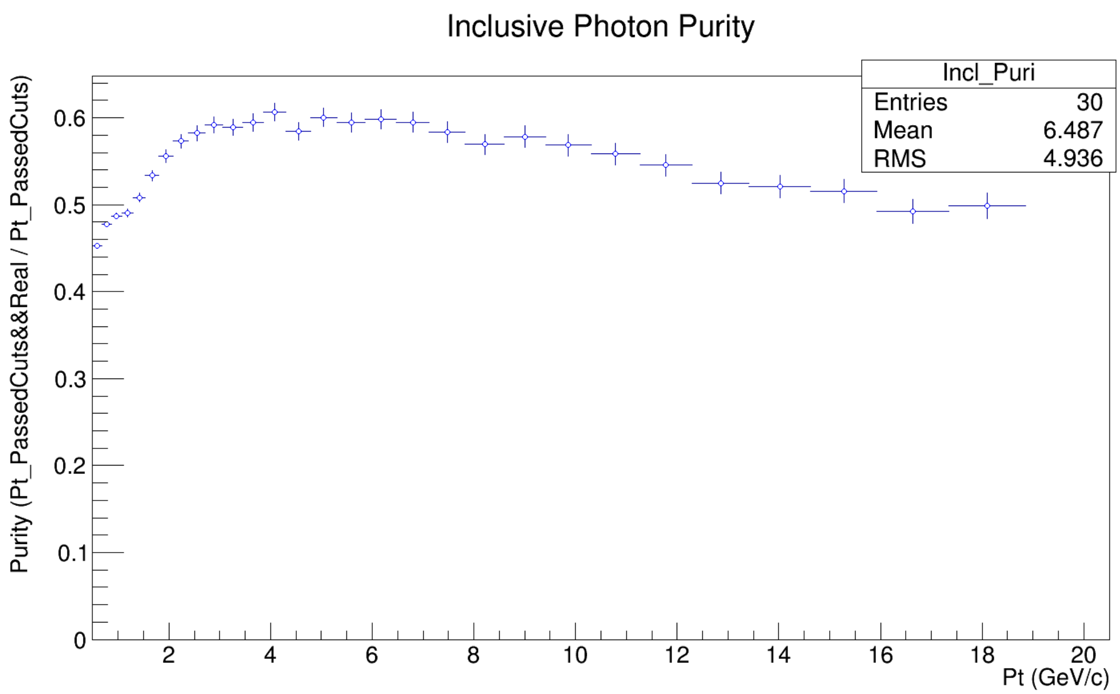

Figure 2.17. Inclusive Photon purity in each p_t bin using the method described in section 2.4.2.

Where n_{incl} is the number of inclusive photons detected, $\mathcal{P}$ is the purity, ϵ is the efficiency, N is the number of events, and A is the ratio of the detector acceptance to the total acceptance.

Note that A is simply the fraction of the solid angle subtended to the detector from the vertex and the total solid angle. That is:

$$\phi = 2\arctan(e^{-\eta}) \tag{2.8}$$

$$\theta_{PHOS} = \left[2\pi * \frac{220}{360}, 2\pi * \frac{320}{360}\right] = [3.84, 5.58] \tag{2.9}$$

$$\eta_{PHOS} = [-0.12, 0.12] \Rightarrow \phi_{PHOS} = [1.45, 1.69] \tag{2.10}$$

$$A = \frac{d\phi_{PHOS} d\theta_{PHOS}}{4\pi} = 0.0332 \tag{2.11}$$

The final inclusive photon invariant yield is shown in Fig. 2.18, while the normalization prefactor, $\frac{1}{N}\frac{\mathcal{P}}{\epsilon A}$, is shown in Fig. 2.19.

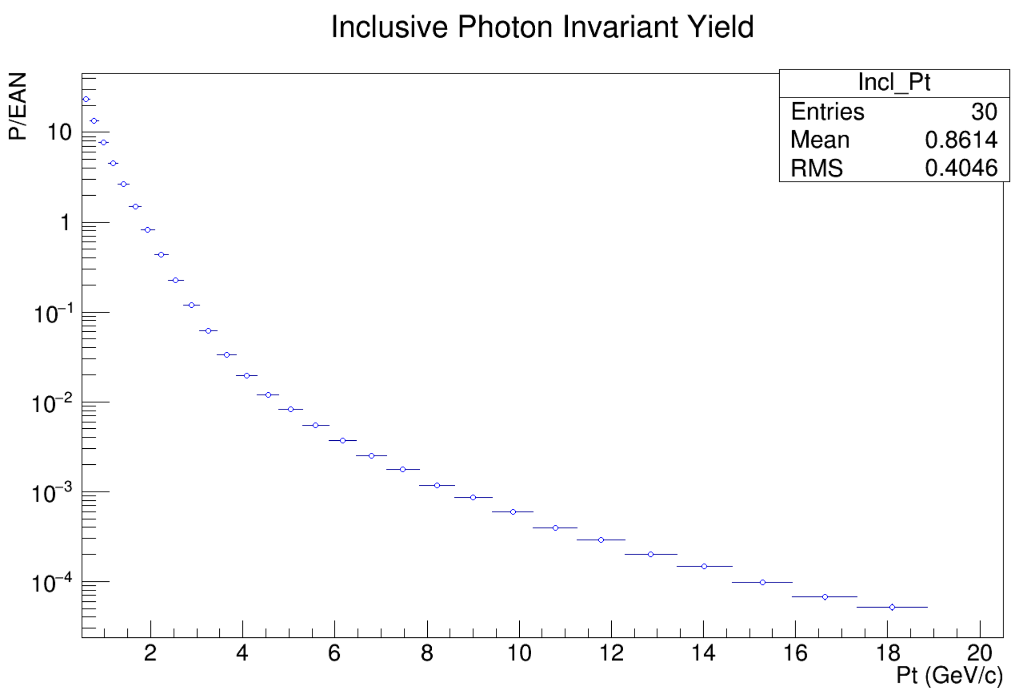

Figure 2.18. LHC11h PbPb data at $\sqrt{s_{NN}} = 2.76$ TeV inclusive photon invariant yield.

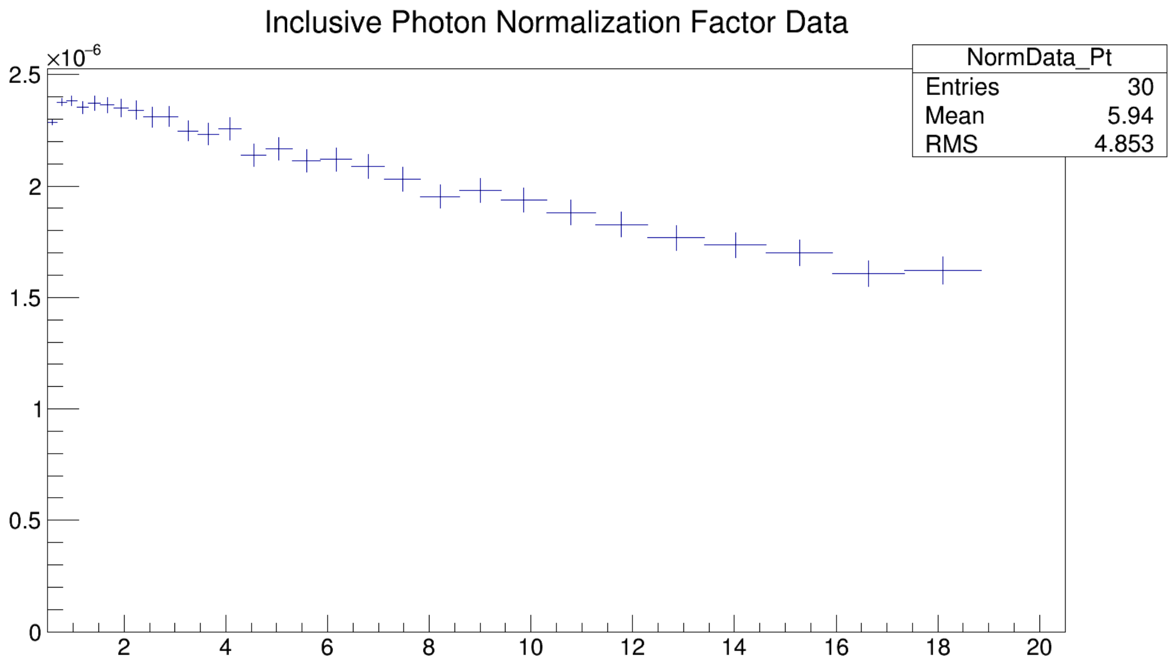

Figure 2.19. LHC11h PbPb data at $\sqrt{s_{NN}} = 2.76$ TeV inclusive photon normalization prefactor, $\frac{1}{N}\frac{\mathcal{P}}{\epsilon A}$.

3. NEUTRAL MESONS

3.1 Photonic Background

3.1.1 Neutral Meson Exclusion

When studying direct photons, the primary source of photonic background is neutral meson decay. At the ALICE experiment, neutral pions make up a nontrivial ratio of the produced particle species, and typically decay to the 2γ channel with $\Gamma_{\pi^0\to\gamma\gamma}/\Gamma_{\pi^0} = 0.98798$ [27] on a characteristic length scale of ~ 22 cm. As such, π_0 decay dominates the photonic background in heavy ion collisions. Another neutral meson that non trivially contributes is the η with $\Gamma_{\eta\to\gamma\gamma}/\Gamma_{\eta} = 0.3941$ [27]. Roughly 80% of the decay mesons are from neutral pions, while 18% are from etas. Much less commonly, other diphoton meson decays can contribute as well, such as the $f_0(600)$. An estimation of the relative contribution of different photonic sources in a heavy ion collision has been done in the past [34].

With these sources in mind, it is impossible to tell if any single photon candidate cluster is caused by a direct photon. The "true" direct photon spectrum can not be measured directly. Therefore, we must rely on a purely mathematical method to isolate direct photons with a high purity. To do with, we use the double ratio method (recall section 1.3.3).

3.1.2 Diphotons

One crucial element of the double ratio is the pion spectrum. To estimate the pion spectrum, a photon matching method was used. The basic premise is to exhaustively pair each photon candidate (i.e. a cluster that passes basic QA, CPV, and shower shape cuts) in a single event with each other photon candidate to produce a two photon system (a diphoton). Each photon candidate's four momentum information is well known (see Chapter 2 for details), so the diphoton's four momentum is simply:

$$p_{di} = p_1 + p_2 \tag{3.1}$$

And thus the mass and transverse momentum can be computed using the typical Einstein relations and geometric projections (that is: $m = \sqrt{E^2 - p_x^2 - p_y^2 - p_z^2}$ and $p_t = \sqrt{p_x^2 + p_y^2}$).

The m and p_t values for each diphoton pair are recorded and plotted in a two dimensional histogram. The number of counts in each histogram bin form a multivariate probability density function.

In general, the form of the diphoton probability density function is:

$$F(m, p_t) = \pi(m, p_t) + M(m, p_t) + C(m, p_t) \tag{3.2}$$

where F is the diphoton probability density function, π is the pion signal, M is the mound (See section 3.2.1), C is the combinatorial background, m is the mass coordinate, and p_t is the transverse momentum coordinate. The observant reader might note that m and p_t are *not* independent variables ($m = \sqrt{E^2 - p_t^2 - p_z^2}$), and therefore this density function is not in an orthonormal coordinate system. However, p_z is somewhat free to vary within the acceptance of the photon spectrometer in pseudorapidity, and E is free to vary liberally for each diphoton pair. Since that information is not carried by this plot, we disregard it. Therefore in this multivariate analysis, we simply assume that m and p_t are in fact independent observables. While there might be some correlation between the two, we are free to simply pretend that the correlation is coincidental with no loss in generality. The measured $F(m, p_t)$ can be observed in Fig. 3.1.

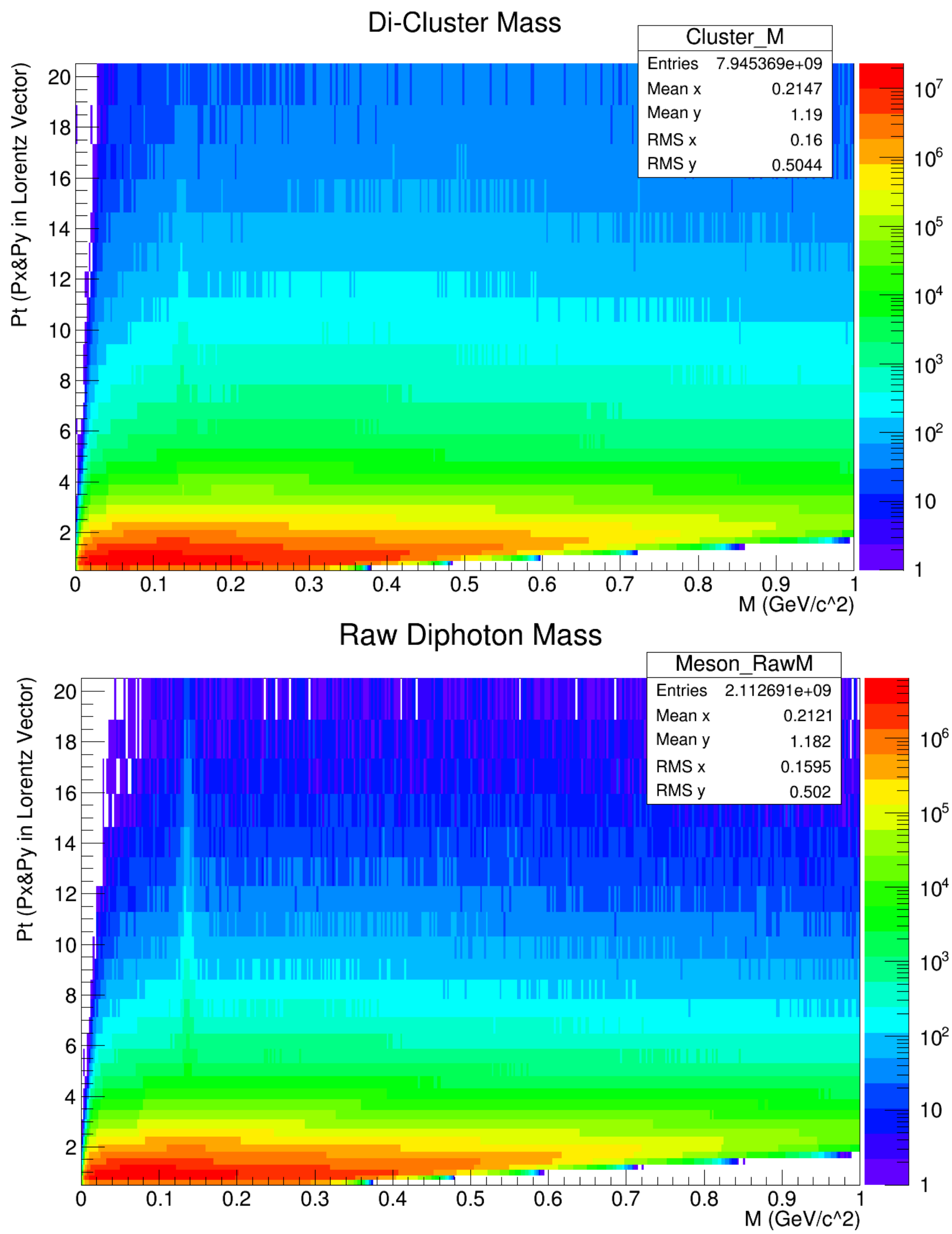

Figure 3.1. Diphoton mass and transverse momentum. Minimum Bias (left) and after QA and shape cuts (right).

3.1.3 Mixed Events

Of course, any given diphoton may not consist of two related photons. These photons are combinatorial background and must be estimated and subtracted to isolate related photon pairs and thus isolate the pion signal. To estimate the combinatorial background, a “mixed event method” was used. Since photon pairs can only be related if they are generated in a single event, mixed pairs can be created by matching photons from different events.

To generate these mixed pairs, each photon in an event would be matched with all other photons *not* in that event, but in a similar one. It is necessary that the events be similar in order accurately simulate the same event combinatorial background. If, for example, two photon candidates from events with very different centralities were matched, then the resulting very different photon multiplicities might cause over counting of the peripheral event photons, which could introduce unexpected correlations in the mixed photon pairs.

To determine event similarity, all events were divided into bins in a three dimensional array based on their centrality, event plane, and z coordinate of their reaction vertex. In this way, only qualitatively similar events would share a bin. Several different bin configurations were tried in small tests. Initially ten bins were used in each coordinate, but this resulted in memory issues ($10^3 = 1000$ bins). It was then decided to use five bins in each dimension ($5^3 = 125$ bins total). However, this resulted in too few valid mixed photon pairs in low event samples. Very central events would often be alone in their bin, resulting in zero central event mixed photons. Therefore, the number of bins in z-vertex was reduced to one ($5^2 * 1 = 25$ bins total), since varying the number of z-vertex bins didn’t seem to change the shape of the estimated combinatorial density function.

The mixed event photo profile can be seen in Fig. 3.2.

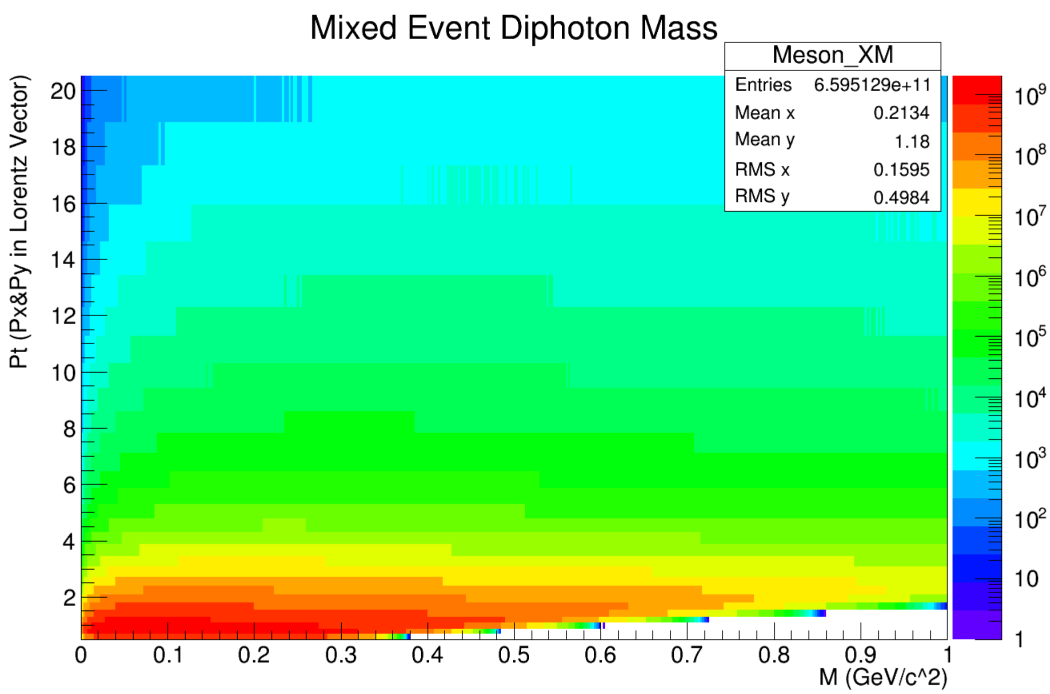

Figure 3.2. Mixed event diphoton mass and transverse momentum.

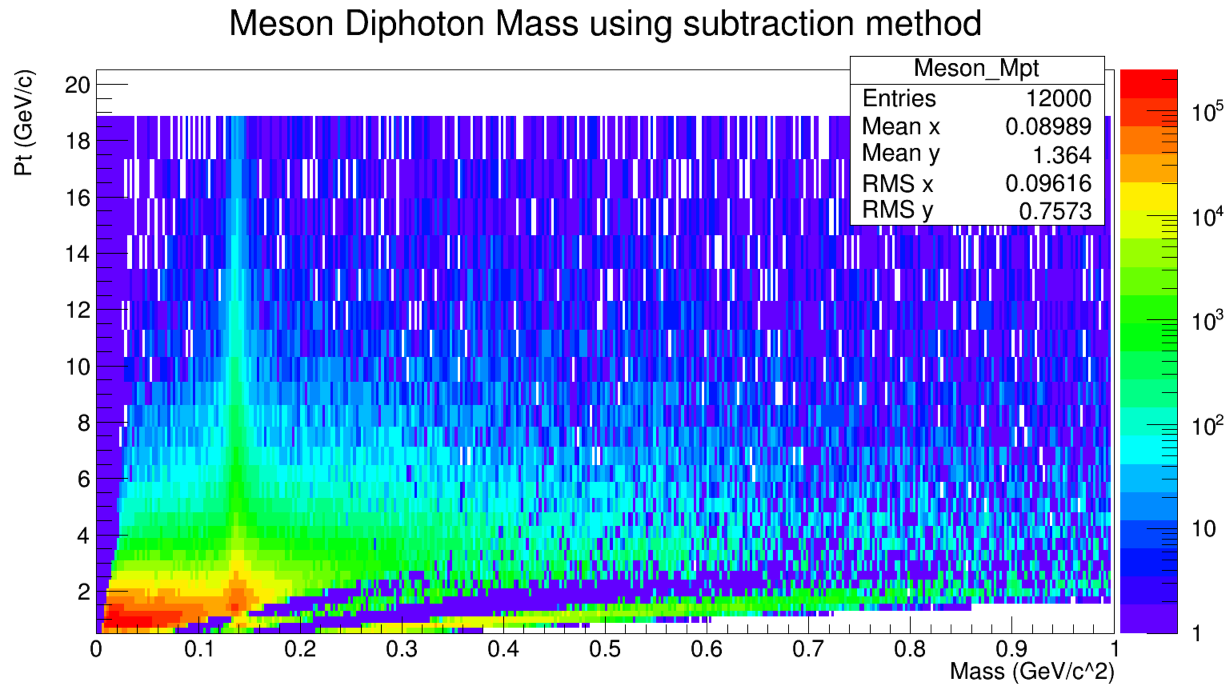

Figure 3.3. Diphoton profile less normalized mixed diphoton profile.

3.2 Additional Diphoton Background

3.2.1 The Mound

After combinatorial background subtraction (Fig. 3.1.3), it was observed that the non-pion signal was not entirely removed and indeed contributed non trivially to the diphoton distribution (Fig. 3.3 and 3.4). Given the skew of the unsubtracted non pion background in transverse momentum - mass phase space, this additional signal was informally referred to as the mound.

The mound can be observed to fall off apparently exponentially in mass and p_t, except for near the axis, where it predictably drops quickly to zero (See discussion of pion detection efficiency in section 3.2.2 for details of that phenomenon). Since the mound is observed even after combinatorial background subtraction, this suggests that it is not merely statistical in nature: there is some physical or detector

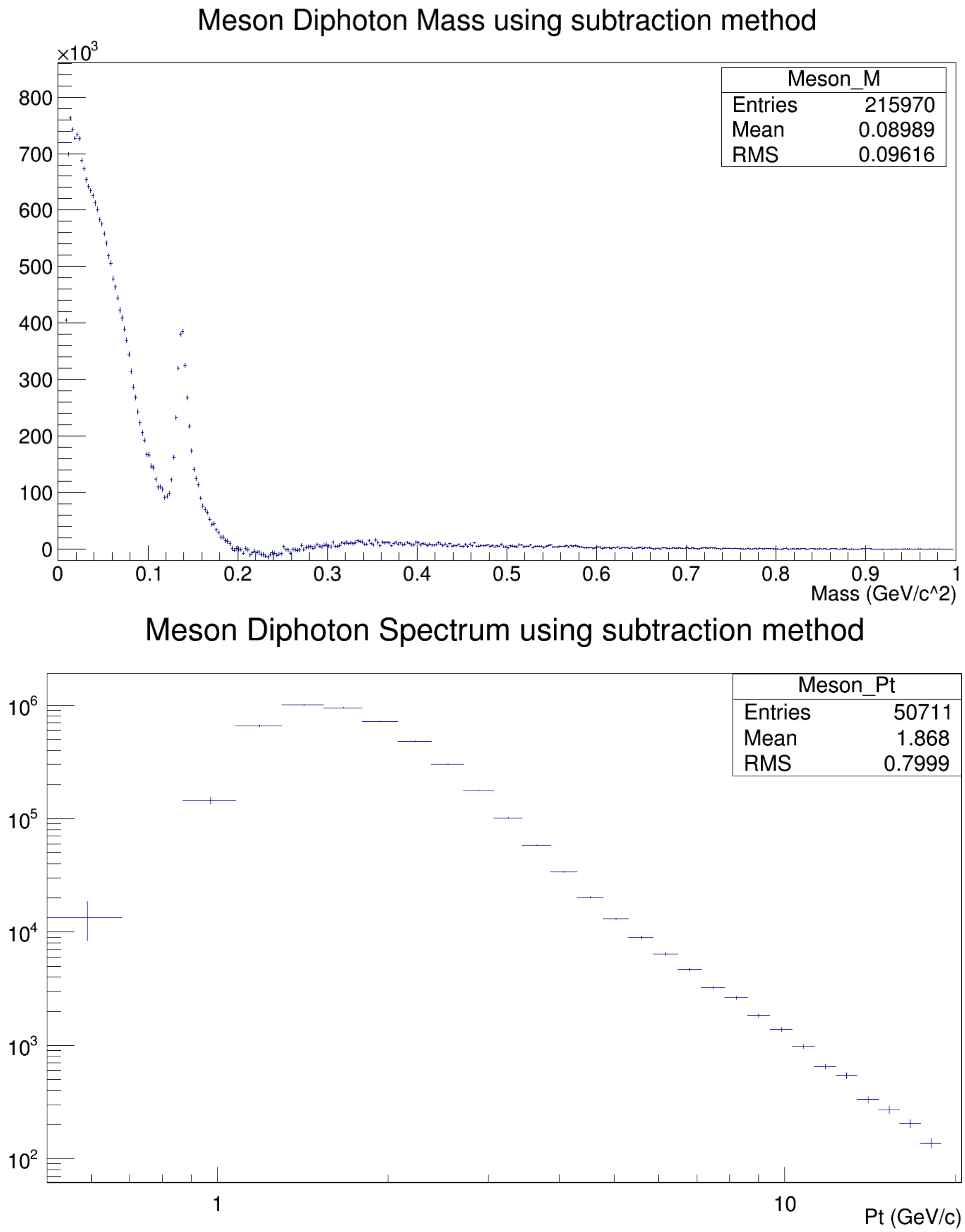

Figure 3.4. Diphoton less normalized mixed diphotons profile projected along mass (top) and transverse momentum (bottom) axis.

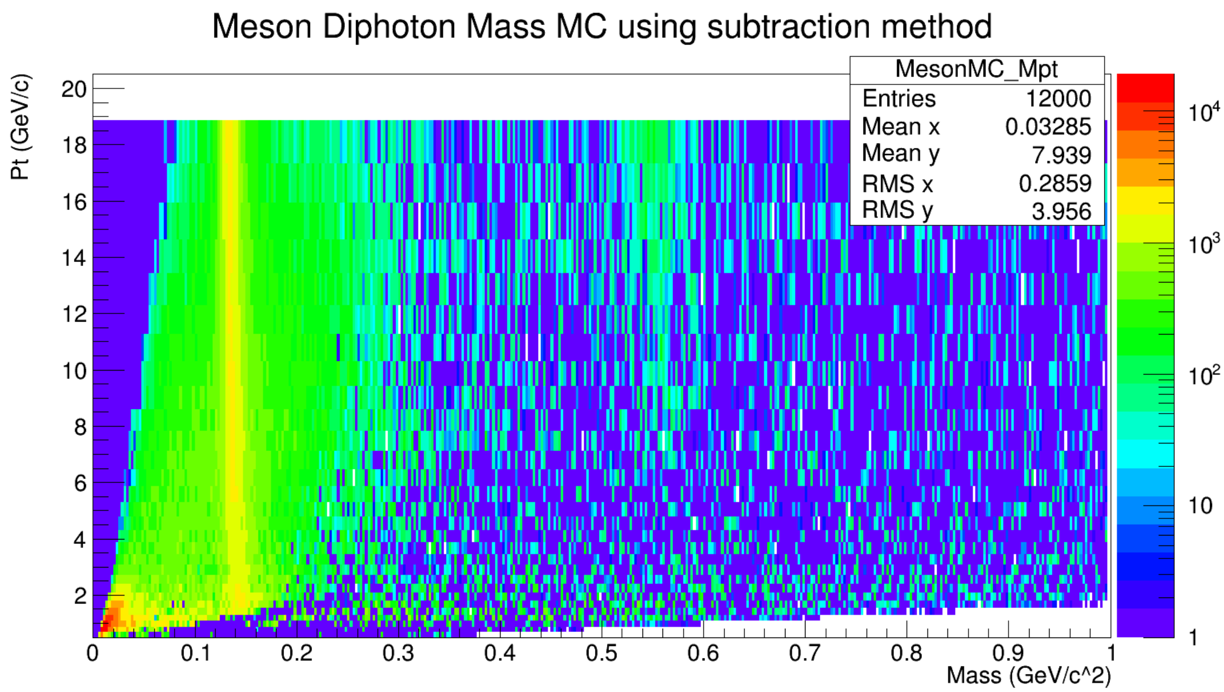

Figure 3.5. Diphoton less normalized mixed diphoton profile in Monte Carlo.

phenomenon that is causing it - such as perhaps some systematic bias introduced by the choice of cuts or even bias introduced by unexpected interactions in the TPC or PHOS. However, no immediate cause of the mound is readily suggested by the data, and minor variation in cuts do not significantly affect it. The mound can also be seen to be present in Monte Carlo analysis as well (Fig. 3.5).

While the cause of the mound certainly warrants further study, it is ultimately not directly meaningful in the scope of this particular analysis. The mound maxima appears well below the region of interest in mass for our neutral pion study (Fig. 3.4). The exponential tail of the distribution does slightly inflate the pion measurement. And indeed, it does so nontrivially; the contribution is enough to artificially deflate the double ratio if it is not compensated for. It was therefore decided that the contribution from the mound must be subtracted from the final pion measurement in order to prevent possible added bias. Since the cause of the mound is unknown, it was decided to isolate it from the pion signal using a numerical multivariate analysis in transverse momentum - mass phase space.

3.2.2 Multivariate Analysis

After combinatorial background has been subtracted (see 3.1.3), we are then only left with parameterizing $\pi(m, p_t) + M(m, p_t)$. If the form of $\pi(m, p_t) + M(m, p_t)$ were known, numerical methods could be used to minimize the chi square per degree of freedom of the fit, and thus compute any parameters. We can't know the exact form of this function, but it should be possible to guess the form while minimizing the χ^2/dof in the subspace of interest. For this analysis, a subspace of $m = (0.08, 0.2)$ and $p_t = (1.7, 20)$ was chosen as the region of interest. Note any values of $M(m, p_t)$ or $\pi(m, p_t)$ outside this region must be extrapolation only and may not match the observed or real local trend.

By inspection of the plot, it appears that $\pi(m, p_t) + M(m, p_t)$ is separable and the form of $\pi(m)$ is a resonance structure in mass ($\pi(m) = Ae^{\frac{-(m-B)^2}{2C^2}}$). Here B is just the center of the Gaussian, which is fixed to simply the pion mass, $m_{\pi^0} = 134.98\frac{MeV}{c^2}$. A and C are allowed to fluctuate as free parameters.

The multivariate function:

$$\pi(m, p_t) + M(m, p_t) = (Ae^{\frac{-(m-B)^2}{2C^2}} + De^{-Fm}) * e^{G\ln(Hp_t)} \tag{3.3}$$

was used to fit the plot, where m is mass, p_t is transverse momentum, and A,B,C,D,F,G, and H are free parameters. The results are shown in Fig. 3.6. This suggest the form of the pion signal to be:

$$\pi(m, p_t) = Ae^{\frac{-(m-B)^2}{2C^2} + G\ln(Hp_t)} \tag{3.4}$$

With a relative contribution from the mound of $\frac{\int \pi(m,p_t)dm}{\int \pi(m,p_t)+M(m,p_t)dm} = \frac{A}{A+D}$. Therefore,

$$\pi(p_t) = \frac{A}{A+D} * e^{G\ln(Hp_t)} \tag{3.5}$$

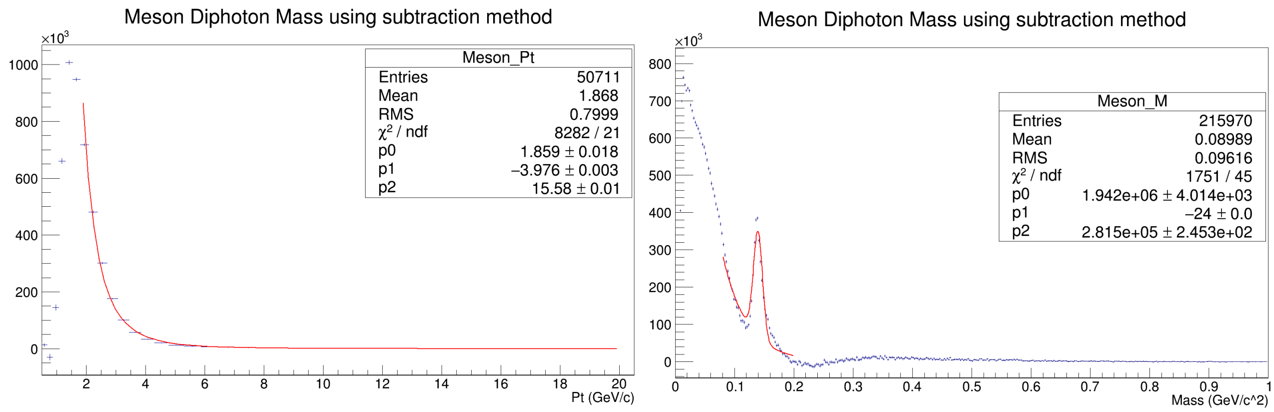

Figure 3.6. Fit multivariate function.

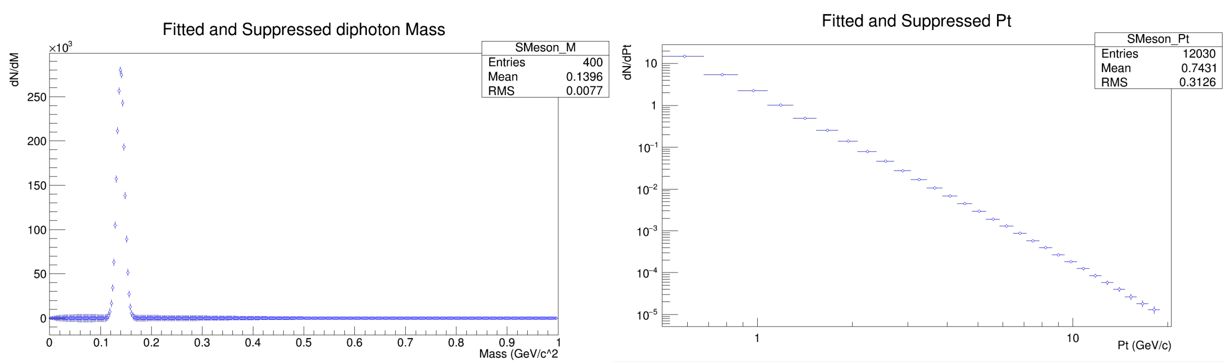

Figure 3.7. Mound suppressed pion profile.

This is shown in Fig. 3.7. This matches previous neutral pion studies within error [78].

Note that the pion fit used necessarily extrapolates the lowest p_t bins. This is because the limited acceptance of PHOS causes a sharp drop in diphoton detection efficiency at low p_t. The explanation for this phenomenon is that, as p_t decreases, the opening angle of the decay photons will be forced by kinematics open wider. Since the pion lifetime is limited (flight distance of neutral pions is on the order of millimeters), when the opening angle widens there is a sharply increasing probability that one - but not both - photons will enter the PHOS acceptance. Thus, PHOS's ability to detect

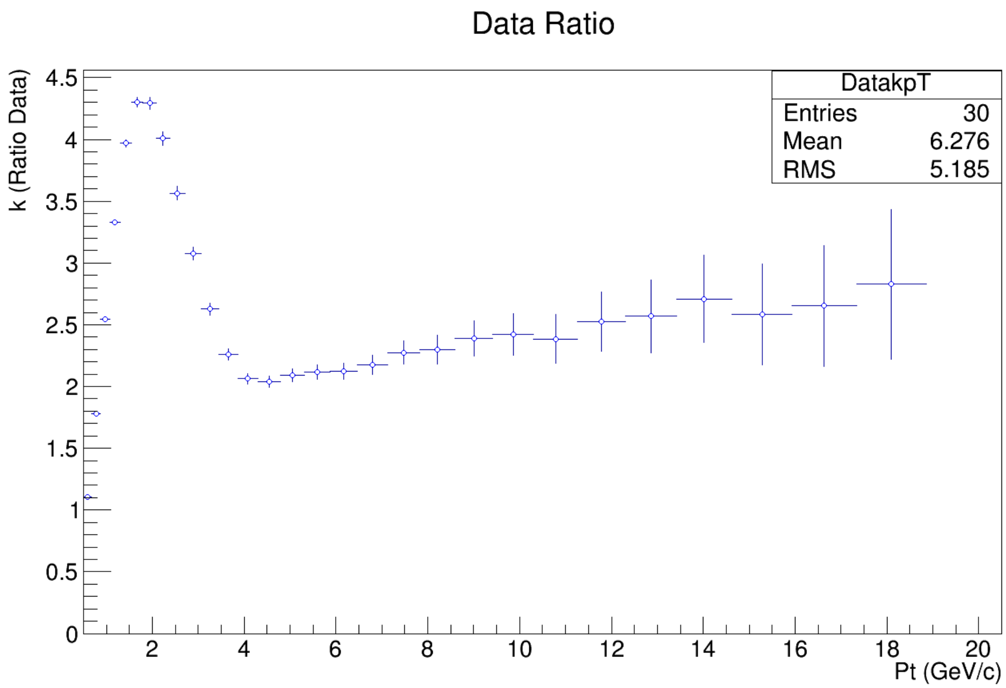

Figure 3.8. Data single ratio, $\frac{\gamma_{incl}}{\pi^0_{data}}$.

diphotons is severely hampered below about $p_t \simeq 1.7$ GeV. To compare to inclusive photons at ultra low p_t, a small extrapolation is required.

3.2.3 Data Single Ratio

It is now possible to compute the so called "single ratio", $\frac{\gamma_{incl}}{\pi^0_{data}}$ using the results for the inclusive photon spectrum and the derived neutral pion measurement. It can be seen in Fig. 3.8.

Note the rapid rise and fall in the thermal photon regime. Recall section 3.2.2 that below $p_t \simeq 1.7$ GeV, results should be regarded with some skepticism because of the necessary extrapolation. While it's still too early to draw any conclusions from this (we still need to compare to expected results from Monte Carlo), it is still possible to already make some observations. One can observe while $\frac{\gamma_{incl}}{\pi^0_{data}}$ is roughly stable above the thermal photon threshold, there is a significant excess of photons at low p_t. After a comparison to Monte Carlo, it will be possible to determine if this is evidence of thermal photon activity.

4. PHOTONIC SUPPRESSION

4.1 Monte Carlo

4.1.1 Monte Carlo

After the normalized inclusive photon spectrum (section 2.4.3) and the pion spectrum (section 3.2.2) is obtained, it is now only necessary to obtain the MC single ratio. The simulation was performed by the ALICE collaboration on simulation LHC14a1a, LHC14a1b, and LHC14a1b (0-10%, 10-50%, and 50-90% centrality classes, respectively); the exact run numbers are again available in appendix B. LHC14a1(abc) MC is created in Pythia 8 and reproduces PbPb interactions at 2.76 TeV in the ALICE geometry with LHC11h anchors. The same analysis (with the same cuts) was performed as in the previous section on this simulation data set. Tender was not applied, because (as we shall discuss) it was not needed. The summarizing plots can be viewed in Fig. 4.1.

This Monte Carlo can not be taken too seriously, since HIJING is known not to accurately reproduce the relevant spectra at LHC energies [79]. In particular, the pion spectrum obtained directly from HIJING is very different from the known pion spectrum obtained by previous analysis [78] and similarly the pion spectrum obtained in this analysis. The comparison can be see in Fig. 4.2.

This is particularly a problem insofar as the double ratio depends heavily on the MC and real data pion spectrum being consistent:

$$\frac{\pi^0_{MC}}{\pi^0_{Data}} = 1 \tag{4.1}$$

$$R \equiv \frac{\gamma_{incl}}{\gamma_{decay}} = \frac{\gamma_{incl}}{\gamma_{decay}} * \frac{\pi^0_{MC}}{\pi^0_{Data}} \tag{4.2}$$

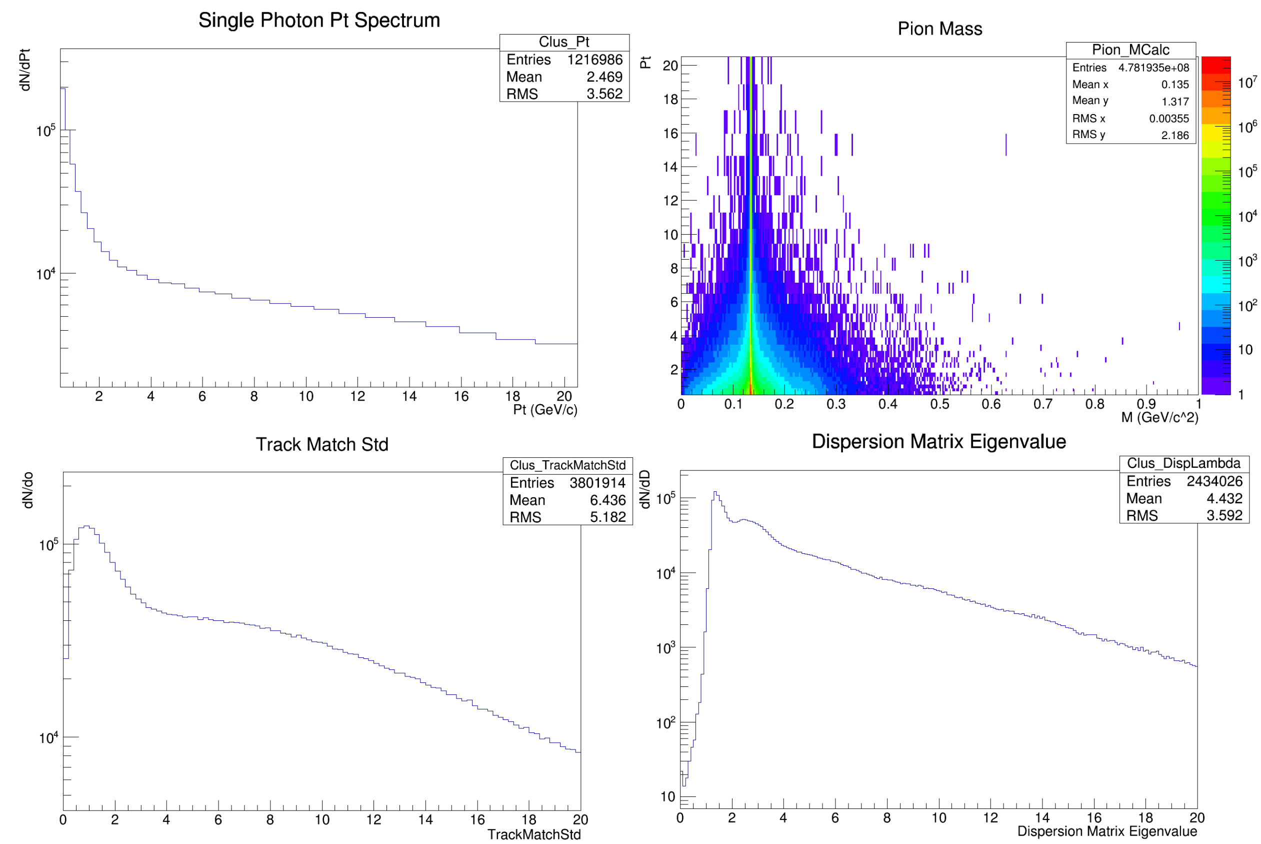

Figure 4.1. The inclusive spectra from MC (top left), pion mass and transverse momentum distribution (top right), CPV (bottom left), dispersion matrix cut (bottom right).

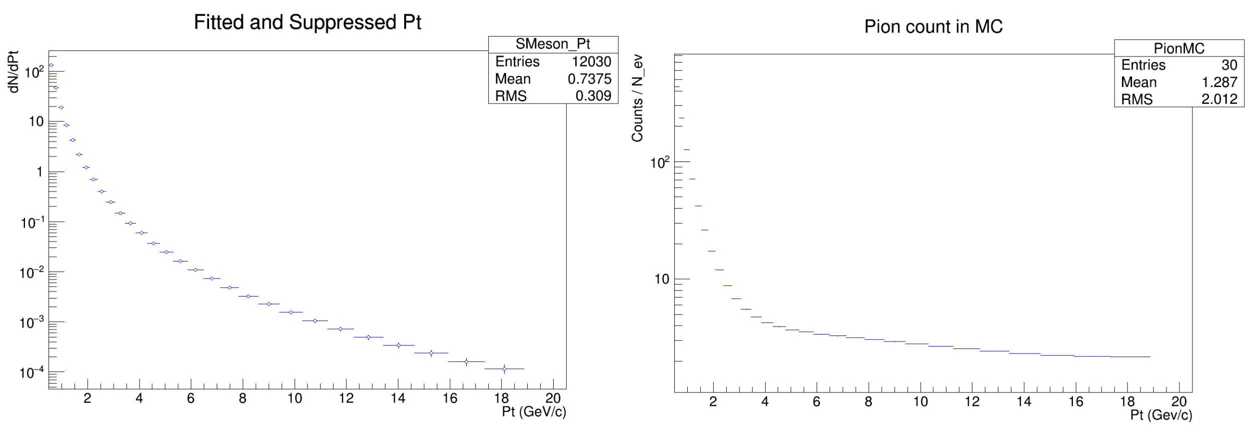

Figure 4.2. Neutral pion spectrum obtained from real data LHC11h (left) and neutral pion spectrum provided by HIJING LHC11a1b (right). Notice significant inconsistencies.

To correct for this, previous analysis [38] have used a so called cocktail simulation which corrects the MC spectrum by isolating HIJING the inconsistency with data and scaling those results based on the relative fraction of product hadron flavors in each transverse momentum bin. For technical reasons this previously generated cocktail is unavailable for this analysis, however even if it was, this cocktail is not optimized to expand its results to Proton-Proton collisions (section 4.3) and therefore would not available for that crucial part of this analysis. A different method is needed.

4.1.2 Cocktail

To correct the data reproduction inconsistency in HIJING, I created my own narrow focused toy cocktail. The idea is simple: assume the relative flavor ratios of the collision product particles predicted by HIJING is correct (this assumption was also made in the old cocktail), and simply scale each particle species by the neutral pion Data to MC ratio and "decay" them in the diphoton channel to create the MC decay photon spectrum. In particular, we care only about the Pion and Eta spectra (other diphoton decay channels proving ultimately inconsequential, contributing less than 2% to the decay photon spectrum [29]). The pion and eta spectrum reported by HIJING are available in Fig. 4.3. To force consistency with data, we multiply by the particle spectra by the pion data to MC ratio. By design, this will force $\frac{[\pi^0]_{Data}}{[\pi^0]_{MC_{toy}}} = 1$ in every transverse momentum bin, an important assumption of the double ratio.

$$R \equiv \frac{\gamma_{incl}}{\gamma_{decay}} = \frac{\gamma_{incl}}{\gamma_{decay}} \frac{[\pi^0]_{MC_{toy}}}{[\pi^0]_{Data}} = \frac{\frac{\gamma_{incl}}{\pi^0_{data}}}{\left[\frac{\gamma_{decay}}{\pi^0}\right]_{MC_{toy}}} \tag{4.3}$$

$$[\pi^0]_{MC_{toy}} = [\pi^0]_{Data} \Leftrightarrow [\pi^0]_{MC_{toy}} = [\pi^0]_{MC} \frac{[\pi^0]_{Data}}{[\pi^0]_{MC}} \tag{4.4}$$

$$[\eta^0]_{MC_{toy}} = [\eta^0]_{MC} \frac{[\pi^0]_{Data}}{[\pi^0]_{MC}} \tag{4.5}$$

Now all that is needed is to simply simulate the decay of each of these product particle flavors and scale to the PHOS acceptance. The modified $[\pi^0]_{MC_{toy}}$ is normalized

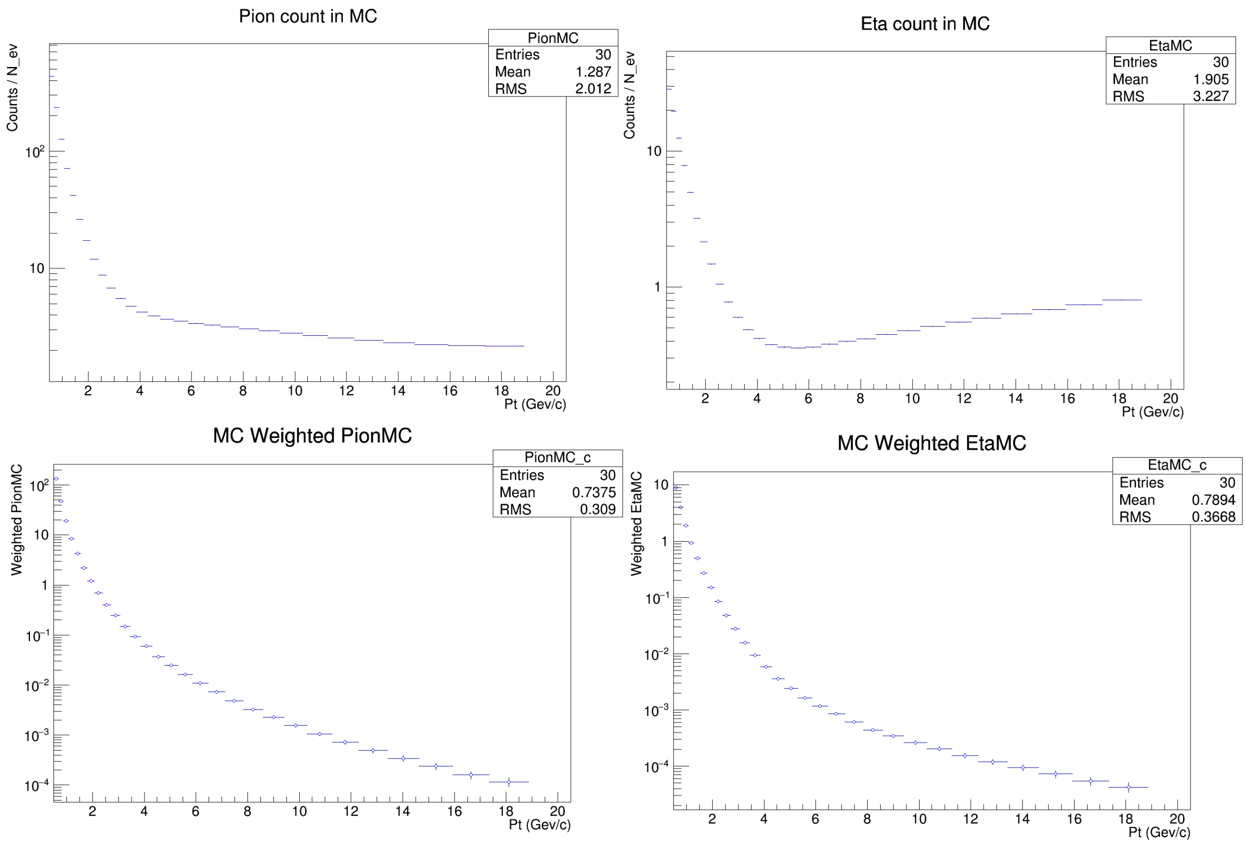

Figure 4.3. π^0 and η before (top left and right, respectively) and after (bottom left and right) HIJING weight.

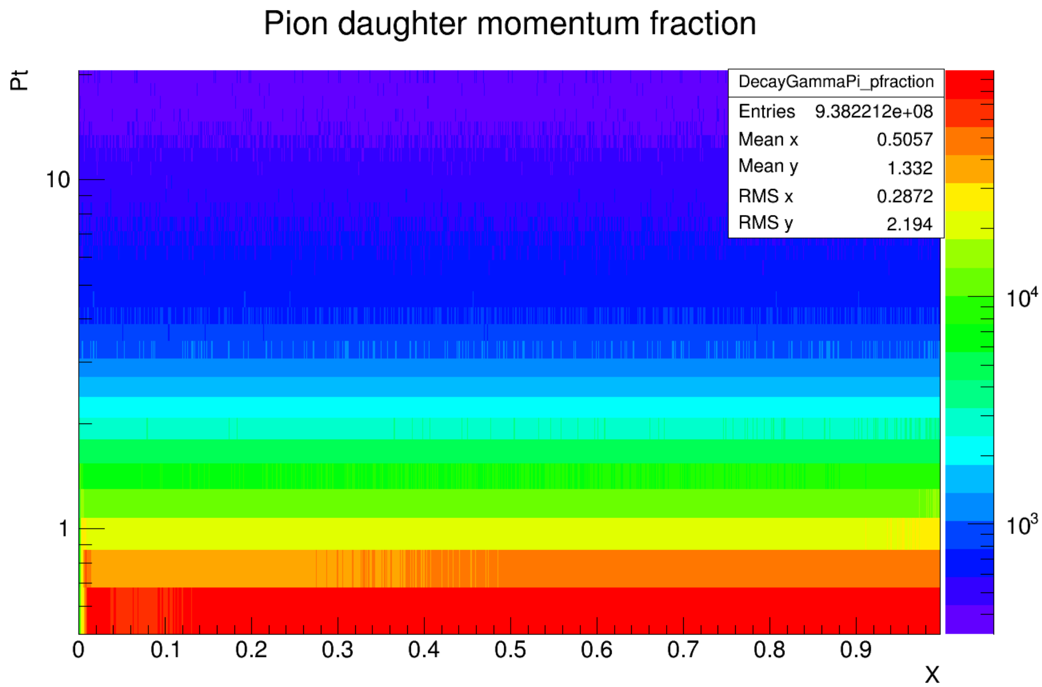

Figure 4.4. Decay photon momentum fraction of parent pion.

to one and used as a probability density function. For each neutral pion candidate in Fig. 4.3, a random transverse momentum is generated according to the $[\pi^0]_{MC_{toy}}$ probability density function. Then two decay photon particles are randomly generated such that the transverse momentum of the generated pion is conserved. The distribution of the decay photon transverse momentum as a fraction of the initial pion's transverse momentum was initially unknown. In order to determine this, HIJING was consulted and this fraction computed for each neutral pion. It turns out the distribution is flat in each p_t bin. The results can be seen in Fig. 4.4. A similar procedure was performed using η, and $[\eta^0]_{MC_{toy}}$.

Since the original analysis only includes π^0 and η up to 20 GeV/c, and those can only decay to lower p_t bins, the limit to the original transverse momentum binning will deform the decay photon results in the highest bins. Those bins will be thrown out to mitigate their effect on this analysis, but this method could be extended to

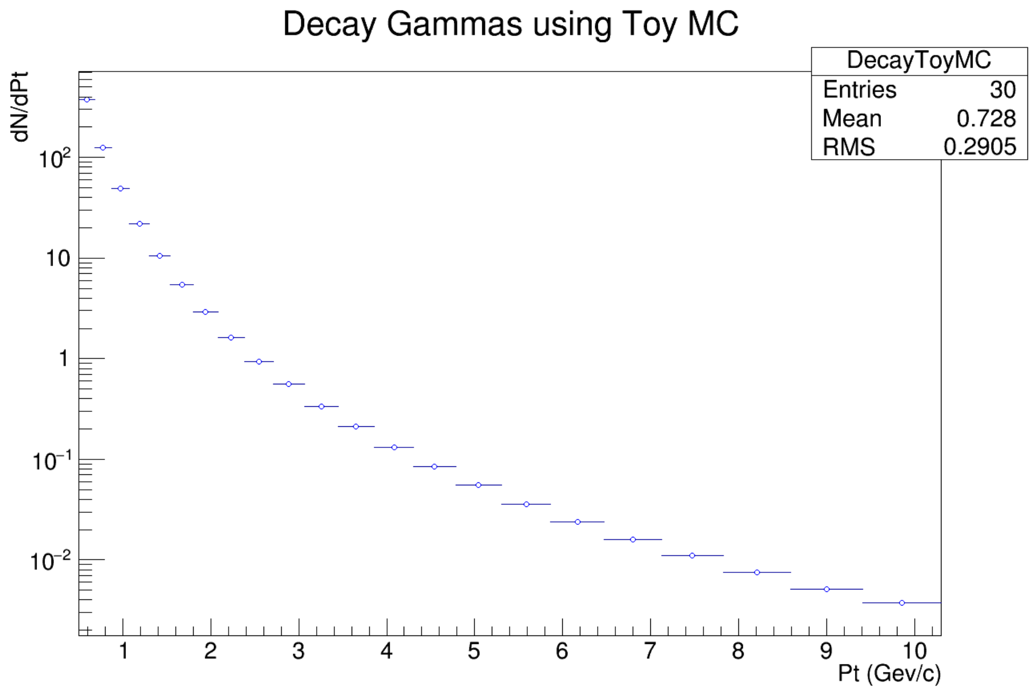

Figure 4.5. Decay photon spectrum $\frac{\gamma_{incl}}{\pi^0_{data}}$

include those lost bins by simply including more p_t bins and increasing statistics correspondingly.

The decay photon results are then added for etas and pions to produce the toy decay photon spectrum seen in Fig. 4.5.

4.1.3 MC Single Ratio

Now that the decay photon spectrum is available, we simply take its ratio with respect to $[\pi^0]_{MC_{toy}}$ to find the double ratio denominator. The results are available in Fig. 4.6.

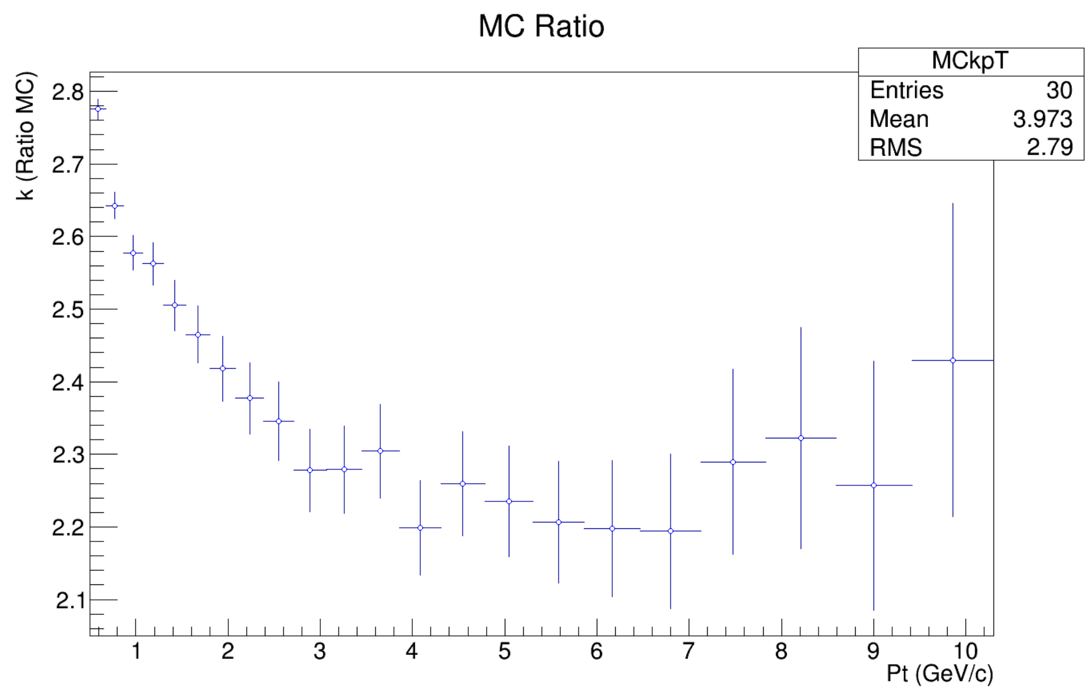

Figure 4.6. MC single ratio, $\left[\frac{\gamma_{decay}}{\pi^0}\right]_{MC}$.

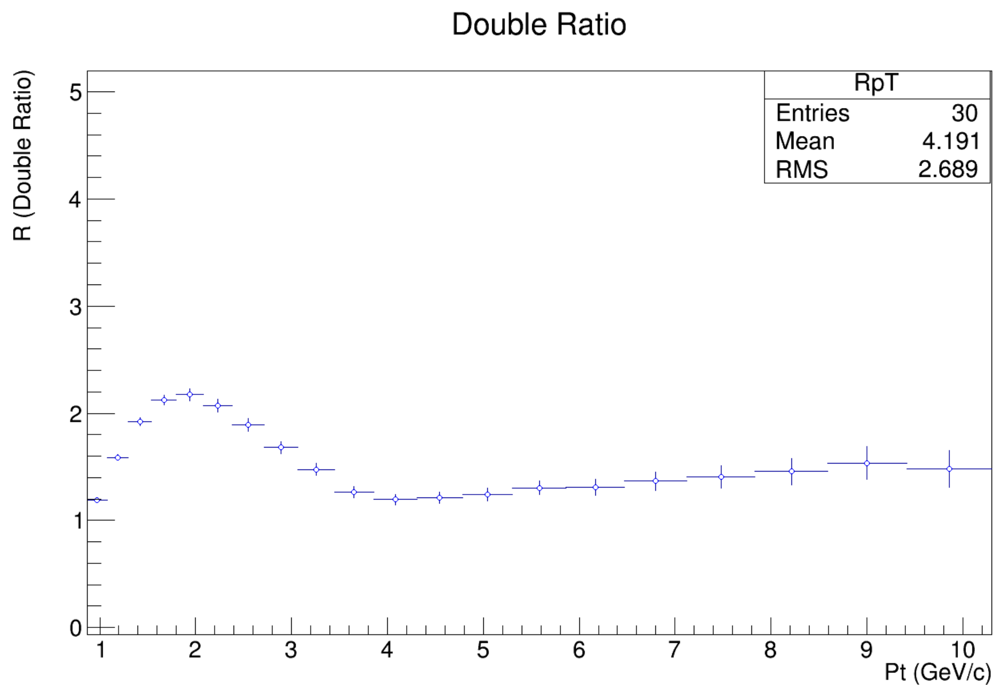

Figure 4.7. PbPb Double Ratio, $R \equiv \frac{\gamma_{incl}}{\gamma_{decay}} = \frac{\frac{\gamma_{incl}}{\pi^0}_{data}}{\left[\frac{\gamma_{decay}}{\pi^0}\right]_{MC}}$.

4.2 Lead-Lead Spectrum

4.2.1 Double Ratio Results

The single ratios are used to finally obtain the double ratio for PbPb collisions at 2.76 TeV in Fig. 4.7.

To assist in interpretation of this, remember that this is in principal just the observed photon spectrum divided by the predicted decay photon spectrum. Therefore, any surplus above 1 can be interpreted as a sign of direct photons in that p_t bin. The observed result is only slightly above 1 and monotonically increasing in all regions after 4 GeV/c. However, below 4 GeV/c there is a sharp increase in observed photons in excess of what might be expected from decay photons alone. It's worth noting that this sharp increase occurs in the thermal photon regime. Unfortunately, these results can not be extrapolated to $\lesssim$ 1.2 GeV/c because of uncertainty in the neutral pion

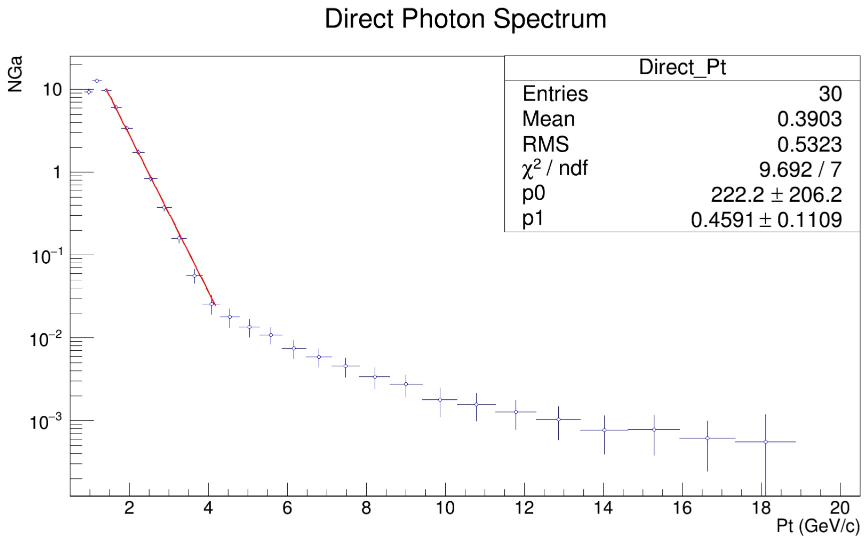

Figure 4.8. PbPb Direct photon spectrum at $\sqrt{s_{NN}} = 2.67$ TeV

measurement in the lowest p_t bins. Detector uncertainty due in this region can be explained by limited PHOS acceptance. As the momentum decreases, the decay photon opening angle increases due to kinematics, and thus the relative likelihood that both photons fall within the acceptance decreases sharply below a certain threshold.

4.2.2 Thermal Photon Spectrum

It is now possible to compute the PbPb direct photon spectrum at $\sqrt{s_{NN}} = 2.67$ TeV in Fig. 4.8.

In the thermal regime, the inverse slope parameter is computed to be 459 ± 110 MeV. Note that this inverse slope parameter is without pQCD photons subtracted, and is thus rather higher than the "true" thermal photon temperature. It is consistent within error to results previously at ALICE [73]. As discussed from the beginning (section 1.4.1), I caution against immediately associating this with a temperature measurement since it remains to be seen when these thermal photons were omitted. In order to do that, we need to first consider the results from proton-proton collisions.

4.3 Proton-Proton Spectrum

4.3.1 Proton-Proton Benchmark

As discussed in section 1.4.2, the photonic nuclear suppression can't be computed with the direct photon spectrum alone. A perturbative quantum chromodynamic benchmark is needed to know the expected thermal photon yield from known physics. If the observed thermal photon spectrum is underestimated by pQCD, then the likely culprit is thermal photons being reabsorbed in the nuclear plasma before they escape - a telltale sign that the thermal photons have a low mean free path as they traverse the quark-gluon fireball.

While it is certainly possible to estimate the pQCD prediction directly from theory [80], it is perhaps more convincing as an experimentalist if one uses real data from pp collisions and then simply scales that result to PbPb. To date it is unclear if the QGP is formed in pp collisions [81, 82], but if it is formed the system is too small to be expected to greatly suppress photons (or hadrons - for that matter). If it is not, then the results will be exactly the same as predicted by pQCD. Either way, the motivation to use pp data as a benchmark to compare to PbPb remains unaffected; it is an ideal estimation of how a small subsection of the strongly interacting lead ions would behave in isolation.

Of course, the lead ions have much more nucleons depending on the collision centrality, so the results will need to be scaled by the expected number of participating nucleons, $\langle T_{AA} \rangle$. The Glauber model provides the tools to do exactly this [48]. See a walk through of this derivation in section 4.4.1.

4.3.2 Proton-Proton Inclusive Photon Spectrum

To obtain the pp inclusive photon spectrum, the identical methods were used as the PbPb analysis. It's useful to use an identical procedure, in order to ensure that the observed results in the two particle species are comparable. Nonetheless, some differences in approach will be required, and are discussed in this section. It was also ensured that all pp collisions are at the same center of mass energy as the PbPb collisions they will be compared to, $\sqrt{s_{NN}} = 2.76$ TeV. LHC11a data was used, and, as before, the exact run numbers are mentioned in appendix 2.1.1.

Firstly and most obviously, it makes no sense to cut on centrality or event plane scaler product because these terms are almost meaningless in pp collisions. As such, those event level cuts were not applied to the pp sample.

Secondly, it's worth noting that the LHC11a data set contains roughly the same number of events as LHC11h data, but pp particle multiplicity is on average roughly two orders of magnitude smaller than PbPb the actual number of identified inclusive photons will be much smaller as well. This drop in statistics is a significant concern, and sadly it can not be made up for by simply increasing the event count by two orders of magnitude. To date, the LHC has not run much more pp data at 2.76 TeV than the LHC11a set. In addition, the PbPb cuts were intentionally chosen to be quiet strong in order to ensure the highest possible sample purity. In pp collisions, the selection criteria do not need to be so hard - particle identification is generally much easier especially in instances where the TPC is used such as the charged particle veto. Therefore, cluster selection cuts were weakened slightly for the pp data set. The exact cuts are listed below, along with Fig. 4.9 indicating their relative efficiency and purity. It is worth comparing to the list provided in section 2.4.1 above. After these updated cuts were made, the proton-proton inclusive photon spectrum was derived and is shown in Fig. 4.10.

0. Is PHOS = True

1. $N_{cells} \geq 2$

2. $E_{cluster} \geq 0.2$ GeV

3. $-100 \leq TOF \leq 100$ ns

4. $d_{NearestBadChannel} \geq 2.2$ cm

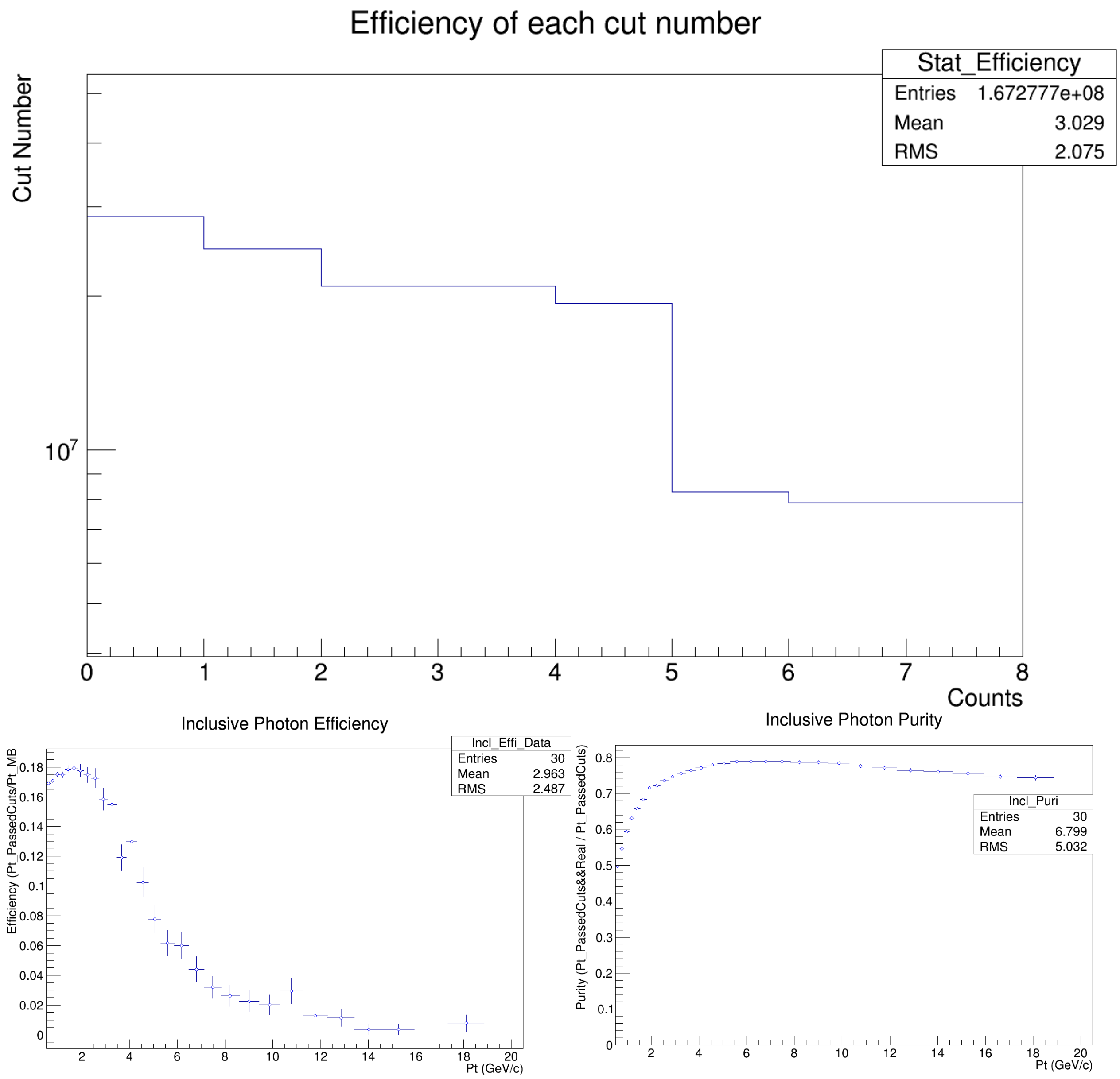

Figure 4.9. pp efficiency of each cut number (top), total efficiency by bin (bottom left), and total purity by bin (bottom right).

5. CPV (see 2.2)

6. Cluster Shape (see 2.3)

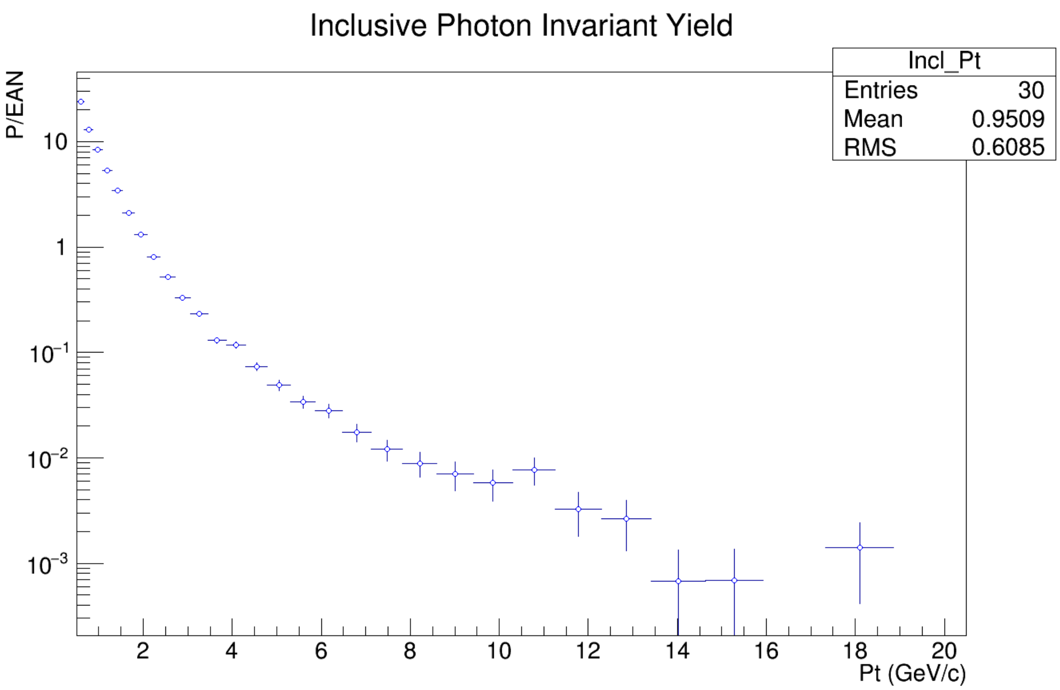

Figure 4.10. pp Inclusive photon spectrum.

And finally, the PbPb neutral meson exclusion mixed event method which bins like events in centrality, event plane, a z-vertex is no longer needed since centrality and event place have no meaning in pp events. As a result, no separate binning for like events was used (the z-vertex was already collapsed to a single bin as discussed in section 2.4.1). The other procedures for extracting the neutral pion spectrum remained unchanged.

4.3.3 Proton-Proton Double Ratio and Direct Photon Spectrum

From here, the same procedure was performed in HIJING as mentioned in section 4.1. Monte Carlo data set 15d3b was used. This Monte Carlo was generated with Pythia 8, LHC13g anchors, pp $\sqrt{s_{NN}} = 2.76$ TeV. The exact run numbers are available in appendix 2.1.1. It is worth noting the (relatively) low statistics of this pp MC simulation. Simply not that many data sets were ever produced; and this is confounded again by the limited cut efficiency of pp. Once again, the relaxed cut set was used for this data set mentioned in section 4.3.2. A pp double ratio was computed and is seen in Fig. 4.11.

The shape of the pp double ration is notably similar to the PbPb double ratio, excepting the larger statistical error bars, of course. We will see if the translates to a suppression factor. In any case, the pp Direct photon spectrum is computed in Fig. 4.12.

4.4 Suppression Results

4.4.1 Average Participating Nucleons

A careful reader has already noticed significantly different photon and pion yield in PbPb collisions by comparison to pp collisions; this is quiet intuitive: greater initial participating nucleons yields correspondingly greater product hadrons in an event. But as discussed briefly in section 4.3.1, this effect means it will be necessary to scale

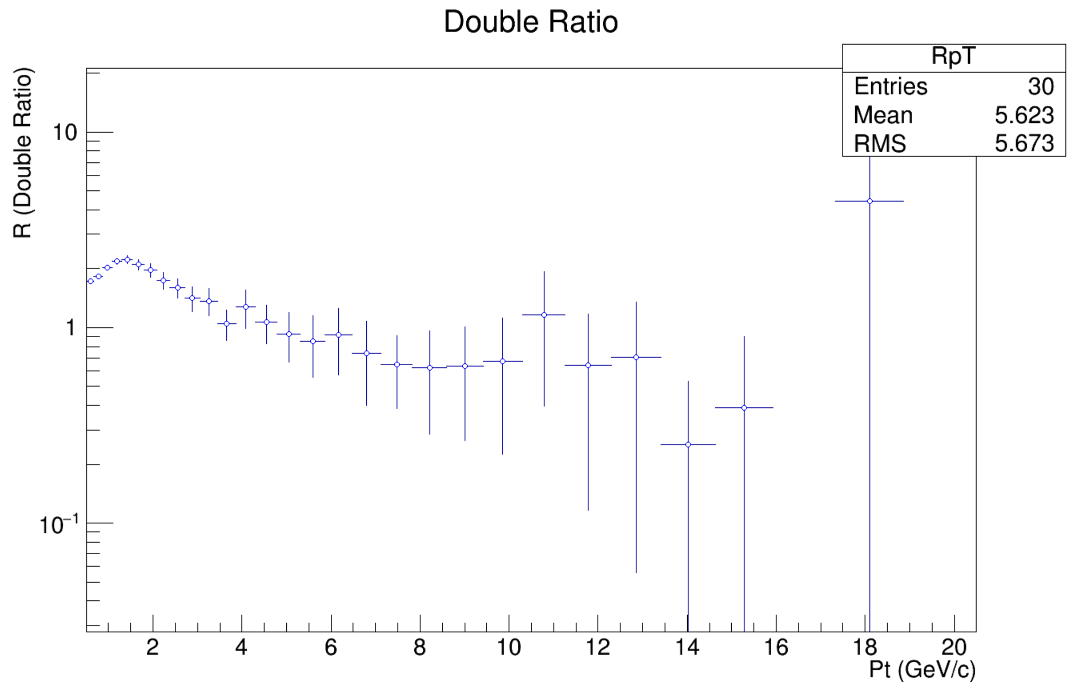

Figure 4.11. pp double ratio.

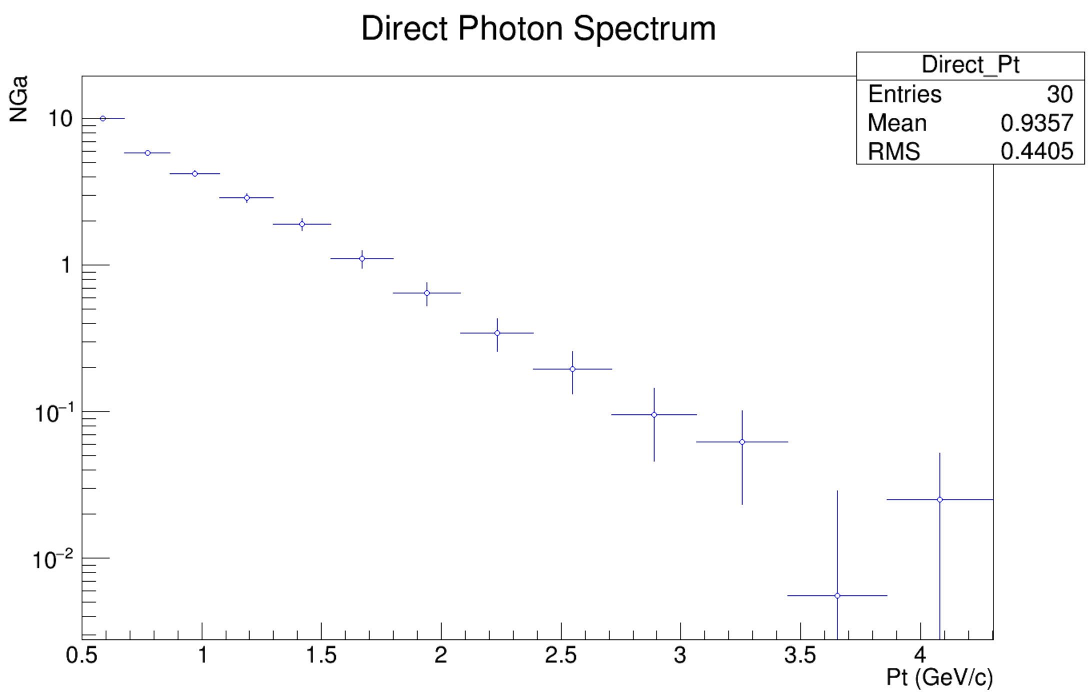

Figure 4.12. pp direct photon spectrum.

down PbPb yields to compare to pp results. This scaling factor is given by Glauber as the nuclear overlap function, $\langle T_{AB} \rangle$. In the Glauber model's optical limit, this can be understood as the approximate number of interacting nucleons in collision as given by the convolution of the two overlapping circles in the collision profile (that is, the overlapping circles in Fig. 1.5). This has been computed before [48], and is given mathematically by:

$$\langle T_{AB} \rangle \equiv \frac{\int d^2b * T_{AB}}{\int d^2b} = \frac{AB}{\pi(R_A + R_B)^2} = \frac{AB}{\sigma_{AB}^{geo}} \tag{4.6}$$

where σ_{AB}^{geo} is the geometrical nuclei cross section and A and B are simply the number of nucleons in each nucleus. In the case of PbPb collisions, A = B = Pb = 208. σ_{AB}^{geo} itself is a function of σ_{NN}, the inclusive inelastic nucleon - nucleon cross section and the overlap function.

$$\sigma_{AB}^{geo} = \iint d^2b \left[1 - e^{-\sigma_{NN}(s)*T_{AB}(b)}\right] \tag{4.7}$$

σ_{NN} has been calculated in pp at $\sqrt{s} = 2.76$ TeV [49, 50] to be roughly:

$$\sigma_{NN} = 62.8mb \tag{4.8}$$

This gives,

$$\sigma_{PbPb}^{geo} = 7.64b \tag{4.9}$$

And,

$$\langle T_{AB} \rangle = \frac{AB}{\sigma_{AB}^{geo}} = 5.66mb^{-1} = 56.6fm^{-2} \tag{4.10}$$

It is worth noting that centrality intervals in ALICE are defined in part using this factor [50]. Using this method, $\langle T_{AB} \rangle == 5.66mb^{-1}$ corresponds to a centrality value of 30-35%. When comparing to centrality dependent results such as those present in many flow measurements [74], we will naively use this centrality bin.

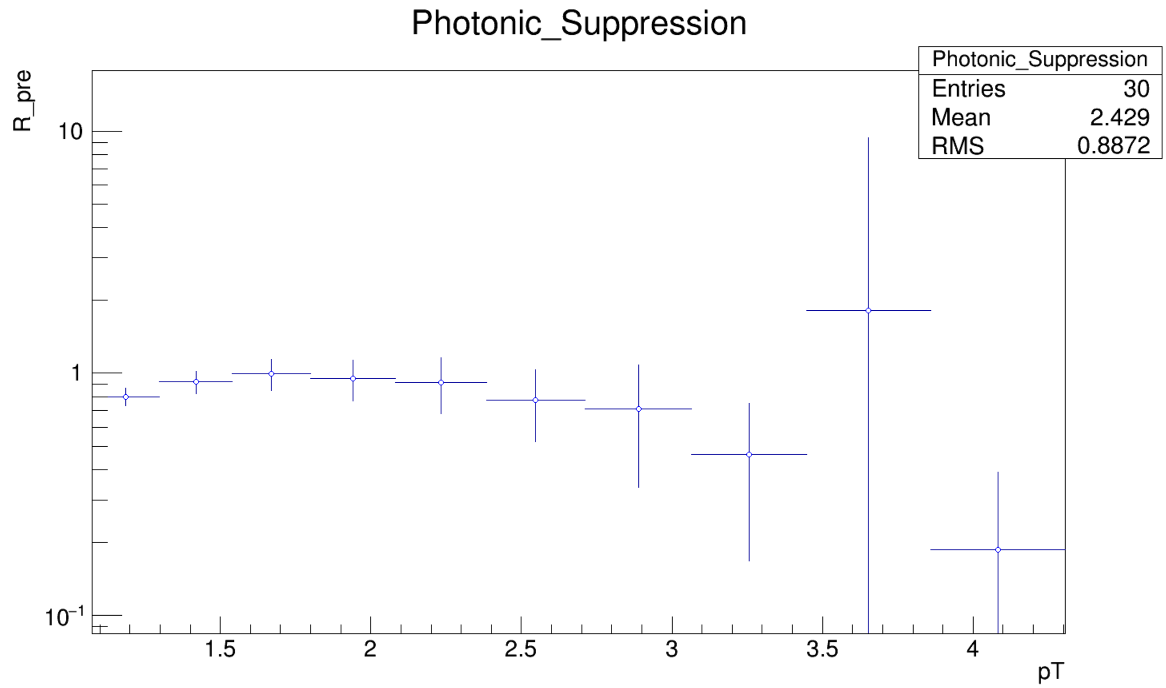

Figure 4.13. Direct photon nuclear suppression factor for PbPb collisions at $\sqrt{s_{NN}} = 2.76$ TeV.

4.4.2 Suppression Results

With the required pp and PbPb direct photon spectrum, as well as the proper normalization factor supplied by Glauber, we now compute the nuclear suppression factor for direct photons as detailed in section 1.4.2, using formula:

$$R_{AA}(p_t) = \frac{dN_{AA}^{total}/dp_t}{\langle T_{AA}\rangle \, d\sigma_{pp}^{pQCD}/dp_t} \tag{4.11}$$

The resulting thermal photon suppression is consistent with one in all centrality bins. In other words, no significant suppression can be detected by the analysis. It appears that thermal photons are like their high energy siblings, jet-medium and prompt photons, and are not absorbed as they traverse the QGP medium.

5. AZIMUTHAL ANISOTROPY

5.1 Event Plane

5.1.1 The Physics of the Event Plane

As discussed previously (1.1.2), the physics of heavy ion collisions is largely described by the Glauber model. In the Glauber model, it's possible to define a nuclear impact parameter ($\vec{b} = \left|\vec{b}\right| \hat{b}$) which describes the displacement vector between the center of the nuclei (as defined by the parton probability density functions in coordinate space) in the transverse plane. The Glauber model allows determination of $\left|\vec{b}\right|$(see again Fig. 1.3) using the total particle multiplicity of the final state, which we understand to be simple the centrality class. However, knowing the orientation of $\vec{b}$ is also critical; especially in discussions of flow. It is possible to determine $\hat{b}$ by observing the pattern of noninteracting observer radiation (see section 5.1.2) along the beam line. This task is performed by the V_0 detector in ALICE (see section 1.2.3 for details of the V_0 detector).

Presently the LHC can focus a PP beam into a cross sectional area of about $64\mu m$ at the collision vertex [54]. Since the cross sectional area of a heavy ion is about $5.78 \begin{array}{c} +0.16 \\ -0.18 \end{array} fm$ [55], the $\vec{b}$ of any given heavy ion collision in the lab is effectively randomly determined. The Glauber model states that $\left|\vec{b}\right|$is not uniformly random; indeed, peripheral events are much more common as one might intuitively expect (you would have to be pretty lucky to have two ions hit "head on"). However, it can be reasonably expected that $\hat{b}$ *is* uniformly random. Specifically, if the angle between an event's $\hat{b}$ with respect to an arbitrary (but consistent between events) direction is described with θ_{RP}, it is expected to be uniformly distributed between zero and 2π. This θ_{RP} is simply the "reaction plane".

It is worth noting that although the domain of θ_{RP} is strictly $[0, 2\pi)$, the physics of a heavy ion collision exhibits bilateral symmetry. As such, any θ_{RP} is physically indistinguishable in a phase shift of exactly π. In other words, $\theta_{RP} = \theta_{RP} + \pi$ describe the same physics. Because of that, the domain$[0, 2\pi)$ can be reduced to $[0, \pi)$ because $[\pi, 2\pi)$ will demonstrate identical physics.

Of course, knowing with certainty the reaction plane for any given event is far beyond present technical abilities. But it is possible to estimate it using existing detectors [15]. The estimated reaction plane using experimental observation is the event plane, θ_{EP}. θ_{EP} demonstrates the same properties mentioned earlier in the event plane, but with the added difficulty of statistical and systematic uncertainty in the measurement. Using statistical methods, those uncertainties can then be incorporated and corrected for using a deeper analysis, which will be discussed in 5.1.2.

5.1.2 Event Plane Determination

A technical breakdown of the V_0 detector can be found in 1.2.3. For our purposes, it is enough to know that in the ALICE experiment, there are three measurements of event plane: two using the V_0 detector on each side of the experiment (the "A" and "C" side - A is on the south side of the detector along the beam line) and one using the TPC. The V_0 method searches for radiation spray along the beam line from liberated non interacting observer nucleons present in the initial collision. The TPC method looks for anisotropy in the charged particle tracks in the TPC. For comparison with previous studies, only the V_0 method was considered in this analysis.

For each event, the V_{0A} and V_{0C} measurements were both computed in post analysis reconstruction. These values were then rotated by $\pm n\pi$ (where n is a positive integer) until they lied in the relevant domain, $[0, \pi)$. The mean of the two measurements where computed (shown in Fig. 5.1). While θ^A_{EP} and θ^C_{EP} are both uniformly distributed (Fig. 5.1 - left) as expected, it can be observed that the mean of the measurements - θ^{AC}_{EP} - is not a good way to estimate the true reaction plane, because

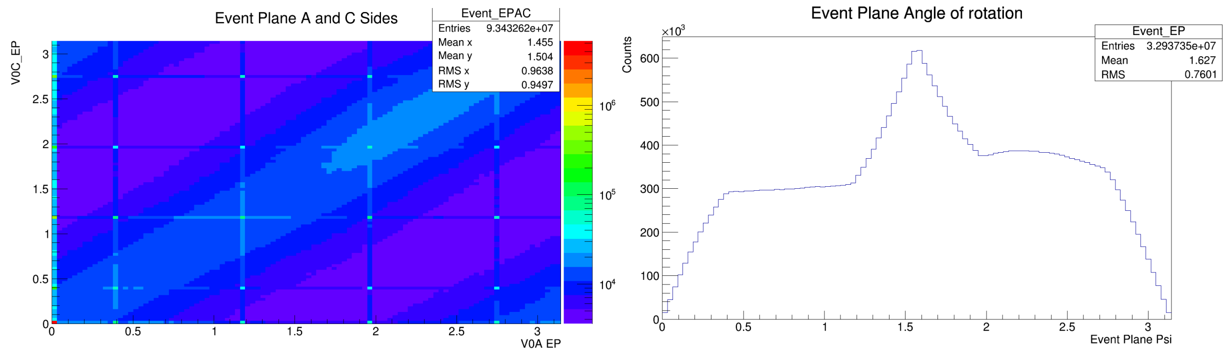

Figure 5.1. V0A vs V0C (left). Average A and C side event plane (right).

it is not uniform. This is because in cases that $\theta^A_{EP} \approx \theta^C_{EP} \approx 0$ and such that $\theta^A_{EP} > 0$ and $\theta^C_{EP} < 0$ (or vice versa), the θ^C_{EP} measurement will be rotated to $\theta^C_{EP} \approx \pi$ to fall in the relevant domain, but θ^A_{EP} will not. The result is an average of $\theta^{AC}_{EP} \approx \frac{\pi}{2}$, which is, of course, entirely wrong. The net effect is an overpopulation of θ^{AC}_{EP} around $\frac{\pi}{2}$ and an underpopulation near 0. Therefore, naively averaging the two measurements is an improper way to attempt to find the two event planes. Note that something similar to this effect is present even before rotation since there's no guarantee that the detectors will agree on the proper $n\pi$ phase shift during reconstruction. Instead, each flow measurement that follows is done independently on both the A and C side. Then it is the flow measurements, not the event planes themselves, which are averaged to compute the "final" flow results.

The scaler product of the A and C event planes (or, more specifcally $\left|\cos(\theta^A_{EP} - \theta^C_{EP})\right|$) was also computed and can be seen in Fig. 2.4. This provides a good check to see how the A and C side event planes agree (if at all). A global cut on events with $\left|\cos(\theta^A_{EP} - \theta^C_{EP})\right| < 0.7$ was applied to eliminate possible bias from inconsistent reporting of the event plane.

5.2 Discussion of Flow

5.2.1 Methods to Compute Flow

The azimuthal coordinate phase space anisotropy in the particle yield of a heavy ion collision is mathematically characterized as [83]:

$$\frac{2\pi}{N}\frac{dP}{d\theta_\gamma} = 1 + 2\sum_{n=1}^{\infty} v_n \cos n(\theta_\gamma - \psi_{EP}) \tag{5.1}$$

where $\frac{dP}{d\theta_\gamma}$ is the true azimuthal probability density of the emitted particle. However, the true azimuthal probability density function is not generally known.

The naive solution is to employ the law of large numbers and simply substitute $\frac{dP}{d\theta_\gamma}$ with $\frac{dN}{d\theta_\gamma}$, the observed particle azimuthal distribution, under the assumption that observed particle distribution will trend toward the probability density function sufficiently to simulate it. This is often called the Event Plane Method, because it depends heavily on the accuracy of the event plane reconstruction. However, this has some problems. Principally, while the average flow measured with the event plane method, $\langle v_n \rangle_{EP}$, does indeed tend toward the measured value, its root-mean-square depends heavily on the measurement of ψ_{EP} as mentioned, which, in turn, depends heavily on the experimental set up. Therefore, different experiment's $\langle v_n \rangle_{EP}$ measurements converge to the real value at different rates. This makes reproducing $\langle v_n \rangle_{EP}$ measurements difficult in different experiments. This additional uncertainty in the measurement can be on the order of several percentage points, and confounds comparison of different harmonics [37].

An alternative solution is the Scaler Product Method, $\langle v_n \rangle_{SP}$, which instead correlates multiple sub events divided by an azimuthal flow independent quantity - usually pseudo-rapidity - using their flow vectors, $\overrightarrow{Q_n}$. This gives the formulation:

$$\langle v_n \rangle_{SP} = \frac{\left\langle Q_n \frac{Q^*_{nA}}{|Q_{nA}|} \right\rangle}{\sqrt{\left\langle \frac{Q_{nA}}{|Q_{nA}|} \frac{Q^*_{nB}}{|Q_{nB}|} \right\rangle}} \tag{5.2}$$

Where Q_{nA} and Q_{nB} are the flow vectors of different sub events. While both methods yield the same $\langle v_n \rangle$ in the limit of large statistics, the scaler product method is said to reduce systematic by a few percent in v_2 and up to 10% in higher order [37].

In this analysis, v_n^{dir} is a composite measurement - depending on both v_n^{incl} and v_n^{dec} (see appendix A). v_n^{dec} is imported from a a charged pion study which used the scaler product method (section 5.2.3). By contrast v_n^{incl} was studied using the event plane method. The motivation for this decision is related to the psuedorapidity acceptance of the PHOS detector, $|\eta| \leq 0.12$, as well as the certain dead half modules in the LHC 11h data set (see Fig. 2.8). It's possible that asymmetry in the particle yield in psuedo rapidity due to the dead half modules might increase the uncertainty in the $\langle v_n \rangle_{SP}$ measurement. Since the improvement in the error of the scaler product method over the event place method is already marginal, and employing the scaler product method would require a nontrivial amount of additional computing time, it was decided to use the simpler scaler product method for a first look at these quantities.

5.2.2 Inclusive Photon Flow

Since the PHOS detector's three modules cover an azimuthal range of about $(0.5 - 20 \text{ GeV})$ where $\theta = 0$ is defined in the ALICE coordinate system, each cluster's location in the global coordinate system also falls in that range. The location of each cluster is taken to be a single point at the cluster's center. The center is algorithmically computed during reconstruction and is defined as the unfolded weighted center of the cluster [60]. After appropriate cuts (section 2.1), the remaining photon candidate cluster locations are subtracted from the event plane (computed using the method in section 5.1.2). $d\theta = \theta_\gamma - \theta_{EP}$ The result is then rotated by $\pm n\pi$ where n is a positive integer in order to be consistent with the same phase domain $[0, \pi]$.

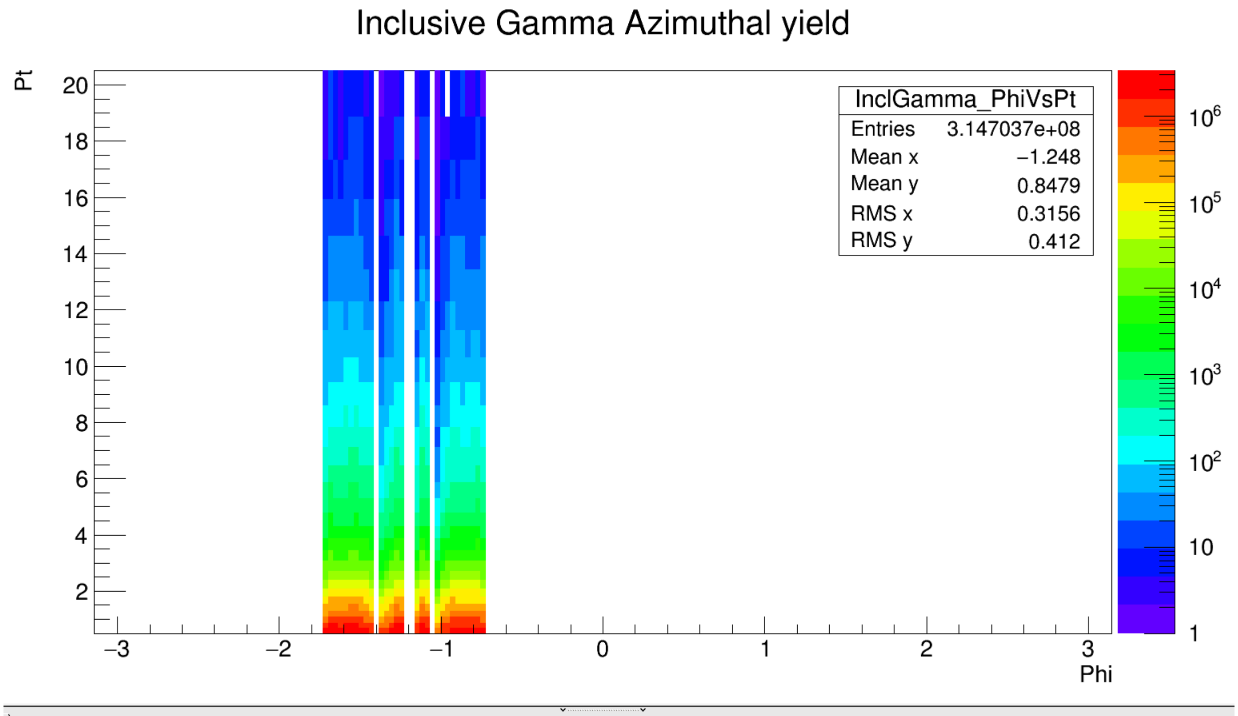

Figure 5.2. θ_γ in the ALICE global coordinate system. Note the acceptance of PHOS.

The resulting $d\theta = \theta_\gamma - \theta_{EP} \pm n\pi$ is plotted with respect to centrality and p_t in Fig. 5.3. A clear sinusoid pattern can be observed even in central events. This sinusoid is already indicative of inclusive photon v_2.

Each p_t bin is projected in $d\theta$ to create plots similar to 5.4. Each plot is then fit to the function:

$$\frac{\delta N_{incl}}{\delta \theta} = v_0^{incl} \left[1 + 2 \sum_{n=1}^{6} v_n^{incl} \cos(nd\theta + \psi) \right] \tag{5.3}$$

where v_n^{incl} are the relevant inclusive flow coefficients and ψ is a universal phase shift coefficient. Note that it's perfectly possible the apparent phase of the best fit to be shifted by $\frac{\pi}{2}$, especially if the V0 detector is slightly misaligned or simply due to statistical fluctuations in the measurement. This can make measurements of the flow in side by side p_t bins to reflect randomly about the x-axis. By introducing

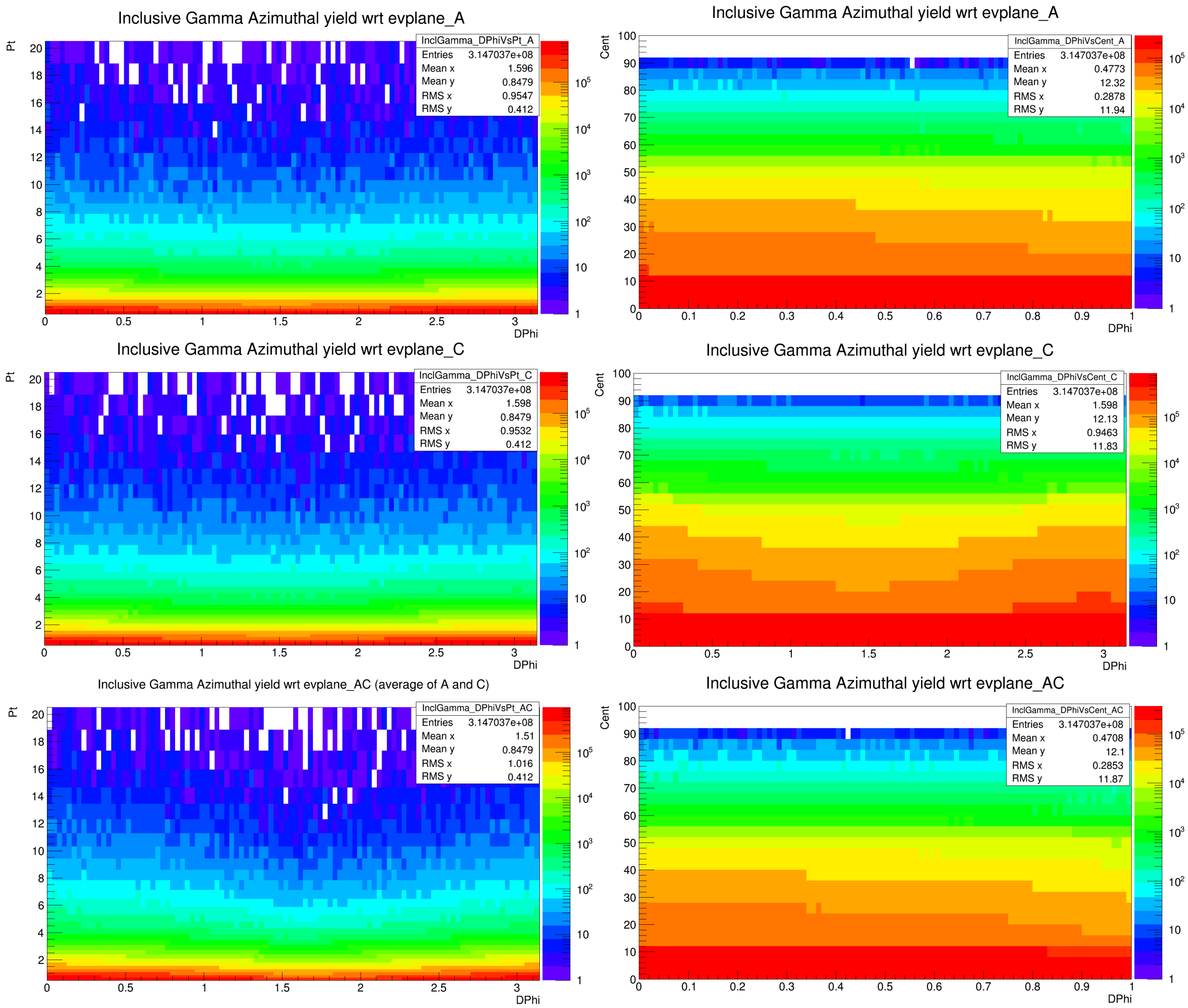

Figure 5.3. $d\theta$ distribution on A side (top), C side (center), and averaged A and C (bottom). By row, the event plane is distributed with respect to p_t (left) and centrality (right).

the universal phase shift in each term, this effect is effectively eliminated, but still possible in principal (especially in very low multiplicity bins).

The fit was taken to the sixth harmonic because published charged pion results [74] go to the fifth harmonic (see section 5.2.3 to understand the relevance of this). An extra order was provided to allow an additional degree of freedom to account for statistical noise.

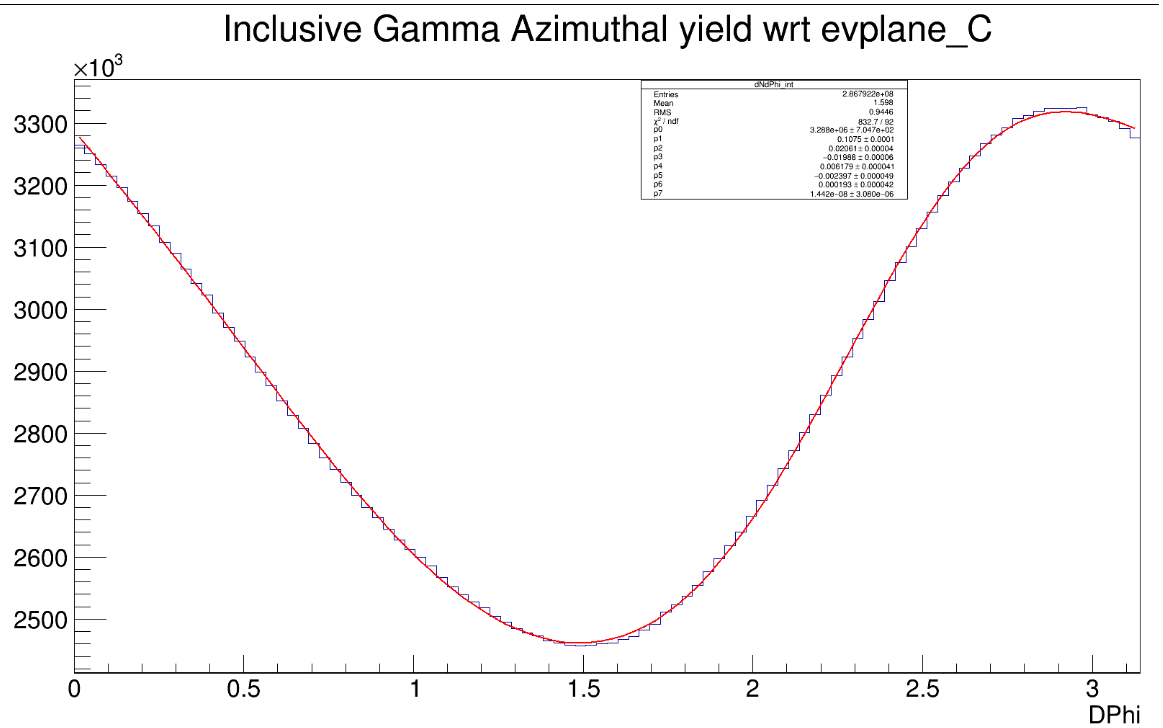

Figure 5.4. $d\theta_C$ integrated on all p_t bin and fitted using Eq. 31.

Each p_t bin of figure 5.3 is projected onto it's $d\theta$ axis to create a profile plot similar to 5.4 which is then fit using eq 31. The resulting parameter values are then plotted in Figs. 5.5 and 5.6, and the mean of the results of the A and C side in 5.7. Flow parameters could be reflected about the x-axis if inconsistent phase shifts were used for each fit, so some tuning of initial fitting parameters and parameter limits was performed to ensure that each fit had a uniform phase shift.

5.2.3 Decay Photon Flow

Unlike inclusive photons which are simple enough to measure, the decay photons are nontrivially difficult to observe with accuracy. Previous attempts to measure the spectrum have led to some success [78], and the azimuthal anisotropy of certain particle species such as the neutral pion have been observed as well [84]. However,

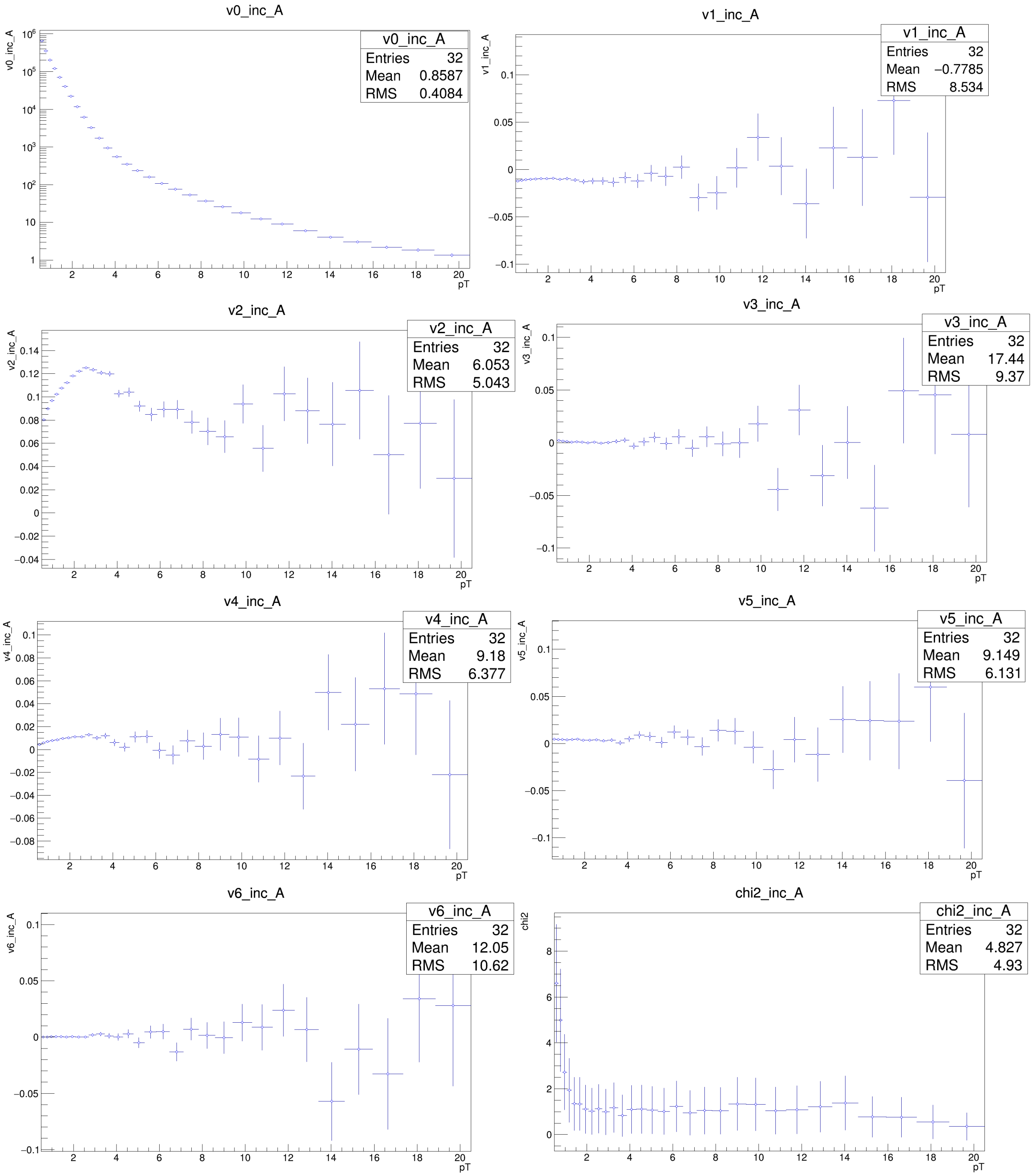

Figure 5.5. A-side Inclusive Flow coefficients in v_0 through v_6 as well as the fit chi square.

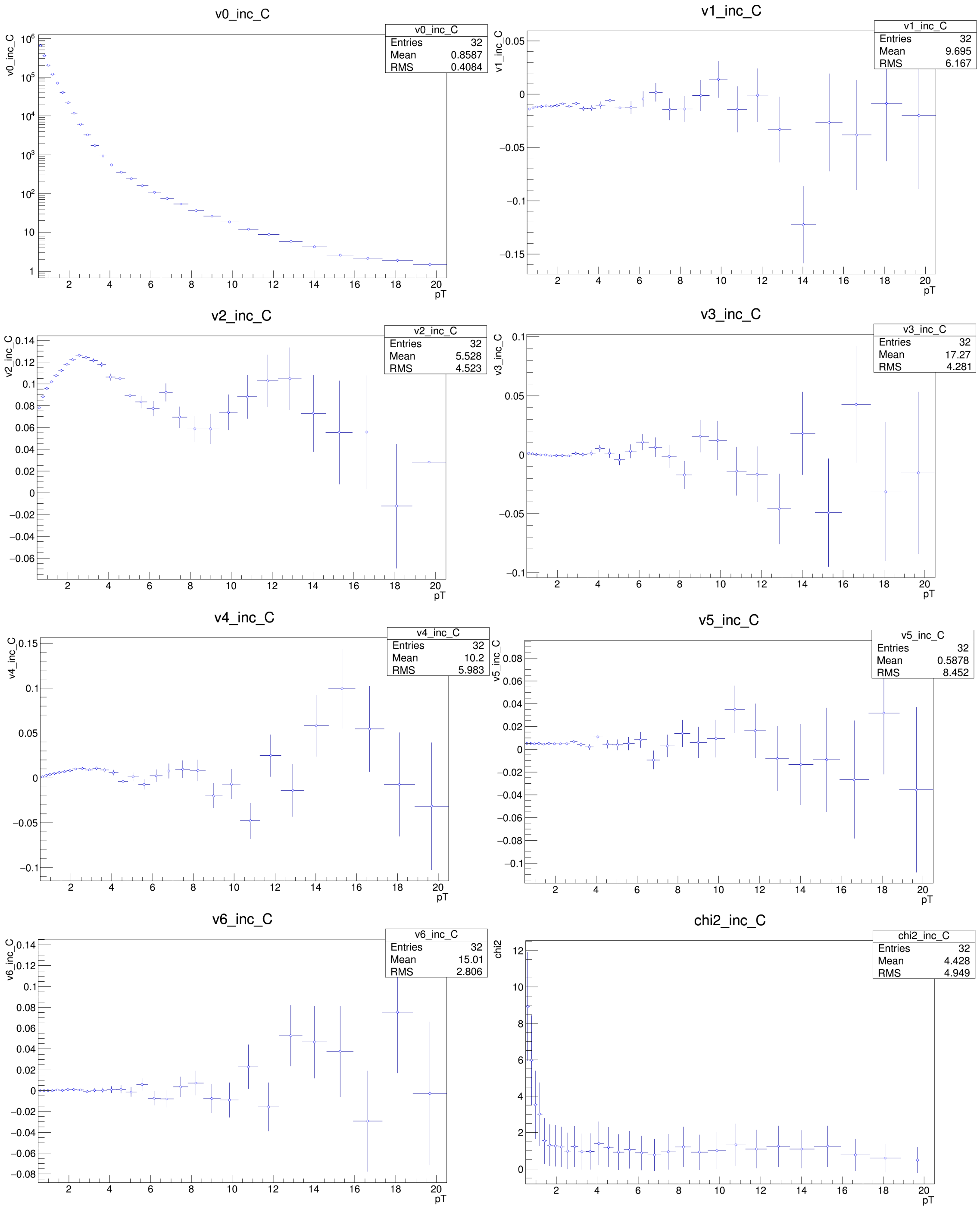

Figure 5.6. C-side Inclusive Flow coefficients in v_0 through v_6 as well as the fit chi square.

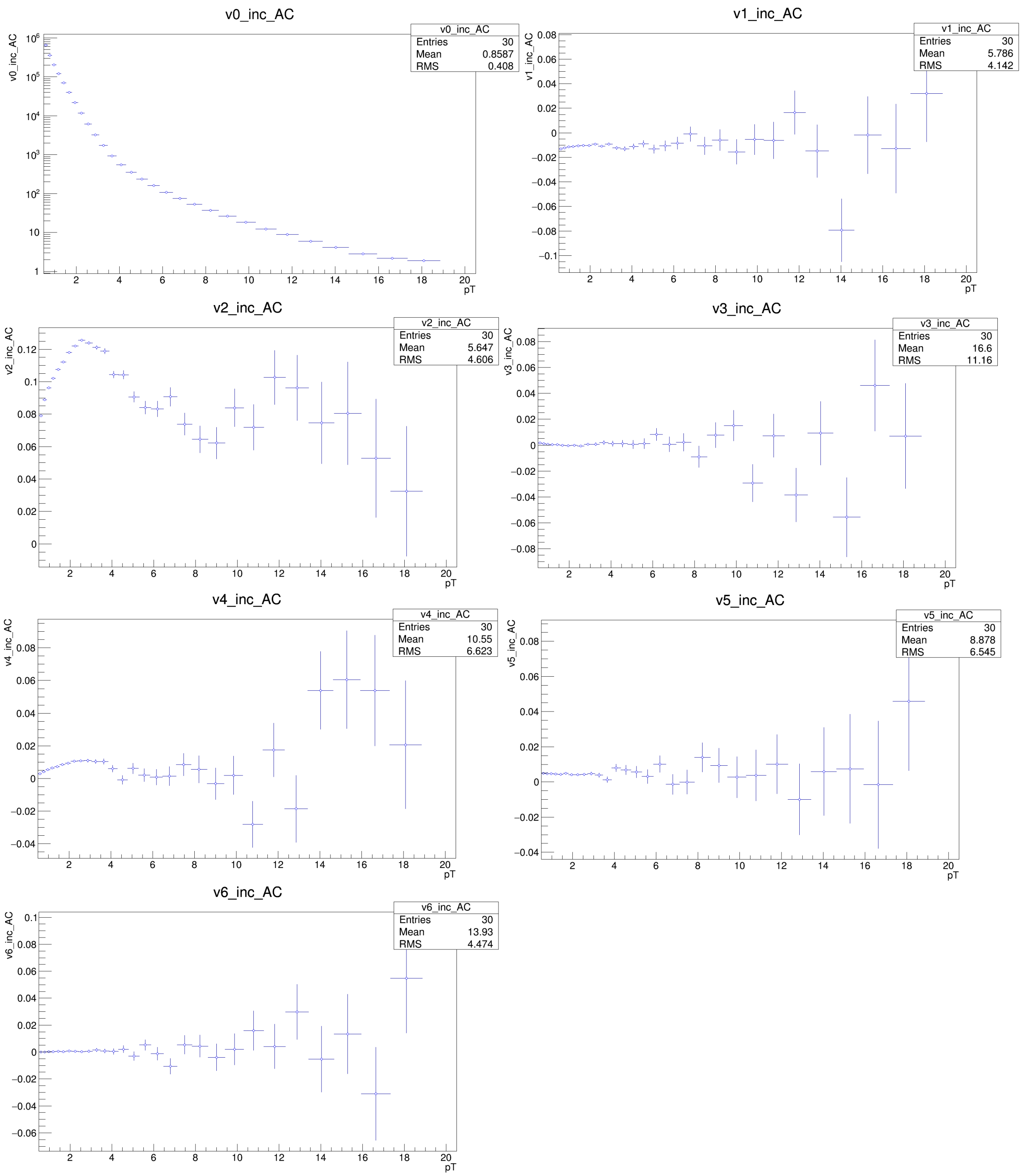

Figure 5.7. A and C averaged Inclusive Flow coefficients in v_0 through v_6 as well as the fit chi square.

in general these analysis are very complex and have large uncertainties. Therefore, using the same methods to isolate decay photons and then compute the decay photon anisotropy is not feasible. It would be beyond the scope of this analysis to attempt to explicitly compute the decay photon anisotropy. Further, if we used these sophisticated methods, the associated error once one takes into account the limited PHOS acceptance would make the final errors in the direct photon flow to make the results effectively meaningless. Therefore, no analysis was done to directly compute decay photon flow.

However, by far the primary source of decay photons is neutral pions, and it is observed that neutral pion anisotropy very closely mirrors charged pion anisotropy, which is far easier to measure and has already been done by previous analysis with great accuracy [74]. Theoretically, this is easy to justify: we postulate that light partons fragment equally often into both charged and neutral pions. Therefore, it is suggested that the initial hadron azimuthal distribution can be parameterized with the measured charged pion distribution [85]:

$$\left[v_N^{\gamma;decay}\right]_{MC} = \left[v_N^{\pi^0}\right]_{MC} = \left[v_N^{\pi^{\pm}}\right]_{MC} \tag{5.4}$$

The result from this previous analysis is in the p_t range $(0.5 - 5.5$ GeV) (the thermal regime!), and in centrality 20-30% and 30-40% up to the fifth harmonic and are transcribed below (Fig. 5.8). Note that these results were computed using the scalar product method discussed in section 5.2.1. In order to match the p_t binning of the inclusive photon flow and double ratio studies (section 2.4.3 and 4.2), the charged pion flow was fit using a fourth order polynomial and interpolated to give specific values in the appropriate bins:

$$v_N^{\pi^{\pm}}(p_t) = A + Bp_t + Cp_t^2 + Dp_t^3 + Ep_t^4 \tag{5.5}$$

Where A, B, C, D, and E are free parameters. The results have good χ^2 and are shown in Fig. 5.9. These values are then used in subsequent computations to compute the direct photon flow.

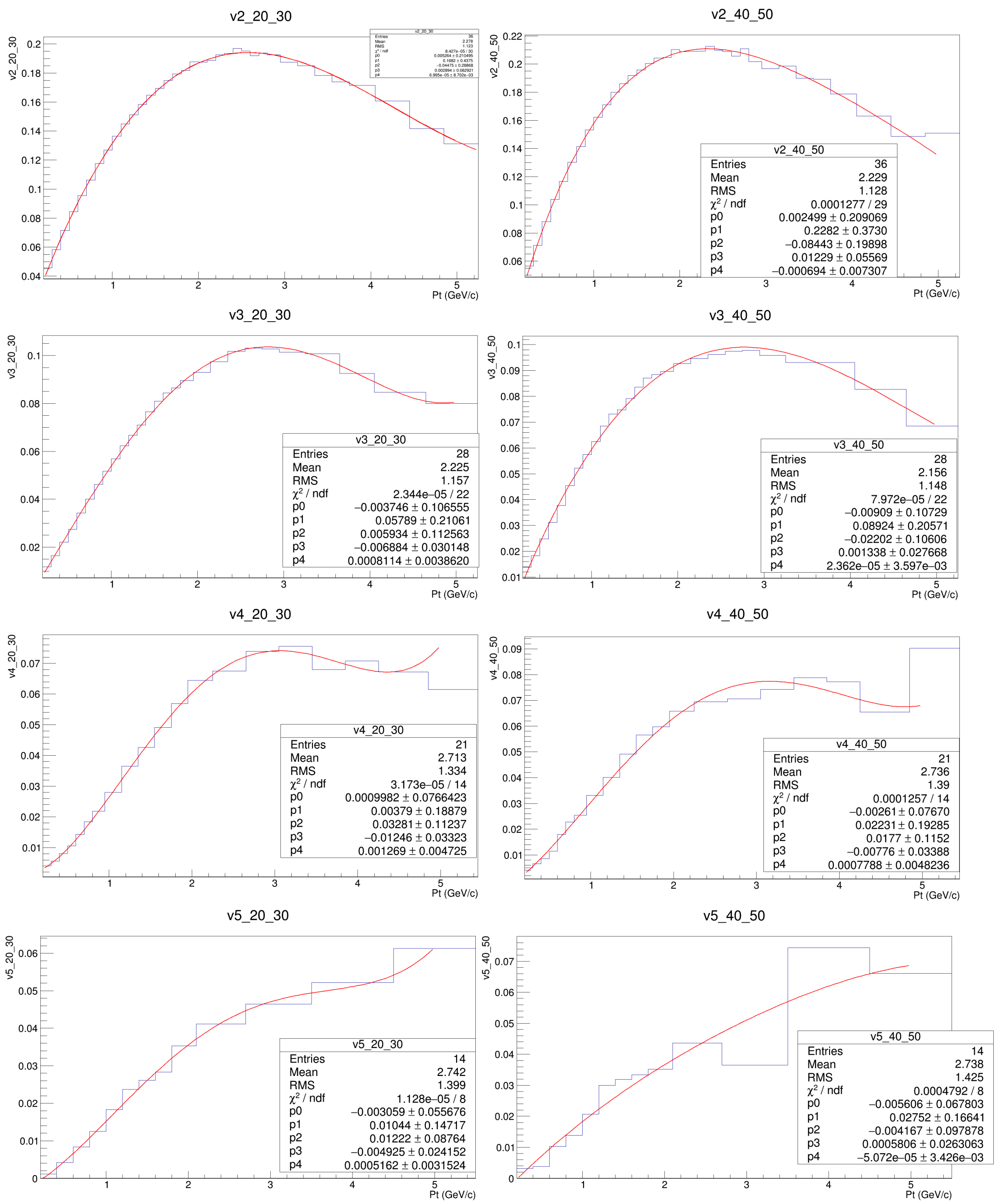

Figure 5.8. Fit of $v_N^{\pi^\pm}(p_t)$ results to rebin histogram. Charged pion data points were computed in a different analysis. [74]

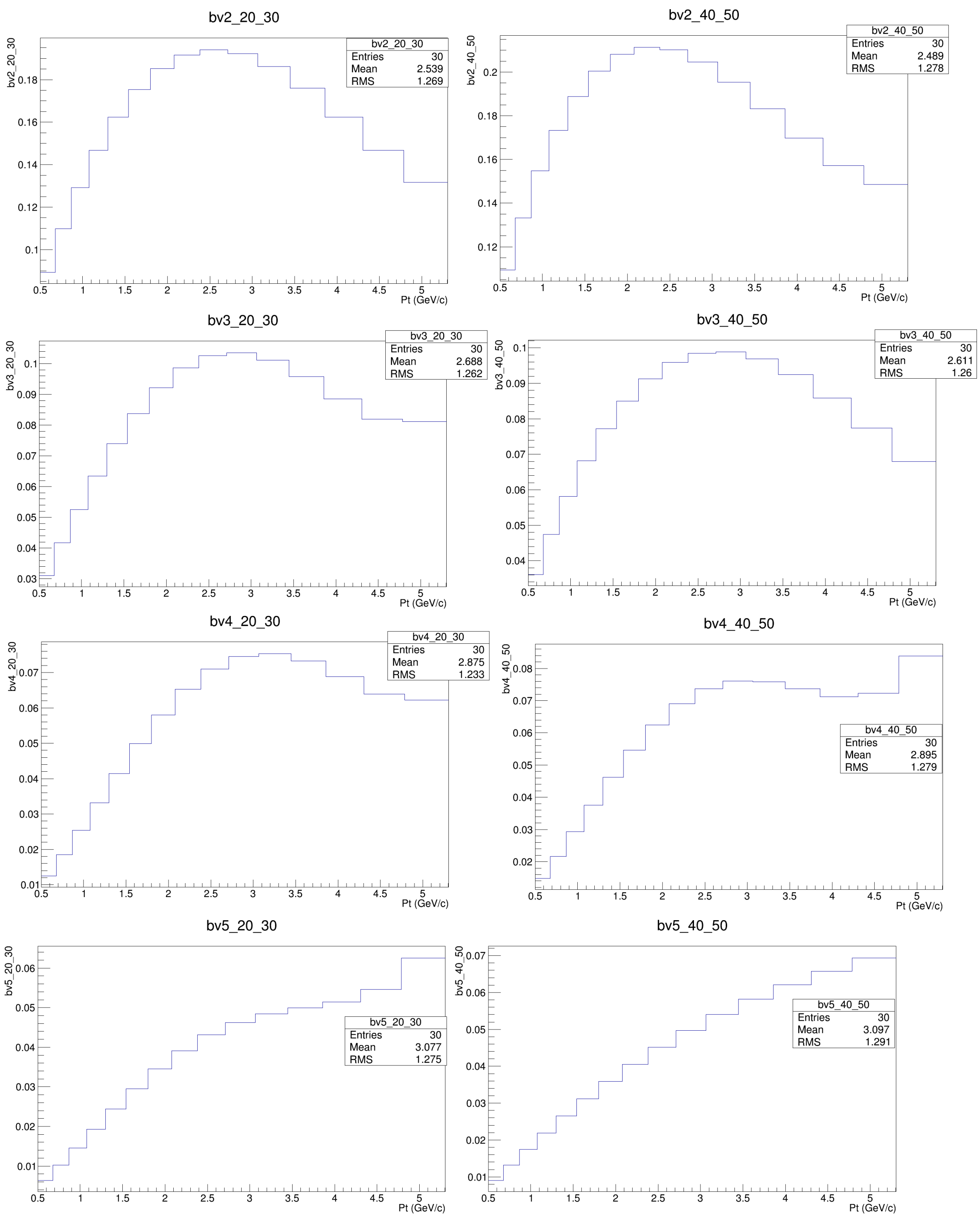

Figure 5.9. Charged Pion flow coefficients in v_2 through v_5 [74] fitted and rebinned for comparison to inclusive flow. Left column is 20-30% centrality. Right column is 40-50% centrality.

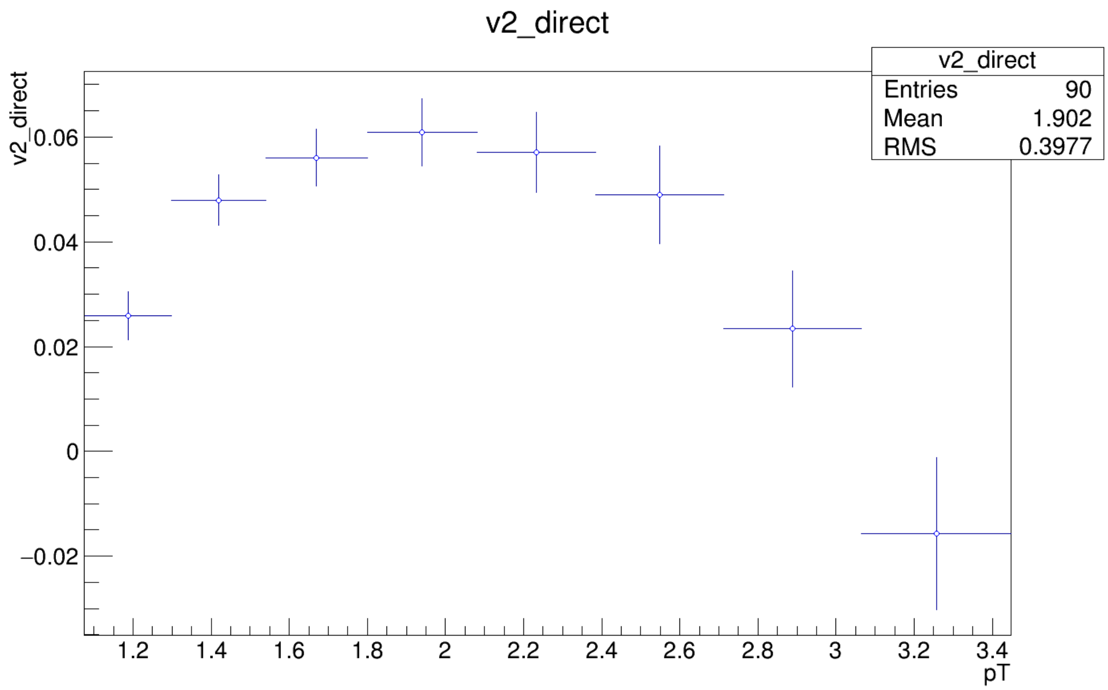

Figure 5.10. Calculated direct photon flow v_2

5.3 Direct Photon Flow Results and Interpretation

5.3.1 Direct Photon Flow

Using the formulation discussed in appendix A:

$$v_n^{dir} \approx \frac{Rv_n^{inc} - v_n^{dec}}{R-1} \tag{5.6}$$

Where R was obtained in section 4.2.1, v_2^{inc} was obtained in section 2.4.3, and v_2^{dec} was obtained in section 5.2.3. v_2^{dir} was therefore computed up to the fifth harmonic in the transverse momentum range $(0.5 - 5.5$ GeV$)$ (where v_2^{dec} is the limiting domain). The results of the computation can be seen in Fig. 5.10.

One can observe that the direct photon v_2 peaks at a value of $v_2^{dir} \sim 0.06$, depending on the p_t bin. This is also consistent with previous results at ALICE [85]. However computing higher order flow parameters presents an immediate problem:

$v_{n>2}^{incl}$ is either very small or zero in every bin! $v_{n>2}^{dec}$ shrinks as well, but as these two quantities (and the difference between them) get smaller, statistical uncertainty becomes too great to effectively measure v_n^{dir}. It appears that if $v_{n>2}^{dir} > 0$, then it is too small to detect using this simple method.

5.3.2 Interpretation of Direct Photon Flow

Now that the direct photon flow is computed, we can compare to hadrons. In Fig. 5.11, one can see a summary of both light and heavy flavor elliptic flow results from the ALICE experiment at $\sqrt{s} = 2.76$ TeV.

Direct photon elliptical flow appears much weaker than both light and heavy flavor hadrons. Furthermore, as discussed in section 5.3.1, high order flow in direct photons is weaker still if it exists at all.

This might not be surprising, considering the fact that no significant photonic suppression was observed in section 4.4.2. If flow is caused by relative pressure differentials in the reaction plane (due to the “almond” asymmetry of the nuclear overlap area in Glauber) [86], and one assumes that that “pressure” is due to particle rescattering and attenuation as it traverses the medium; then of course a particle with a high mean free path in the medium (read: a nuclear suppression factor near unity) would show little to no flow compared to particles with a much lower mean free path.

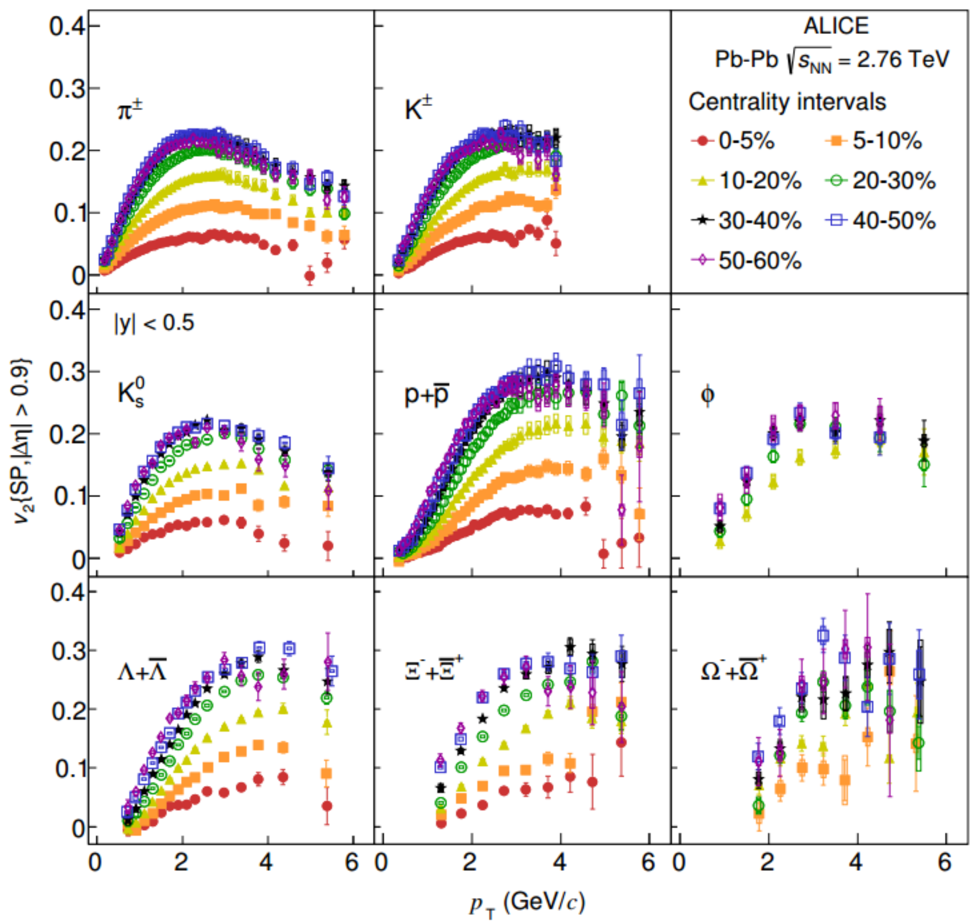

Figure 5.11. Elliptic flow of several major hadrons. [51]

6. CONCLUSIONS

6.1 Review of Findings

6.1.1 Temperature Measurement

Historically, thermodynamic arguments have been used to insist that the inverse slope parameter of the thermal photon spectrum is exactly the thermalization temperature of the activated nuclear plasma in a heavy ion collision [41, 42]. Pursuant to that, the ALICE experiment have gone to great lengths to statistically isolate the thermal photon spectrum [73]. That analysis measured the thermal photon inverse slope parameter of $407 \pm 61^{stat} \pm 96^{sys}$ for 20-40% centrality without pQCD subtraction. This thesis independently measures the thermal photon spectrum and inverse slope parameter, available in Fig. 6.1.

An inverse slope parameter of 459 ± 110 MeV in PbPb at $\sqrt{s_{NN}} = 2.76$ TeV was computed - consistent within error with the previous measurements. It is also possible for the first time to compute the first proton-proton inverse slope parameter measure-

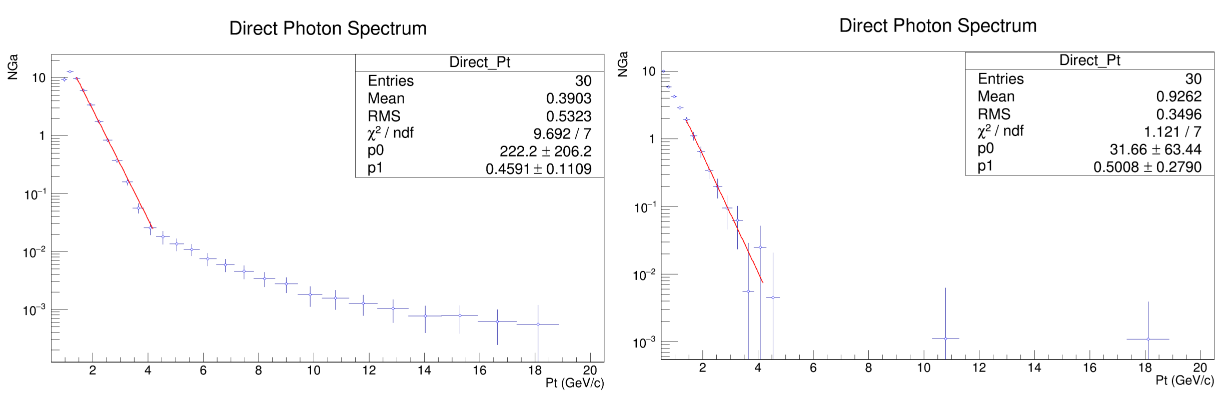

Figure 6.1. Thermal photon spectrum and fit for pp and PbPb.

ment: in pp at $\sqrt{s_{NN}} = 2.76$ TeV an inverse slope of 500 ± 270 MeV is computed. However, the interpretation of the inverse slope parameter has recently become contested [43]. The argument is made that thermal photons are emitted and reabsorbed continuously as they traverse the activated nuclear plasma, and thus might not represent the true thermalization temperature and instead some time weighted average temperature. Indeed, this suggestion is passively (but inconclusively) supported by the observed increase in measured inverse slope parameter with respect to collision energy in RHIC versus the LHC. Therefore, if this assertion is true, then the interpretation of the inverse slope parameter depends heavily on if and when thermalized photons cease interacting with the QGP.

6.1.2 Suppression Summary

In order to interpret the thermal photon inverse slope parameter, it is first necessary to determine if thermal photons are suppressed in the QGP. Previous studies at PHENIX show that hard photons such as those generated by prompt QGP and jet-medium interaction (see section 1.3.4) do indeed traverse the QGP unimpeded [34]. Further, direct photons have historically been considered a privileged probe of the QGP because of their reluctance to interact in the otherwise strongly coupled QGP. However, the PHENIX results do not extend to the thermal photon regime, and particle energy has been known to influence interaction cross section in some particle species [87]. Therefore, this thesis extended the direct photon suppression measurements previously computed by PHENIX into the thermal photon regime in order to directly verify the historical assumption. The results are available in Fig. 6.2.

It can be seen that the thermal photon nuclear suppression factor is consistent with unity; that is, there appears to be no significant suppression. Thus, it is possible that the observed thermal photon spectrum observed at RHIC and LHC and in section 6.1.1 is indeed unperturbed from its moment of emission. Therefore, if the measured thermal photon inverse slope parameter is indeed a time weighted average

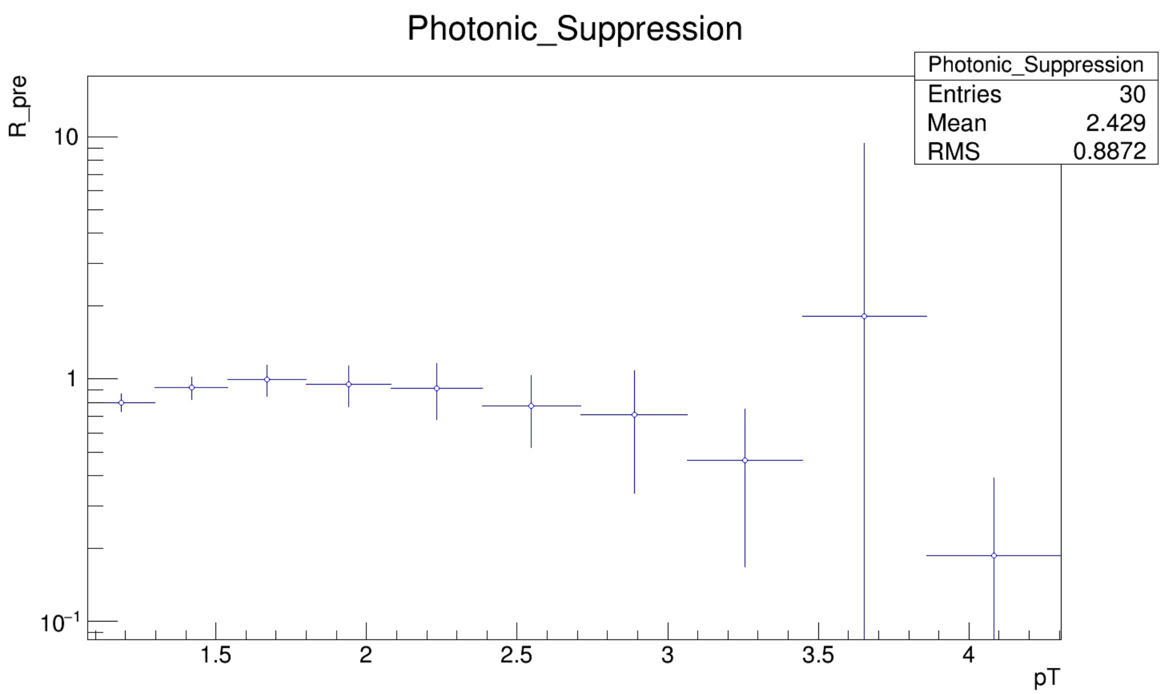

Figure 6.2. Direct photon nuclear suppression factor for PbPb collisions at $\sqrt{s_{NN}} = 2.76$ TeV.

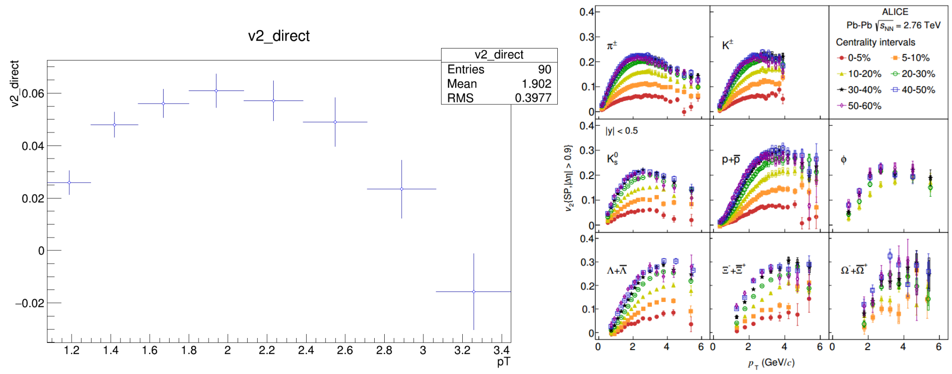

Figure 6.3. Elliptic flow of thermal photons (left). Elliptic flow of other selected particle species [51] (right).

temperature, then it is because those thermal photons were in fact emitted later in the collision and not because of simply rescattering as they traversed the medium.

6.1.3 Direct Photon Flow

In addition to the thermal photon suppression, the measurement of the thermal photon flow provides additional context to help support our conclusions. It was observed that the thermal photon elliptic flow is small compared to both light and heavy hadrons in every p_t bin.

Higher order flow was determined to be too small to measure using the tools available (section 5.3.1 provides a full discussion). This observation is consistent with our thermal photon suppression results: that is, since thermal photons are noninteracting in the medium, the rate of rescattering as a function of azimuthal angle due to the plasma's geometric asymmetry is negligible. It is also consistent with predictions of hydrodynamics [88]. Indeed, the photons observed are mostly unperturbed from their moment of emission. Furthermore, due to momentum conservation, it can also be argued that the thermal photon four momentum distribution will largely mirror the momentum distribution of their parent thermalized partons at their moment of emission. Thus, it can be conjectured that the vanguard of thermal photons are emitted at some time in the collision the when the average four momentum distribution of the plasma is at least locally isotropic.

6.2 Comparison to Theory

6.2.1 Hydrodynamic Model

It is now possible to conjecture about when during the life timeline of the QGP thermal photons are generated in various models. To consider this, one might consider a function, $\frac{d\gamma_{thermal}}{dt}$, the number of generated thermal photons with respect to time during a heavy ion collision. By definition, thermal photons will not be emitted prior to at least local thermalization of the plasma [26]; and even after local thermalization, their population will be limited by the relative proportion of plasma which is locally thermalized to locally unthermalized. By this same line of reasoning, they also may not be emitted after after the last parton has hadronized; $\frac{d\gamma_{thermal}}{dt} = 0$ after chemical freeze out.

During this interim time period, the plasma is expanding and cooling and in principal the vanguard of thermal photons are free to be emitted. However, exact details of this phase are largely unknown, and several narratives exist which one might pursue. Here, we will continue using the hydrodynamic model as we did in section 1.1.3. Once again, we choose to discuss hydrodynamics for no reason other than the fact that hydrodynamics provides a clear picture of the time progression of the plasma. According to the hydrodynamic model partons will strongly interact in the nuclear plasma, and evolve like a fluid - experiencing hydrodynamic shear viscosity and bulk viscosity. Parton shear viscosity accelerates the transverse hydrodynamics expansion, and “for fixed initial conditions, this leads to a longer quark-gluon plasma (QGP) lifetime, larger radial flow in the final state, and flatter transverse momentum spectra for the emitted hadrons compared to ideal fluid dynamic simulations” [52]. Elliptic flow in particular is very sensitive to shear viscosity [53].

If, as hydrodynamics seems to suggest, the thermalized plasma's four momentum distribution is initially locally isotropic and becomes less isotropic as time passes due to the influence of shear viscosity [88], then particles that are immune to shear viscosity will preserve the initial relative isotropy of the system. As we have seen, thermal photons are liberated from these fluid dynamic effects and indeed exhibit low elliptic flow compared to hadrons. Therefore, we are forced to conclude that the results of this analysis are consistent with the predictions of hydrodynamics.

6.3 Implications

6.3.1 Future Considerations

Due to the sensitivity of the thermal photon flow computation, higher order thermal photon flow in a variety centrality bins would require a significantly more sophisticated method which perhaps takes into account more massive diphoton sources as well as secondary diphoton sources. In addition, much higher pp statistics at the same energy as PbPb collisions would be essential for a more precise computation of the photon nuclear suppression factor.

More generally, it is very possible that the thermal photon inverse slope parameter is more strongly coupled to the collision center of mass energy than the thermalization temperature of the QGP. After all, if thermal photons are indeed emitted early in the collision's evolution, one would expect the mean temperature provided by them to increase as the temperature early in the collision increases, and that initial temperature will itself be related to the collision center of mass energy. It would be an interesting task to verify this using a beam energy scan and computing the thermal photon inverse slope parameter at several center of mass energies both at RHIC and the LHC. If the thermal photon inverse slope parameter is closely coupled to the collision center of mass energy, then it would be extremely strong evidence that the observed thermal photons are, indeed, emitted very early in the collision and are more indicative of the maximum temperature of the collision than of the phase transition temperature.

6.3.2 The Time Evolution

We can now provide some answers the open questions proposed in section 1.4. In the hydrodynamic timeline provided in section 1.1.3, we conclude that the peak of thermal photon emission occurs shortly after quark thermalization and before prompt radiation; relatively early in the collision. After peak emission, thermal photons continue to be emitted until chemical freeze out. As thermal photons are emitted, they traverse the quark-gluon plasma mostly unperturbed. As a result, the thermal photon inverse slope parameter measured is not necessarily indicative of the phase transition temperature, but rather a temperature much earlier in the progression of the collision. This result is consistent with the predictions of hydrodynamics [43] with the important extension that the elevated inverse slope parameter is not due to thermal photon rescattering in the plasma, but is instead related to the true thermal photon emission time. We also experimentally verify the long held view [34] that photons - including thermal photons - are a privileged probe of the QGP due to their ability to traverse the plasma unperturbed.

APPENDIX

A. DERIVATION DIRECT PHOTON FLOW

Let

$$\theta = \theta^{\gamma} - \psi^{EP} \tag{A.1}$$

Where θ^{γ} is the azimuthal coordinate of an observed photon cluster, and ψ^{RP} is the measured event plane of the collision.

Now,

$$\frac{\delta N_{direct}}{\delta\theta} \equiv \frac{\delta N_{inc}}{\delta\theta} - \frac{\delta N_{decay}}{\delta\theta} \tag{A.2}$$

$$\frac{\delta N_{direct}}{\delta\theta} = A_{dir}\left[1 + 2\sum_{n\geq 1} v_n^{dir}\cos(n\theta) + s_n^{dir}\sin(n\theta)\right] \tag{A.3}$$

$$\frac{\delta N_{inc}}{\delta\theta} = A_{inc}\left[1 + 2\sum_{m\geq 1} v_m^{inc}\cos(m\theta) s_m^{inc}\sin(m\theta)\right] \tag{A.4}$$

$$\frac{\delta N_{dec}}{\delta\theta} = A_{dec}\left[1 + 2\sum_{l\geq 1} v_l^{dec}\cos(l\theta) + s_l^{dec}\sin(l\theta)\right] \tag{A.5}$$

Where A is just a factor used to normalize the photon distribution $\frac{\delta N}{\delta\theta}$, and v and s are the usual fourier expansion coefficients.

$$\int_{-\pi}^{\pi} \frac{\delta N}{\delta\theta} d\theta = N_{\gamma} = A \tag{A.6}$$

So,

$$A_{dir}\left[1 + 2\sum_{n\geq 1} v_n^{dir}\cos(n\theta) + s_n^{dir}\sin(n\theta)\right] = \tag{A.7}$$

$$A_{inc}\left[1+2\sum_{m\geq 1} v_m^{inc}\cos(m\theta)s_m^{inc}\sin(m\theta)\right] - A_{dec}\left[1+2\sum_{l\geq 1} v_l^{dec}\cos(l\theta)+s_l^{dec}\sin(l\theta)\right] \tag{A.8}$$

Term-by-term:

$$A_{dir}(v_n^{dir}\cos(n\theta)+s_n^{dir}\sin(n\theta)) = A_{inc}(v_n^{inc}\cos(n\theta)+s_n^{inc}\sin(n\theta))-A_{dec}(v_n^{dec}\cos(n\theta)+s_n^{dec}\sin(n\theta)) \tag{A.9}$$

Observe that $\frac{\delta N_{dir,inc,dec}}{\delta\theta}$ are physically expected to be even functions. So, the s_n terms should vanish.

$$A_{dir}(v_n^{dir}\cos(n\theta)) = A_{inc}(v_n^{inc}\cos(n\theta)) - A_{dec}(v_n^{dec}\cos(n\theta)) \tag{A.10}$$

$$A_{dir}v_n^{dir} = A_{inc}v_n^{inc} - A_{dec}v_n^{dec} \tag{A.11}$$

$$v_n^{dir} = \frac{\frac{A_{inc}}{A_{dec}}v_n^{inc} - v_n^{dec}}{A_{dir}} \tag{A.12}$$

Since

$$A_{dir} = A_{inc} - A_{dec} \tag{A.13}$$

$$A_{dir} = \frac{A_{inc}}{A_{dec}} - 1 = R - 1 \tag{A.14}$$

Where

$$R \equiv \frac{\left[\frac{A^{inc}(p_t)}{\pi^0(p_t)}\right]_{data}}{\left[\frac{A^{decay}(p_t)}{\pi^0(p_t)}\right]_{MC}} \approx \frac{A^{inc}(p_t)}{A^{decay}(p_t)} \tag{A.15}$$

Then,

$$v_n^{dir} \approx \frac{Rv_n^{inc} - v_n^{dec}}{R-1} \tag{A.16}$$

B. DATA SETS

B.1 11h (PbPb $\sqrt{s_{NN}} = 2.76$ TeV)

Runlist listRCTAndJPsigood: 167987, 167988, 168310, 168311, 168322, 168325, 168341, 168342, 168361, 168362, 168458, 168460, 168464, 168467, 168511, 168512, 168514, 168777, 168826, 168984, 168988, 168992, 169035, 169091, 169094, 169099, 169138, 169143, 169144, 169145, 169148, 169156, 169160, 169167, 169238, 169411, 169415, 169417, 169418, 169419, 169420, 169475, 169498, 169504, 169506, 169512, 169515, 169550, 169553, 169554, 169555, 169557, 169584, 169586, 169587, 169588, 169590, 169591, 169835, 169837, 169846, 169855, 169858, 169859, 169923, 169956, 169965, 169975, 169981, 170027, 170036, 170038, 170040, 170083, 170085, 170152, 170155, 170159, 170163, 170193, 170195, 170203, 170204, 170207, 170208, 170228, 170230, 170268, 170269, 170270, 170306, 170308, 170309, 170311, 170312, 170313, 170315, 170387, 170388, 170556, 170572, 170593

Runlist listPCMgood: 167987, 167988, 168310, 168311, 168322, 168325, 168341, 168342, 168361, 168362, 168458, 168460, 168464, 168467, 168511, 168512, 168514, 168777, 168826, 168984, 168988, 168992, 169035, 169091, 169094, 169138, 169143, 169144, 169145, 169148, 169156, 169160, 169167, 169238, 169411, 169415, 169417

Runlist listTPCOROC8Problems: 169099, 169418, 169419, 169420, 169475, 169498, 169504, 169506, 169512, 169515, 169550, 169553, 169554, 169555, 169557, 169584, 169586, 169587, 169588, 169590, 169591

Runlist listTPCIROC13Problems: 169975, 169981, 170027, 170036, 170038, 170040, 170083, 170085, 170152, 170155, 170159, 170163, 170193, 170195, 170203, 170204, 170207, 170208, 170228, 170230, 170268, 170269, 170270, 170306, 170308, 170309, 170311, 170312, 170313, 170315, 170387, 170388, 170556, 170572, 170593

Runlist listTPCvaryingVoltagesProblems: 169835, 169837, 169846, 169855, 169858, 169859, 169923, 169956, 169965

Runlist listEMCgood: 168310, 168311, 168322, 168325, 168341, 168342, 168361, 168362, 168458, 168460, 168461, 168464, 168467, 168511, 168512, 168514, 168777, 168826, 168984, 168988, 168992, 169035, 169040, 169044, 169045, 169238, 169411, 169415, 169417, 169418, 169419, 169420, 169475, 169498, 169504, 169506, 169512, 169515, 169550, 169553, 169554, 169555, 169557, 169584, 169586, 169587, 169588, 169591, 169835, 169837, 169838, 169846, 169855, 169858, 169923, 169975, 169981, 170027, 170036, 170038, 170040, 170081, 170083, 170084, 170085, 170088, 170089, 170091, 170152, 170155, 170159, 170163, 170193, 170195, 170203, 170204, 170228, 170230, 170268, 170269, 170270, 170306, 170308, 170309, 170311, 170313, 170315, 170387, 170388, 170572, 170593

Runlist listPCMgood+VaryingVoltages (no phi cut): 167987, 167988, 168310, 168311, 168322, 168325, 168341, 168342, 168361, 168362, 168458, 168460, 168464, 168467, 168511, 168512, 168514, 168777, 168826, 168984, 168988, 168992, 169035, 169091, 169094, 169138, 169143, 169144, 169145, 169148, 169156, 169160, 169167, 169238, 169411, 169415, 169417, 169835, 169837, 169846, 169855, 169858, 169859, 169923, 169965

Runlist listDeviatingTPCChambers: 169099, 169418, 169419, 169420, 169475, 169498, 169504, 169506, 169512, 169515, 169550, 169553, 169554, 169555, 169557, 169584, 169586, 169587, 169588, 169590, 169591, 169975, 169981, 170027, 170036, 170038, 170040, 170083, 170085, 170152, 170155, 170159, 170163, 170193, 170195, 170203, 170204, 170207, 170208, 170228, 170230, 170268, 170269, 170270, 170306, 170308, 170309, 170311, 170312, 170313, 170315, 170387, 170388, 170572, 170593

Runlist Bneg: 167987, 167988, 168310, 168311, 168322, 168325, 168341, 168342, 168361, 168362, 168458, 168460, 168464, 168467, 168511, 168512, 168514, 168777, 168826, 168984, 168988, 168992, 169035, 169091, 169094, 169099, 169138, 169143, 169144, 169145, 169148, 169156, 169160, 169167, 169238, 169411, 169415, 169417, 169418, 169419, 169420, 169475, 169498, 169504, 169506, 169512, 169515, 169550, 169553, 169554, 169555, 169557, 169584, 169586, 169587, 169588, 169590, 169591

Runlist Bpos: 169835, 169837, 169846, 169855, 169858, 169859, 169923, 169956, 169965, 169975, 169981, 170027, 170036, 170038, 170040, 170083, 170085, 170152, 170155, 170159, 170163, 170193, 170195, 170203, 170204, 170207, 170208, 170228, 170230, 170268, 170269, 170270, 170306, 170308, 170309, 170311, 170312, 170313, 170315, 170387, 170388, 170556, 170572, 170593

Runlist 11: 168464

B.2 10h (used for cross check) (PbPb $\sqrt{s_{NN}} = 2.76$ TeV)

137161, 137162, 137165, 137230, 137231, 137232, 137235, 137236, 137243, 137366, 137430, 137431, 137432, 137434, 137439, 137440, 137441, 137443, 137530, 137531, 137539, 137541, 137544, 137546, 137549, 137595, 137608, 137638, 137639, 137685, 137686, 137691, 137692, 137693, 137704, 137718, 137722, 137724, 137751, 137752, 137844, 137848, 138190, 138192, 138197, 138201, 138225, 138275, 138364, 138396, 138438, 138439, 138442, 138469, 138534, 138578, 138579, 138582, 138583, 138621, 138624, 138638, 138652, 138653, 138662, 138666, 138730, 138732, 138837, 138870, 138871, 138872, 139028, 139029, 139036, 139037, 139038, 139104, 139105, 139107, 139173, 139308, 139309, 139310, 139311, 139314, 139328, 139329, 139360, 139437, 139438, 139439, 139465, 139503, 139504, 139505, 139507, 139510

B.3 14a1a (PbPb $\sqrt{s_{NN}} = 2.76$ TeV) (Monte Carlo, 10h benchmarks, Central)

Runlist listRCTAndJPsigood: 167987, 167988, 168310, 168311, 168322, 168325, 168341, 168342, 168361, 168362, 168458, 168460, 168464, 168467, 168511, 168512, 168514, 168777, 168826, 168984, 168988, 168992, 169035, 169091, 169094, 169099, 169138, 169143, 169144, 169145, 169148, 169156, 169160, 169167, 169238, 169411, 169415, 169417, 169418, 169419, 169420, 169475, 169498, 169504, 169506, 169512,

169515, 169550, 169553, 169554, 169555, 169557, 169584, 169586, 169587, 169588, 169590, 169591, 169835, 169837, 169846, 169855, 169858, 169859, 169923, 169956, 169965, 169975, 169981, 170027, 170036, 170038, 170040, 170083, 170085, 170152, 170155, 170159, 170163, 170193, 170195, 170203, 170204, 170207, 170208, 170228, 170230, 170268, 170269, 170270, 170306, 170308, 170309, 170311, 170312, 170313, 170315, 170387, 170388, 170556, 170572, 170593 Runlist listPCMgood: 167987, 167988, 168310, 168311, 168322, 168325, 168341, 168342, 168361, 168362, 168458, 168460, 168464, 168467, 168511, 168512, 168514, 168777, 168826, 168984, 168988, 168992, 169035, 169091, 169094, 169138, 169143, 169144, 169145, 169148, 169156, 169160, 169167, 169238, 169411, 169415, 169417 Runlist listTPCOROC8Problems: 169099, 169418, 169419, 169420, 169475, 169498, 169504, 169506, 169512, 169515, 169550, 169553, 169554, 169555, 169557, 169584, 169586, 169587, 169588, 169590, 169591 Runlist listTPCIROC13Problems: 169975, 169981, 170027, 170036, 170038, 170040, 170083, 170085, 170152, 170155, 170159, 170163, 170193, 170195, 170203, 170204, 170207, 170208, 170228, 170230, 170268, 170269, 170270, 170306, 170308, 170309, 170311, 170312, 170313, 170315, 170387, 170388, 170556, 170572, 170593 Runlist listTPCvaryingVoltagesProblems: 169835, 169837, 169846, 169855, 169858, 169859, 169923, 169956, 169965 Runlist listEMCgood: 168310, 168311, 168322, 168325, 168341, 168342, 168361, 168362, 168458, 168460, 168461, 168464, 168467, 168511, 168512, 168514, 168777, 168826, 168984, 168988, 168992, 169035, 169040, 169044, 169045, 169238, 169411, 169415, 169417, 169418, 169419, 169420, 169475, 169498, 169504, 169506, 169512, 169515, 169550, 169553, 169554, 169555, 169557, 169584, 169586, 169587, 169588, 169591, 169835, 169837, 169838, 169846, 169855, 169858, 169923, 169975, 169981, 170027, 170036, 170038, 170040, 170081, 170083, 170084, 170085, 170088, 170089, 170091, 170152, 170155, 170159, 170163, 170193, 170195, 170203, 170204, 170228, 170230, 170268, 170269, 170270, 170306, 170308, 170309, 170311, 170313, 170315, 170387, 170388, 170572, 170593 Runlist listPCMgood+VaryingVoltages (no phi cut): 167987, 167988, 168310, 168311, 168322, 168325, 168341, 168342, 168361, 168362, 168458, 168460, 168464, 168467, 168511, 168512, 168514, 168777, 168826, 168984, 168988, 168992, 169035, 169091, 169094, 169138, 169143, 169144, 169145, 169148, 169156, 169160, 169167, 169238, 169411, 169415, 169417, 169835, 169837, 169846, 169855, 169858, 169859, 169923, 169965 Runlist listOROCproblems: 169099, 169418, 169419, 169420, 169475, 169498, 169504, 169506, 169512, 169515, 169550, 169553, 169554, 169555, 169557, 169584, 169586, 169587, 169588, 169590, 169591, 169975, 169981, 170027, 170036, 170038, 170040, 170083, 170085, 170152, 170155, 170159, 170163, 170193, 170195, 170203, 170204, 170207, 170208, 170228, 170230, 170268, 170269, 170270, 170306, 170308, 170309, 170311, 170312, 170313, 170315, 170387, 170388, 170572, 170593 Runlist Bneg: 167987, 167988, 168310, 168311, 168322, 168325, 168341, 168342, 168361, 168362, 168458, 168460, 168464, 168467, 168511, 168512, 168514, 168777, 168826, 168984, 168988, 168992, 169035, 169091, 169094, 169099, 169138, 169143, 169144, 169145, 169148, 169156, 169160, 169167, 169238, 169411, 169415, 169417, 169418, 169419, 169420, 169475, 169498, 169504, 169506, 169512, 169515, 169550, 169553, 169554, 169555, 169557, 169584, 169586, 169587, 169588, 169590, 169591 Runlist Bpos: 169835, 169837, 169846, 169855, 169858, 169859, 169923, 169956, 169965, 169975, 169981, 170027, 170036, 170038, 170040, 170083, 170085, 170152, 170155, 170159, 170163, 170193, 170195, 170203, 170204, 170207, 170208, 170228, 170230, 170268, 170269, 170270, 170306, 170308, 170309, 170311, 170312, 170313, 170315, 170387, 170388, 170556, 170572, 170593

B.4 14a1b (PbPb $\sqrt{s_{NN}}$ = 2.76 TeV) (Monte Carlo, 10h benchmarks, Semi-Central)

Runlist listRCTAndJPsigood: 167987, 167988, 168310, 168311, 168322, 168325, 168341, 168342, 168361, 168362, 168458, 168460, 168464, 168467, 168511, 168512, 168514, 168777, 168826, 168984, 168988, 168992, 169035, 169091, 169094, 169099, 169138, 169143, 169144, 169145, 169148, 169156, 169160, 169167, 169238, 169411, 169415, 169417, 169418, 169419, 169420, 169475, 169498, 169504, 169506, 169512,

169515, 169550, 169553, 169554, 169555, 169557, 169584, 169586, 169587, 169588, 169590, 169591, 169835, 169837, 169846, 169855, 169858, 169859, 169923, 169956, 169965, 169975, 169981, 170027, 170036, 170038, 170040, 170083, 170085, 170152, 170155, 170159, 170163, 170193, 170195, 170203, 170204, 170207, 170208, 170228, 170230, 170268, 170269, 170270, 170306, 170308, 170309, 170311, 170312, 170313, 170315, 170387, 170388, 170556, 170572, 170593 Runlist listPCMgood: 167987, 167988, 168310, 168311, 168322, 168325, 168341, 168342, 168361, 168362, 168458, 168460, 168464, 168467, 168511, 168512, 168514, 168777, 168826, 168984, 168988, 168992, 169035, 169091, 169094, 169138, 169143, 169144, 169145, 169148, 169156, 169160, 169167, 169238, 169411, 169415, 169417 Runlist listTPCOROC8Problems: 169099, 169418, 169419, 169420, 169475, 169498, 169504, 169506, 169512, 169515, 169550, 169553, 169554, 169555, 169557, 169584, 169586, 169587, 169588, 169590, 169591 Runlist listTPCIROC13Problems: 169975, 169981, 170027, 170036, 170038, 170040, 170083, 170085, 170152, 170155, 170159, 170163, 170193, 170195, 170203, 170204, 170207, 170208, 170228, 170230, 170268, 170269, 170270, 170306, 170308, 170309, 170311, 170312, 170313, 170315, 170387, 170388, 170556, 170572, 170593 Runlist listTPCvaryingVoltagesProblems: 169835, 169837, 169846, 169855, 169858, 169859, 169923, 169956, 169965 Runlist listEMCgood: 168310, 168311, 168322, 168325, 168341, 168342, 168361, 168362, 168458, 168460, 168461, 168464, 168467, 168511, 168512, 168514, 168777, 168826, 168984, 168988, 168992, 169035, 169040, 169044, 169045, 169238, 169411, 169415, 169417, 169418, 169419, 169420, 169475, 169498, 169504, 169506, 169512, 169515, 169550, 169553, 169554, 169555, 169557, 169584, 169586, 169587, 169588, 169591, 169835, 169837, 169838, 169846, 169855, 169858, 169923, 169975, 169981, 170027, 170036, 170038, 170040, 170081, 170083, 170084, 170085, 170088, 170089, 170091, 170152, 170155, 170159, 170163, 170193, 170195, 170203, 170204, 170228, 170230, 170268, 170269, 170270, 170306, 170308, 170309, 170311, 170313, 170315, 170387, 170388, 170572, 170593 Runlist listPCMgood+VaryingVoltages (no phi cut): 167987, 167988, 168310, 168311, 168322, 168325, 168341, 168342, 168361, 168362, 168458, 168460, 168464, 168467, 168511, 168512, 168514, 168777, 168826, 168984, 168988, 168992, 169035, 169091, 169094, 169138, 169143, 169144, 169145, 169148, 169156, 169160, 169167, 169238, 169411, 169415, 169417, 169835, 169837, 169846, 169855, 169858, 169859, 169923, 169965 Runlist listOROCproblems: 169099, 169418, 169419, 169420, 169475, 169498, 169504, 169506, 169512, 169515, 169550, 169553, 169554, 169555, 169557, 169584, 169586, 169587, 169588, 169590, 169591, 169975, 169981, 170027, 170036, 170038, 170040, 170083, 170085, 170152, 170155, 170159, 170163, 170193, 170195, 170203, 170204, 170207, 170208, 170228, 170230, 170268, 170269, 170270, 170306, 170308, 170309, 170311, 170312, 170313, 170315, 170387, 170388, 170572, 170593 Runlist Bneg: 167987, 167988, 168310, 168311, 168322, 168325, 168341, 168342, 168361, 168362, 168458, 168460, 168464, 168467, 168511, 168512, 168514, 168777, 168826, 168984, 168988, 168992, 169035, 169091, 169094, 169099, 169138, 169143, 169144, 169145, 169148, 169156, 169160, 169167, 169238, 169411, 169415, 169417, 169418, 169419, 169420, 169475, 169498, 169504, 169506, 169512, 169515, 169550, 169553, 169554, 169555, 169557, 169584, 169586, 169587, 169588, 169590, 169591 Runlist Bpos: 169835, 169837, 169846, 169855, 169858, 169859, 169923, 169956, 169965, 169975, 169981, 170027, 170036, 170038, 170040, 170083, 170085, 170152, 170155, 170159, 170163, 170193, 170195, 170203, 170204, 170207, 170208, 170228, 170230, 170268, 170269, 170270, 170306, 170308, 170309, 170311, 170312, 170313, 170315, 170387, 170388, 170556, 170572, 170593

B.5 14a1c (PbPb $\sqrt{s_{NN}} = 2.76$ TeV) (Monte Carlo, 10h benchmarks, Peripheral)

Runlist listRCTAndJPsigood: 167987, 167988, 168310, 168311, 168322, 168325, 168341, 168342, 168361, 168362, 168458, 168460, 168464, 168467, 168511, 168512, 168514, 168777, 168826, 168984, 168988, 168992, 169035, 169091, 169094, 169099, 169138, 169143, 169144, 169145, 169148, 169156, 169160, 169167, 169238, 169411, 169415, 169417, 169418, 169419, 169420, 169475, 169498, 169504, 169506, 169512,

169515, 169550, 169553, 169554, 169555, 169557, 169584, 169586, 169587, 169588, 169590, 169591, 169835, 169837, 169846, 169855, 169858, 169859, 169923, 169956, 169965, 169975, 169981, 170027, 170036, 170038, 170040, 170083, 170085, 170152, 170155, 170159, 170163, 170193, 170195, 170203, 170204, 170207, 170208, 170228, 170230, 170268, 170269, 170270, 170306, 170308, 170309, 170311, 170312, 170313, 170315, 170387, 170388, 170556, 170572, 170593 Runlist listPCMgood: 167987, 167988, 168310, 168311, 168322, 168325, 168341, 168342, 168361, 168362, 168458, 168460, 168464, 168467, 168511, 168512, 168514, 168777, 168826, 168984, 168988, 168992, 169035, 169091, 169094, 169138, 169143, 169144, 169145, 169148, 169156, 169160, 169167, 169238, 169411, 169415, 169417 Runlist listTPCOROC8Problems: 169099, 169418, 169419, 169420, 169475, 169498, 169504, 169506, 169512, 169515, 169550, 169553, 169554, 169555, 169557, 169584, 169586, 169587, 169588, 169590, 169591 Runlist listTPCIROC13Problems: 169975, 169981, 170027, 170036, 170038, 170040, 170083, 170085, 170152, 170155, 170159, 170163, 170193, 170195, 170203, 170204, 170207, 170208, 170228, 170230, 170268, 170269, 170270, 170306, 170308, 170309, 170311, 170312, 170313, 170315, 170387, 170388, 170556, 170572, 170593 Runlist listTPCvaryingVoltagesProblems: 169835, 169837, 169846, 169855, 169858, 169859, 169923, 169956, 169965 Runlist listEMCgood: 168310, 168311, 168322, 168325, 168341, 168342, 168361, 168362, 168458, 168460, 168461, 168464, 168467, 168511, 168512, 168514, 168777, 168826, 168984, 168988, 168992, 169035, 169040, 169044, 169045, 169238, 169411, 169415, 169417, 169418, 169419, 169420, 169475, 169498, 169504, 169506, 169512, 169515, 169550, 169553, 169554, 169555, 169557, 169584, 169586, 169587, 169588, 169591, 169835, 169837, 169838, 169846, 169855, 169858, 169923, 169975, 169981, 170027, 170036, 170038, 170040, 170081, 170083, 170084, 170085, 170088, 170089, 170091, 170152, 170155, 170159, 170163, 170193, 170195, 170203, 170204, 170228, 170230, 170268, 170269, 170270, 170306, 170308, 170309, 170311, 170313, 170315, 170387, 170388, 170572, 170593

B.6 11a (pp $\sqrt{s_{NN}} = 2.76$ TeV)

146860, 146859, 146858, 146857, 146856, 146824, 146817, 146814, 146813, 146812, 146808, 146807, 146806, 146805, 146804, 146803, 146802, 146801, 146748, 146747, 146746, 146689, 146688, 146686

B.7 15d3b (pp $\sqrt{s_{NN}} = 2.76$ TeV) (Monte Carlo, LHC13g anchors)

197471, 197496, 197497, 197499, 197500, 197501, 197527, 197529, 197531, 197553, 197555, 197583, 197584, 197606, 197608, 197609, 197610, 197611, 197613, 197618, 197643, 197669

REFERENCES

REFERENCES

[1] E.D Bloom et al. Phys. Rev. Lett., 23. 930-934. (1969) 1

[2] Particle Data Group. Phys Rev Lett B, 667. 1061-1206. (2008) 1, 2

[3] Shuryak. The QCD Vacuum, Hadrons, and Superdense Matter. World Scientific Pub Co Inc. (2004) 3

[4] Appelquist and Politzer. Phys. Rev. Lett. 34. 43. (1975) 3

[5] Wong. Introduction to High-Energy Heavy-Ion Collisions. World Scientific Pub Co Inc. (1994) 3, 22, 24

[6] Bass et al, representing the US Heavy-Ion Community. "Hot and Dense QCD Matter: Unraveling the Mysteries of the Strongly Interacting Quark-Gluon-Plasma". A Community White Paper on the Future of Relativistic Heavy-Ion Physics in the US. 4, 6, 8

[7] R.J. Fries and B. Muller. The European Physical Journal C - Particles and Fields, 34. 279–285. (2004) vi, 5

[8] Enterria, Peressounko. Eur.Phys.J.C 46. 451-464. (2006) 4

[9] Karsch. Lect.Notes Phys. 583. 209-249. (2002) 4

[10] Shapiro and Teukolsky. Black Holes, White Dwarfs and Neutron Stars: The Physics of Compact Objects. Wiley. (2008) 4

[11] "New State of Matter Created at CERN". The CERN Courier. <http://press.web.cern.ch/press-releases/2000/02/new-state-matter-created-cern>. (2000) 6

[12] Chiho and Nonaka. arXiv:1204.4795 [nucl-th]. <http://arxiv.org/pdf/1204.4795v2.pdf>. (2012) vi, 6

[13] Miller, Reygers, Sanders, and Steinberg. Ann.Rev.Nucl.Part.Sci. 57. 205-243. (2007) vi, 6, 7

[14] Tawfik and Shalaby. Adv. in High Energy Phys. 186812. (2015) vi, 9

[15] The ALICE Collaboration. JINST 8 P10016. arXiv:1306.3130. (2013) 8, 15, 94

[16] H. Satz. Extreme States of Matter in Strong Interaction Physics, page 166. Springer-Verlag Berlin Heidelberg. (2012) 8, 22

[17] Heinz and Kestin. Eur.Phys.J.ST 155:75-87. (2008) 8

[18] ATLAS collaboration. <http://www.atlas.ch/photos/lhc.html> (2014) vi, 12

[19] Horowitz. “Probing the Frontiers of the QCD”. Columbia University. arXiv:1011.4316. (2008) vi, 10

[20] “The LHC’s first long run”. The CERN Courier. <http://cerncourier.com/cws/article/cern/54381>. (2013) 11

[21] Alice Collaboration. <http://aliceinfo.cern.ch/General/index.html>. ALICE Collaboration Website. (2012) vi, 11, 13

[22] Alice Collaboration. “ALICE Data Acquisition” <http://aliceinfo.cern.ch/Public/en/Chapter2/Chap2_DAQ.html> ALICE Collaboration Website. (2008) 13, 14

[23] Alice Collaboration. J. Phys. G: Nucl. Part. Phys. 30. 1517. (2004) 14, 29, 46

[24] Alice Collaboration. J. Phys. G: Nucl. Part. Phys. 32. 1295. (2006) 14, 29, 46

[25] Bock. “ALICE Capabilities for Studying Photon Physics with Conversion Method at LHC Energies”. Bachelor Colloquium at Physikalisches Institut Heidelberg. (2010) vii, 19

[26] Wilde. “Measurement of Direct Photons in pp and Pb-Pb Collisions with ALICE”. Quark Matter 2012. (2012) 16, 22, 115

[27] Particle Data Group. PL B667, 1. (2008) 16, 63

[28] Koch. “Measurement of Pi_0 and eta mesons with photon conversions in ALICE in proton-proton collisions as root(s) = 0.9, 2.76, and 7 TeV”. PhD Thesis at the University of Heidelberg, Germany. (2012) 17

[29] Alice Collaboration. Phys. Lett. B 754. 235-248. (2016) vii, 17, 20, 21, 26, 44, 78

[30] Arsene I, et al. Nucl. Phys. A 757. 1. (2005)

[31] Adcox K, et al. Nucl. Phys. A 757. 184. (2005)

[32] Back BB, et al. Nucl. Phys. A 757. 28. (2005)

[33] Adams J, et al. Nucl. Phys. A 757. 102. (2005)

[34] d’Enterria and Peressounko. Eur.Phys.J.C 46. 451-464. (2006) vii, 16, 18, 20, 63, 112, 117

[35] ALICE Collaboration. J. Phys.: Conf. Ser. 446 012028. arXiv:1212.3995v2. (2013)

[36] Chatterjee, Srivastava, and Renk. Quark Matter 2014. Darmstadt, Germany. arXiv:1407.8329 [nucl-th]. (2014)

[37] Luzum and Ollitrault. Phys. Rev. C87 044907. (2013) 96, 97

[38] ALICE Collaboration. “Direct photon and neutral pion production in pp and Pb-Pb collisions measured with the ALICE experiment at LHC”. Proceedings of XXXth International Workshop on High Energy Physics, Protvino, Russia. (2014) vii, 20, 23, 78

[39] Gelis. Invited review for International Journal of Modern Physics; based on lectures given at the 22nd Jyvaskyla Summer School, version 2. arXiv:1211.3327 [hep-ph]. (2012) 22

[40] PHENIX Collaboration. ”Centrality dependence of low-momentum direct-photon production in Au+Au collisions at $\sqrt{s}$ = 200 GeV”. Phys. Rev. C. v2. arXiv:1405.3940 [nucl-ex]. (2015) 22

[41] E. L. Feinberg, Nuovo Cim. A 34, 391. (1976) 22, 111

[42] K. Kajantie and H. I. Miettinen, Z. Phys. C 9, 341. (1981) 22, 111

[43] Shen, Heinz, Paquet, and Gale. Phys. Rev. C 89, 044910. (2014) 22, 112, 117

[44] PHENIX Collaboration. Phys. Rev. Lett. 104, 132301. (2010) 24

[45] Gyulassy and Wang. Nuclear Physics B, Volume 420, Issue 3, 6. 583-61. (1994) 24, 25

[46] PHENIX Collaboration. Phys. Rev. Lett. 101, 232301. (2008) 25

[47] ALICE Collaboration. J. Phys.: Conf. Ser. 664 082023. (2015) 30

[48] d’Enterria. “Hard scattering cross sections at LHC in the Glauber approach: from pp to pA and AA collisions”. <arXiv:nucl-ex/0302016>. (2004) 85, 91

[49] The Alice Collaboration. “Measurement of inelastic, single- and double-diffraction cross sections in proton–proton collisions at the LHC with ALICE” <arXiv:1208.4968>. (2012) 91

[50] The Alice Collaboration. Phys. Rev. C 88 044909. (2013) 91

[51] The ALICE Collaboration. JHEP06 190. (2015) x, 109

[52] Song and Hienz. Phys. Rev. C 77, 064901. (2008) 115

[53] Heinz and Snellings. Annu. Rev. Nucl. Part. Sci. 63. 123-151. (2013) 115

[54] LHC MACHINE OUTREACH. ”LHC collisions”. <http://lhc-machine-outreach.web.cern.ch/lhc-machine-outreach/collisions.htm> (2016) 93

[55] Abrahamyan et al. Phys. Rev. Lett. 108, 112502. (2012) 93

[56] ALICE collaboration. Cern Courier. “ALICE: from LS1 to readiness for Run 2”. <http://cerncourier.com/cws/article/cern/60878>. (2015) vii, 47

[57] Kovchegov. Nucl.Phys.A 762. 298-325. (2005) 24

[58] Stöcker. Nucl.Phys.A 750. 121-147. (2004) 25

[59] Nahrgang et al. Phys.Rev.C 91. 014904. (2015) 26

[60] Conesa et al. Nucl.Instr.Meth.Phys.Research A 537. 363–367. (2004) 31, 32, 39, 40, 43, 97

[61] Ippolitov et al. Nucl.Instr.Meth.Phys.Research A 486. 121–125. (2002) 31

[62] Muller et al. Nucl.Instr.Meth.Phys.Research A 518. 525–528. (2004) 32

[63] Hoecker and Kartvelishvili. Nucl.Instr.Meth.Phys.Research A 372. 469-481. (1996) 32

[64] Agostini. Nucl.Instr.Meth.Phys.Research A 362. 487–498. (1995) 32

[65] ALICE EMCAL Collaboration. "ALICE EMCal Physics Performance Report". Submitted to the U.S. Department of Energy. <arXiv:1008.0413>. (2010) 37

[66] Ichou for ALICE Collaboration. Nucl.Phys.A 855. 339-342. (2011) 37

[67] Alme. "Firmware Development and Integration for ALICE TPC and PHOS Front-end Electronics " Dissertation for the degree philosophiae doctor (PhD) at the University of Bergen. (2008) 37

[68] Taylor. IEEE Transactions on Nuclear Science 45; 3. 821 - 828. (1998) 39

[69] Christiansen. Nuclear Science Symposium and Medical Imaging Conference Record Vol 1. 597 - 601. (1995) 39

[70] Jing. Nuclear Physics Review; ISSN 1007-4627 v. 21(1). 12-16. (2004) 43

[71] Lippman. Nucl.Instr.Meth.Phys.Research A 666. 148-172. (2012) 43

[72] Alme et al. Nucl.Instr.Meth.Phys.Research A 622. 316-367. (2010) 43

[73] The ALICE Collaboration. Phys. Lett. B 754. 235-248. (2016) 16, 50, 84, 111

[74] ALICE Collaboration. Phys.Rev.Lett. 107. 032301. (2011) ix, x, 91, 99, 104, 105, 106

[75] Fernández. Nucl.Instr.Meth.Phys.Research A 572. 102-103. (2007) 46

[76] ALICE Collaboration. Photon Spectrometer PHOS, CERN/LHCC 99-4, ALICE TDR 2. (1999) 48, 52

[77] Particle Data Group. Chin. Phys. C 38. 090001. (2015) 48

[78] ALICE collaboration. Nucl.Phys.A 855. 213-216. (2011) 72, 75, 100

[79] Deng, Wang, and Xu. Phys.Rev. C 83. 014915. (2011) 75

[80] Turbide, Rapp, and Gale. Phys. Rev. C 69. 014903. (2004) 85

[81] Liu and Werner. J. Phys. G: Nucl. Part. Phys. 38. 124183. (2011) 85

[82] Avsar, Hatta, Flensburg, Ollitrault, and Ueda. J. Phys. G: Nucl. Part. Phys. 38. 124053. (2011) 85

[83] Luzum. J. Phys. G: Nucl. Part. Phys. 38. 124026. (2011) 96

[84] CMS Collaboration. Phys. Rev. Lett. 110. 042301. (2013) 100

[85] The ALICE Collaboration. J. Phys. Conf. Ser. 446 012028. (2013) 104, 107

[86] PHENIX Collaboration. PRL 105, 142301. (2010) 108

[87] Rinard. “Neutron Interactions with Matter”, Los Alamos Technical Report. <http://www.fas.org/sgp/othergov/doe/ lanl/lib-www/la-pubs/00326407.pdf>. (2009) 112

[88] Shen, Heinz, Paquet, and Gale. Nuclear Physics A 932. 184–188. (2014) 114, 116

VITA

VITA

Tyler A. Browning attended Purdue University from May 2010 to August 2016. Previously he attained his Bachelor of Science at Georgia Institute of Technology with a major in applied physics and minor in mathematics (specializing in applied physics and differential equations). While at Purdue he worked in the Purdue Nuclear Physics Group, which specializes in relativistic heavy ion collisions. Additionally, he taught elementary mechanics laboratory and electrodynamics recitation for engineering undergraduates.

In 2011, he became involved in the A Large Ion Collider Experiment (ALICE) at the Large Hadron Collider (LHC) in Geneva, Switzerland and spent several months per year working on site at ALICE throughout the remainder of his time at Purdue. While at ALICE he: participated in commissioning the DCAL expansion to the Electromagnetic Calorimeter (EMCAL), served as Detector Safety Control operator for ALICE during data taking, updated the EMCAL documentation, and worked alongside international collaborators in experimental nuclear physics.

After graduation, Tyler intends to continue working in the field of nuclear physics and will use the skills he has developed at Purdue to contribute to solving some of the most outstanding problems he sees facing the next generation of scientists.